Consejo Superior de Investigaciones Científicas
CSIC

Universitat Autònoma de Barcelona

Escola Tècnica Superior d'Enginyeria

Internal IR-laser Deflection Measurements of Temperature and Free-Carrier Concentration in Power Devices

A dissertation submitted to the department of electronic engineering and the committee on graduate studies of Universitat Autònoma de Barcelona in partial fulfilment of the requirements for the degree of doctor of philosophy by:

Xavier Perpiñá Giribet

Power Devices and Systems Group

Centre Nacional de Microelectrònica

Consejo Superior de Investigaciones Científicas

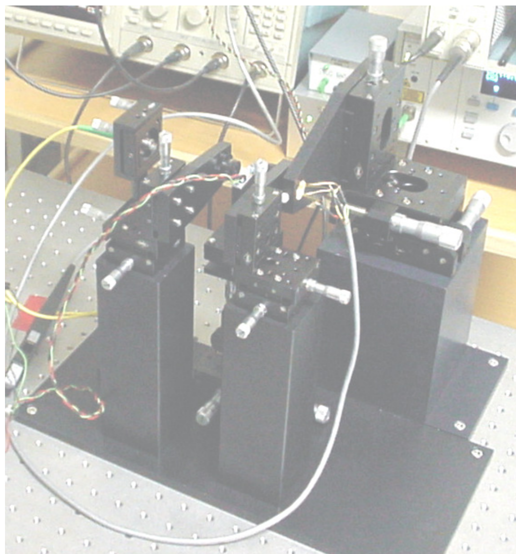

Supervised by
Dr. Xavier Jordà Sanuy
Dr. Narcís Mestres Andreu

Assigned Tutor:
Prof. Francesc Serra Mestres

Bellaterra, May 27th 2005

Els Drs. Xavier Jordà i Sanuy, Científic Titular del Centre Nacional de Microelectrónica de Barcelona, i Narcís Mestres i Andreu, Investigador Científic de l'Institut de Ciencia de Materials de Barcelona

CERTIFIQUEN

El treball que duu per títol "Internal IR-laser Deflection Measurements of Temperature and Free-carrier Concentration in Power Devices", presentat per Xavier Perpiñá Giribet com a memòria de la tesis doctoral en Enginyeria Electrònica, ha estat realitzat sota la seva direcció.

Bellaterra, Maig de 2005

Dr. Xavier Jordà i Sanuy

Dr. Narcís Mestres i Andreu

Tutor:Prof. Francesc Serra i Mestres

Acknowledgements

After all those years, I have a long list of people who contributed in some way to this thesis, for which I would like to express my gratitude.

First of all, special thanks to Prof. Francesc Serra, who let me use the C.N.M. facilities for my research. I would like to acknowledge the supervision of Drs. Xavier Jordà and Narcís Mestres during the development of this work. With great appreciation, I would like to thank Prof. J. Vobecký from the Czech Technical University (Czech) for his continuous support and kindly providing some of the investigated samples. In addition, this work would not have been possible without the careful sample preparation performed by Mr. H. von Kiedrowski from the Paul Drude Institut für Festkörperelektronik in Berlin (Germany) and all of the CNM technical services.

I'm also grateful with Prof. José Millán, Dr. José Rebollo, Dr. Salvador Hidalgo, Dr. Miquel Vellvehi, Dr. David Flores and Dr. Philippe Godignon for their advice and encouragement throughout this investigation. I would like to thank all my colleagues for their help, comradeship and endless patience, Dr. Jaume Roig, Dr. Francesc Madrid, Dr. Riccardo Rurali, Dr. Servane Blanqué, Dr. Dominique Tournier, Jesús Urresti, Ignacio Cortés, José Luis Gálvez, Amador Pérez, Marcel Placidi, Juan Antonio Ramírez, and David Sánchez.

I am grateful for the wholehearted support that Lídia, my parents, and the rest of my family have given to me throughout.

This work was partially supported by the EC Growth Project ATHIS (G1RD-CT-2002-00729), CICYT project TIC 2000-1403-C003-03 entitled “Caracterización y Electrotérmica de dispositivos de SiC aplicados a sensores de gases”, and a postgraduate grant from Consejo Superior de Investigaciones Científicas (REF I3P-BPG2004).

Table of Figures

Figure 2.3.1. Free-carriers and temperature gradient interaction with the probe laser beam in the IIR-LD technique. 17

Figure 2.4.1. Experimental rig phototgraph. 20

Figure 2.5.1. Sketch of a laser beam traversing the analysed DUT, showing the main beam parameters. 21

Figure 2.5.2. Average value of the beam radius as a function of L, when NA= $NA|_{opt}$ 24

Figure 2.5.3. (a) Variation of the probe beam diameter on the chip lateral side as a function of the beam numerical aperture for λ=1.3µm and different values of L, showing the minima corresponding to each case. (b) Variation of the beam diameter average value along L as a function of the beam numerical aperture, also stressing the reachable values for L=5 mm and L=10 mm by means of equation (2.5.10). 26

Figure 2.5.4. Comparison between measured and predicted beam diameters, stressing L_{ef} where the optical set-up has been optimised. 27

Figure 2.6.1. Top view of the positioning system schematic, stressing its several parts. 29

Figure 2.7.1. Block diagram of the whole sensing system, showing its main variables. 30

Figure 2.7.2. Block diagram corresponding to the post-processing circuit. 33

Figure 2.7.3. N-input op amp based voltage adders with offset compensation: (a) Non-inverting configuration, (b) Inverting configuration. 35

Figure 2.7.4. Proposed schematic to remove input voltage offset for each signal channel. 35

Figure 2.7.5. Implemented adder with two input signals and the corresponding nulling offset voltages. 37

Figure 2.7.6. Circuit schematic showing the stage for compensating the input offset voltage. 37

Figure 2.7.7. (a) Schematic of the designed divisor to calculate $V_{out,y}$. (b) Nominal frequency response of the divisor gain depending on denominator value $V_{out,P}$. 38

Figure 2.7.8. (a) Experimental characterisation of the static system response, corresponding to $V_{out,y}$ vs spot relative displacement. (b) Experimental determination of the proportionality factor which relates P with $V_{out,P}$. 40

Figure 2.8.1. Schematic of the excitation System for DUT biasing under real operating conditions. 44

Figure 2.8.2. Schematic for the connectivity of other kind of devices, such as diodes or thermal test chips. 45

Figure 2.8.3. Simplified scheme of the gate-drive circuit 46

Figure 2.8.4. Cronogram of $V_{generator}$ and the three pulses generated by the SCU. 47

Figure 2.8.5. Schematic of the SCU, showing the monostables and tuning resistors configuration 48

Figure 3.3.1. (a) Schematic cross-sectional view of the TTC (not to scale), showing the substrate, the oxide layer, and the poly-Silicon dimensions. (b) Dimensions of the Pt sensing resistor. 53

Figure 3.3.2. Top view of a TTC part, showing both the heating and sensing resistors. 53

Figure 3.3.3. Simulated 3D-structure, part of the full size TTC, showing its dimensions (not to scale) 55

Figure 3.3.4. Simulated temperature increase profile along x direction for several depths at t=50 µs for the structure of Figure 3.3.3 55

Figure 3.3.5. 2D cross-sectional view of the simulated temperature distribution at z=300 µm and t=250 µs, showing that the isothermal line T=293 K is located 135 µm from the structure backside. 56

Figure 3.3.6. Simulated structure, showing its dimensions (not to scale), for inspecting ΔT under the TTC sensor. 57

Figure 3.3.7. Time evolution of ΔT 1-D cut along x direction performed at y=0 and z=3000 µm 58

Figure 3.4.1. Schematic illustrating the TTC connection to the excitation circuit. 60

Figure 3.5.1. Heating time dependence of the measured $V_{out,y}$ waveforms at different measurement depths, ranging from 45 µm to 470 µm with 25 µm steps. 62

Figure 3.5.2. Extracted temperature profile evaluated for $(\partial n/\partial T)_C$ reported values and its comparison with the prediction of equation (3) for t=250 µs. 62

Figure 3.5.3. Extracted temperature profile compared with the prediction of equation (3.3.1) for several heating times, using $(\partial n/\partial T)_C$ Magunov's value, for: (a) P-type substrate and (b) N-type substrate. Points are experimental values and lines display the predictions of the considered model using equation (3.3.1). 64

Figure 3.5.4. Comparison between the model results and the extracted temperature profile from the N-type TTC for (a) P_0=30W and (b) P_0=15W for several heating times, using $(\partial n/\partial T)_C$ Magunov's value. 65

Figure 4.3.1. Internal structure of the studied devices. 70

Figure 4.4.1. (a) 2D electrons density inside the simulated unirradiated diode where a surface recombination velocity of 2800 cm/s is considered. (b) Comparison of one-dimensional vertical profiles of electrons concentration obtained from considering (black lines) and not considering (red line) recombination at lateral faces, as well as electrons concentration average along the interaction length (●). 74

Figure 4.5.1. Measured waveforms of the time evolution of free-carrier concentration at various depths inside the drift region (y) for irradiated (a) and unirradiated (b) diodes, when a current density of 8 A/cm^2 is flowing through them. 77

Figure 4.5.2. Comparison between experiment (■,●) and simulation results (solid lines) for both devices, also showing holes (red solid lines) and electron (black solid lines) densities (C_p, C_n), as well as the doping profile (brown dashed line), along the entire device. 78

Figure 4.5.3. Comparison of free-carriers in the drift region between measurement (points) and simulation (solid lines) at current densities of 2.75 (△), 5 (■), 8 (▽), and 11 (○) A/cm^2 for both diodes: irradiated (a) and unirradiated (b). From simulation results, holes (red solid lines) and electron (black solid lines) densities (C_p, C_n), as well as the doping profile (brown dashed line) are also shown. 79

Figure 4.5.4. Comparison between the measured carriers decay time τ_{dec} for both devices (■, unirradiated; ◇, irradiated). 80

Figure 5.2.1. View of the basic half-cell cross-sections of the main important types of IGBTs: (a) NPT-IGBT (b) PT-IGBT. 84

Figure 5.3.1. Cross-section of the basic half-cell of the 600V PT-IGBT, showing its main parts and dimensions. 86

Figure 5.4.1. Simulated profile of holes concentration corresponding to a cut under the channel. 88

Figure 5.4.2. Simulated time evolution of vertical temperature distributions in the unirradiated PT-IGBT. 89

Figure 5.4.3. Summary of the numerical simulation results for the PT-IGBT (forward collector current pulse I_{Con}=9 A and t_{on}=100 µs): (a) collector current IC, (b) free-carrier concentration gradient, (c) temperature gradient, (d) refraction index gradient. Gradients evaluated in the drift region using two coordinates y1=22.5 µm and y2=47.5 µm. 91

Figure 5.5.1. Typical waveforms obtained for both biased PT-IGBT (t_{on}=100µs, I_{Con}=10A, V_{GE}=10V): (a) unirradiated, $E_{dissipated}$=2.80 mJ, (b) irradiated, $E_{dissipated}$=15.53 mJ. 92

Figure 5.5.2. Measured free-carrier concentration inside the drift region of the unirradiated PT-IGBT 93

Figure 5.5.3. Measured temperature gradients in the PT-IGBT drift region (y_0=35 μm) for: (a) unirradiated and (b) irradiated device. 95

Figure 5.5.4. Temperature gradient evolution for I_C=10 A and V_{GE}=10V at several t_{on} values, corresponding to: (a) unirradiated device, (b) irradiated device. 96

Figure 5.5.5. Temperature gradient as a function of t_{on} for I_{Con}=10A corresponding to each device. Lines show the corresponding fitting curves, according to expression (5.5.1). 98

Figure A.1.1. View of IIR-LD involved phenomena, showing the main parameters used for the final expression. 108

Table of Tables

Table 2.1. Reported values for both the plasma-optical coefficients $(\partial n/\partial C)_T$ and $(\partial \alpha/\partial C)_T$ when $C_n = C_p = 1\times10^{16}$ cm^{-3}, at room temperature (T = 300 K) and $\lambda = 1.3$ µm....................................... 14

Table 2.2. Reported values for the thermo-optical coefficient $(\partial n/\partial T)_C$ for $\lambda = 1.3$ µm. 16

Table 2.3. The main performances of the four channel preamplifier and FQP. 31

Table of Contents

TABLE OF FIGURES i

TABLE OF TABLES v

TABLE OF CONTENTS vii

CHAPTER 1 INTRODUCTION 1

1.1 INTRODUCTION 1
1.2 POWER DEVICES STRUCTURE 1
1.3 SELF-HEATING EFFECTS ON POWER DEVICES 3
1.4 THERMOMETRY TECHNIQUES IN POWER DEVICES 4
1.4.1 Electrical Methods 4
1.4.2 Optical Methods 5
1.5 SCOPE AND STRUCTURE OF THIS THESIS 8

CHAPTER 2 THE EXPERIMENTAL RIG 11

2.1 INTRODUCTION 11
2.2 OPERATION PRINCIPLE OF LASER PROBING TECHNIQUES 11
2.2.1 Dependence of Optical Properties 11
2.2.2 Plasma-Optical Effect 12
2.2.3 Thermo-Optical Effect 14
2.3 IIR-LD TECHNIQUE DESCRIPTION 16
2.4 EXPERIMENTAL RIG 19
2.5 OPTICAL SET-UP 20
2.5.1 The laser probe beam 20
2.5.1.1 The Beam Waist: Spatial Resolution in IIR-LD Measurements 20
2.5.1.2 Radiation Source Selection 24
2.5.2 Optical System Design and Implementation 25
2.5.2.1 Collimator and L_1-lens Selection and Obtained Performances 25
2.5.2.2 L_2-lens Selection and Results 28

2.6 MICRO-POSITIONING DISPLACEMENT MODULES 28
2.7 ELECTRICAL SET-UP I: POWER AND DEFLECTION SENSING SYSTEM 30
2.7.1 System Description and Constraints 30
2.7.2 Sensing Device and Adaptation Stage 31
2.7.3 Position and Power Measurement Principle 32
2.7.4 Post-Processing Signal Circuit Design 33
2.7.4.1 Block Diagram of the Post-Processing Signal Circuit 33
2.7.4.2 First Stage Design 33
2.7.5 Circuit Implementation 36
2.7.6 Performances and Features of the Post-Processing signal Circuit 39
2.7.7 Experimental Analysis of the Sensing System Noise 41
2.7.8 Achieved Resolution in Spot Displacement and Power Sensing 42
2.8 ELECTRICAL SET-UP II: DUT EXCITATION SYSTEM 43
2.8.1 General Description 43
2.8.2 Buck Converter 44
2.8.3 Gate-Drive Circuit 46
2.8.4 Synchronisation and Control Unit 47
2.9 CONCLUSIONS 48

CHAPTER 3 THERMAL CALIBRATION 51

3.1 INTRODUCTION 51
3.2 MOTIVATION 51
3.3 THE THERMAL TEST CHIP 52
3.3.1 Structure Description 52
3.3.2 TTC Simulated Thermal Behaviour 54
3.3.2.1 Temperature Increase Profile 54
3.3.2.2 Suitability of the Sensing Resistor 56
3.3.3 TTC Modelling 58
3.4 THE THERMAL CALIBRATION PROCEDURE 59
3.5 EQUIPMENT THERMAL CALIBRATION 61
3.5.1 Measured Signals and $(\partial n/\partial T)_C$ Selection 61
3.5.2 Temperature Rise Measurements 63
3.6 CONCLUSIONS 66

CHAPTER 4 FREE-CARRIER CONCENTRATION MEASUREMENTS ON DIODES 67

4.1 INTRODUCTION 67
4.2 LIFETIME KILLING METHODS 68
4.3 DIODE STRUCTURE AND EXPERIMENTAL CONDITIONS 69

4.3.1 Diodes Characteristics....69
4.3.2 Experimental Conditions....70
4.4 SIMULATION ASPECTS OF THE ANALYSED DIODES....71
4.4.1 Simulations Motivation....71
4.4.2 Considerations on Recombination Processes in Simulations....72
4.4.3 Stripe Diodes Preparation Effects on C....73
4.4.4 Simulation Procedure....75
4.5 FREE-CARRIER CONCENTRATION MEASUREMENTS....76
4.5.1 Time Evolution of Free-Carrier Concentration....76
4.5.2 Steady State Free-Carrier and Decay Time Profiles....77
4.6 CONCLUSIONS....81

CHAPTER 5 IIR-LD MEASUREMENTS ON IGBTS....83

5.1 INTRODUCTION....83
5.2 IMPORTANCE OF IGBTS IN POWER ELECTRONICS....83
5.3 PT-IGBTS STRUCTURE AND EXPERIMENTAL CONDITIONS....85
5.3.1 PT-IGBTS Caracteristics....85
5.3.2 Experimental Conditions....86
5.4 DEFLECTION SIGNALS SIMULATION....87
5.4.1 Motivation and Electro-thermal Simulation Conditions....87
5.4.2 Electro-thermal Simulation Results....87
5.4.3 Expected Deflection Signals....89
5.5 PERFORMED MEASUREMENTS....91
5.5.1 Bias Waveforms of the Analysed IGBTs....91
5.5.2 Measured Free-Carriers Evolution in the Drift Region....93
5.5.3 Temperature Gradient Comparison Depending on I_{Con}....94
5.5.4 Temperature Gradient Comparison Depending on t_{on}....95
5.5.5 Thermal Parameters Extraction....97
5.6 CONCLUSIONS....99

GENERAL CONCLUSIONS....101

APPENDIX A DERIVATION OF C AND $\nabla_y T$....107

A.1 INTRODUCTION....107
A.2 FREE-CARRIER CONCENTRATION EXPRESSION....108
A.3 REFRACTIVE INDEX GRADIENT DERIVATION....110
A.4 DECOUPLING $\nabla_y C(y, t)$ AND $\nabla_y T(y, t)$ FROM $\nabla_y n(y, t)$....114

LIST OF SYMBOLS....115

LIST OF ABBREVIATIONS **123**

BIBLIOGRAPHY **125**

Chapter 1

INTRODUCTION

1.1 Introduction

Power electronics is the key technology for managing electrical power efficiently. In this field, the used semiconductor devices (power diodes or controlled switches) are the main contributors to its expansion in the last years. As a consequence of the increasing power demand and reliability requirements on such devices, effective temperature management becomes ever more important, representing a central problem for power electronics. Another crucial issue is the time response of bipolar power devices. Different techniques, e. g., emitter and lifetime engineering, have been developed to improve it. However, they negatively contribute on the device self-heating problems. In this chapter, the reader is introduced to this topic showing the catastrophic effects of self-heating on power devices reliability. To study and minimise all these degradation problems, the temperature and free-carrier concentration measurements are required. For this reason, different methods for temperature and free-carrier concentration determination have been developed. The most commonly used in power devices are compared and discussed, giving a higher importance to laser probing techniques.

1.2 Power Devices Structure

According to the external controllability of power devices, they may be divided into diodes –PIN or Schottcky contacts– and power switches –MOSFETs, Thyristors, and IGBTs, as the most important ones–. Their common structural characteristics are

an optimised edge termination and low doped drift region (N^{-}), which allow them to support the blocking voltages usually required in power electronics (up to 10 kV). Furthermore, they incorporate two types of heavily doped zones, situated along each lateral side of the drift region. One of them injects free-carriers towards the drift region (emitter), whereas, the other one collects them (collector). Depending on the type of injected carriers (i. e., e^{-} or h^{+}), the emitter can be N^{+} or P^{+} doped. Thus, power devices may present one or both kinds of emitter, according to their conductive mechanism (i. e., unipolar or bipolar). An additional layer or diffused region could be present between the emitter and drift region controlling either the carrier injection level or device turn-on or turn-off. The latter can be tackled by various approaches –e. g., MOS-gated, current-controlled, or voltage drop of PN junction–, leading to the large family of power devices.

In all these devices, the drift region plays a prominent role. In the blocking state, the drift region absorbs the depletion layer originated from the reverse biased emitter-N^{-} junction, also fixing the breakdown voltage. Thus, the thicker this region is, the higher blocking voltages will be supported. However, as a consequence of the ohmic resistance introduced by this region during conduction state [1], the on-state power dissipation rises, especially in power MOSFETs. Therefore, a trade-off between breakdown voltage and on-state power dissipation must be achieved. Moreover, the thickness of the drift region also affects the switching device features. In bipolar power devices –such as PIN diodes, Thyristors, or IGBTs–, a high concentration of free-carriers is stored in this region during conduction state, due to the fact that the injected carrier concentration always is much higher than the doping level (high injection regime [1]) decreasing the drift region resistance (carrier conductivity modulation). Subsequently, after the turn-off instant, all the stored charge is not immediately removed, increasing the device turn-off time. Obviously, this effect is more important as drift region is thicker. This undesired phenomenon can be mitigated by using the emitter or lifetime engineering [2]. The former consists in adjusting the injection from a high doped layer or diffused region (injecting layer or region) by either varying its doping level or depth, or inserting a buffer layer. By

contrast, the latter controls the lifetime of injected carrier by introducing an appropriate spatial profile of stable point defects for enhancing carrier recombination. Nevertheless, both technological solutions also increase the on-state voltage drop, since they reduce the free carrier concentration in the drift region. Subsequently, a trade-off between turn-off switching and on-state power dissipation must also be obtained.

The common problem in all power devices is the heat dissipation produced within them due to their non-idealities. This dissipation is so important that their self-heating is one of the main drawbacks in power electronics. The different effects on the device reliability are discussed in the next section.

1.3 Self-heating Effects on Power Devices

Under typical working conditions (up to 10 kV and 6 kA), these devices dissipate a certain amount of electrical power in all their operation regimes, increasing the average value of its internal temperature. As a result, a complete degradation of the device performances and reliability would be obtained. Thus, to maintain its internal average temperature below a maximum value, the use of heat evacuation mechanisms based on thermal management strategies is crucial. However, with a standard heat dissipation system, it is not possible controlling local temperature rises due to electro-thermal coupling. Precisely, they activate and accelerate several physical degradation mechanisms, varying the electrical, structural, and mechanical properties of power devices. As a consequence, physical changes are induced to the die –e. g., burnout failures [3] or die cracking [4]– as well as in its package –e. g., bond wire fatigue [5] or die attach cracking [6]–. To better withstand such stressing conditions, power devices are designed improving their electro-thermal behaviour performing accurate simulations. Nonetheless, the simulation of their thermal failure phenomena requires transient temperature-field data for verification and improvement of the used model parameters. Therefore, in order to improve thermal management and study electro-thermal failure, the development of techniques and equipments allowing internal temperature measurements is required as a first step.

Moreover, the determination of free carrier concentration could be complementary to temperature measurement, since it can be used for adjusting simulation parameters, eventually improving the simulation results reliability. In the next section, thermometry techniques for power devices are reviewed. They are categorized depending on whether they employ electrical or optical signals. In the case of optical techniques, some of them also allow free carrier concentration measurement within power devices.

1.4 Thermometry Techniques in Power Devices

1.4.1 Electrical Methods

For a long time, thermometry in power devices, as well as in semiconductor devices in general, was based on the use of electrical thermo-sensitive parameters (TSP) [7]. The most used TSP in power electronics is the voltage drop of a PN junction forward biased by a low current level, since all power devices contain inherent PN junctions inside them. Apart from the voltage drop in the PN junction of a power diode, some examples are the voltage drop between collector-emitter terminals of a bipolar or IGBT in saturation regime. Other TSP very used in MOS-controlled power devices is the gate threshold voltage. Despite the fact that the threshold voltage response is less linear and sensitive than the forward biased PN junction one, it allows the extraction of a maximum operation temperature much more precise and accurate depending on the operation regimes of the device under test (DUT), e. g., short-circuit for IGBTs [8]. As major advantages of the TSPs use, temperature measurements can be performed on fully packaged devices with little or no modification, directly measuring the temperature within the device. However, an average value of device temperature is obtained, because of the calibration experimental conditions [9, 10]. This calibration is performed measuring the desired TSP once the whole device is heated and stabilised at a given steady-state temperature.

In order to improve the low spatial resolution presented by TSP-based techniques, temperature sensors are placed at the DUT inspection points by either monolithic integration or mechanical contact. In the first approach, PN junctions forward biased

by a low current [11] or resistors [12] are employed as a temperature sensor. However, sometimes the temperature measurement at the desired inspection point cannot be possible due to technological limitations. Moreover, when multiple sensors are required for measuring different inspection points, the packaging and device design complexity increase, the thermal mapping being unviable. Thus, this method is only useful for measuring the maximum temperature rise in operation conditions, as well as for protecting the device when a high temperature rise is produced.

Thanks to the recent advances in near-field microscopy, atomic force microscopes (AFM) allow the placement of a temperature sensor on the inspection point by mechanical contact, originating the scanning thermal microscopy (SThM) [13]. In this approach, the temperature sensor, e. g., Pt resistor [14] or thermo-couple [15], is at the AFM tip, which enormously facilitates the thermal mapping of the DUT top surface. This method shows the highest spatial resolution (around 30-100 nm) with a temperature accuracy of 1 mK [16]. These limitations on temperature extraction are due to the sensor nature, the AFM tip dimensions, and the roughness presented by the inspected device surface. Regarding the time response of this technique, a 5 μs resolution is achieved, because of the capacitive coupling between the tip and the device.

1.4.2 Optical Methods

Along the last 30 years, the dependence of material optical properties on temperature has suggested different thermometry techniques applicable to power devices. Basically, they may be categorized in surface thermal imaging (power radiation) or laser probing techniques. The former consists in determining the temperature distribution on the DUT top surface by means of a CCD camera. This process may be performed by either directly measuring the radiated heat flux with an IR-camera –infrared thermography (IRT) [17]–, or previously depositing a thermo-sensitive film on the inspected surface –liquid crystal thermography (LCT) [18] and fluorescence microthermography (FMT) [19]–. As a result, an image containing the surface thermal mapping of the DUT is recorded, in both cases, with the CCD

camera. Although IRT shows less spatial and temperature resolution (~5 μm and ~1 K) than LCT or FMT (~1 μm and ~50 mK), the commercial availability of IRT equipments, such as AGEMA Thermovision THV900 actually available at the CNM, has increased its use when measurements are not much restrictive. All these techniques are very useful for hot spot determination.

Concerning the laser probing techniques, they use as a probe a laser beam, where the thermo-sensitive magnitudes are its power, propagation direction, or phase. Thus, according to the monitored beam characteristic, the thermoreflectance (radiation power), Internal IR-Laser Deflection (beam deflection), and interferometric (phase shift) thermometry are distinguished. As a major goal, these techniques do not have physical contact with the device, eliminating the possibility of spurious influences of a probe on the temperature field. However, sometimes they require an extra step for DUT conditioning before the measurement.

In the thermoreflectance thermometry, a probe laser beam strikes on the DUT top. Due to the dependence of the surface reflectivity on temperature, the reflected beam experiences a variation on its radiation power, sensed by a photo-detector. This technique was initially used by Claeys et al [20] for fault detection in ICs, also allowing electromigration studies [21]. Abid et al. [22] applied this technique on power devices. They measured the temperature at several points on the top surface of a GTO, achieving a 20 μm spatial resolution with a minimum measured temperature increase of 10 K. The time resolution of this technique is ultimately limited to the order of the relaxation times associated with the microscopic scattering processes governing the reflectance, which is typically on the order of picoseconds in metals. On the other hand, its spatial resolution is limited by the diffraction of the probe beam, being comparable to the beam wavelength (<1 μm). However, its calibration is complex, due to surface non-uniformities and the presence of different materials on the device top.

In the laser beam deflection technique, the refractive index gradient and free carrier concentration is measured by the deflection and partial power absorption of a

probe laser beam passing through the device –internal IR-laser deflection (IIR-LD) [23]–. A refractive index gradient formed within the DUT alters the propagation direction of a beam (mirage effect). Detection of beam deflection yields information on the average temperature along a laser beam path through DUT. The average device temperature is deduced using independent data for the temperature dependence of the index of refraction and carrier-induced absorption. Among other problems, this approach includes the arduous sample preparation process, which is required to provide optical access to both sides of the device, and the difficulty of performing a precise calibration.

On the other hand, the interferometric thermometry consists in determining the phase shift between two or more beams. One of them is taken as a reference and the others go through or are reflected inside the DUT (sensing beams). As the refractive index depends on temperature (thermo-optical effect), the sensing beams find a variation on its optical path, inducing a phase shift respect to the reference beam. By superposing all the beams on a photo-detector, the phase shift is finally determined. The interferometric methods are the backside laser probing and Fabry-Perot thermometry.

In the backside laser probing, a sensing beam vertically traverses all the biased DUT until it is reflected at the top metallization, while the reference beam is reflected at the rear metallization layer of the DUT [24]. In this case, the detected phase shift has two contributions originated from the injection/removal of carriers and the temperature rise during the current pulse. Although they are opposite in sign, they are of the same order of magnitude as long as the power dissipated within the DUT is small. However, for a large temperature rise (e. g., IGBTs in short circuit operation), the phase modulation by the carriers can be neglected in view of the thermal contribution. This technique was used by Seliger et al. [25] and Fürböck et al. [26] for determining the temperature and free-carriers concentration at the channel of power MOSFETS and IGBTs, respectively. In order to provide full access through the DUT backside, a window of approximately 70×70 μm^2 must be opened in the

rear metallization layer. After that, an antireflective coating is deposited to suppress multiple reflections within the substrate [27]. Its spatial resolution is limited by the laser spot size to approximately 2 μm. Although only integral information on the vertical profiles is provided, this technique constitutes a useful characterization method for vertical MOS-gated switches, since it is capable of detecting large temperature rises of 100 K or more.

The Fabry-Perot interferometry takes advantage of the multiple secondary beams, resulting from the probe beam (main ray) reflections on either the opposite lateral sides [28] –Fabry-Perot transmission (FPT) measurements– or an internal layer –Fabry-Perot reflectivity (FPR) measurements– of the DUT. In such a situation, the device is behaved as a Fabry-Perot resonator cavity whose optical path is affected by modulations of the refractive index. All the different beams are superposed on the surface of a photo-detector obtaining the time evolution of the interfering signal. Seliger et al. performed Fabry-Perot reflectivity measurements on lateral power MOSFETs [29]. Although reported works on Fabry-Perot transmission measurements are not found in the literature, they could be applied on vertical power devices. For FPT, a 5 μm spatial and 10 K temperature resolution are achieved, being possible to measure temperature increases up to 300 K or more.

1.5 Scope and Structure of this Thesis

From all these reported techniques, this thesis covers the development of an experimental rig for temperature and free carrier concentration measurement in power devices, based on internal IR-laser deflection (IIR-LD) technique. IIR-LD allows a complete characterisation of power devices, extracting from the device its temperature gradient and free carrier concentration. This technique has been chosen over the other ones, because of its higher precision, its greater versatility and lower complexity. Moreover, at the Centre Nacional de Microelèctronica, an IRT and SThM equipment are available. Thus, with this new equipment, the thermal

characterisation area of power devices will be drastically improved, also allowing free carrier measurements.

This thesis is organized in two main parts. The first one details the physical insights of IIR-LD, developed equipment (chapter 2) and followed thermal calibration procedure based on a thermal test chip (chapter 3). By contrast, the second part reports measurements performed with the IIR-LD equipment on power diodes (chapter 4) and IGBTs (chapter 5). In both chapters, the difference in behaviour between unirradiated and irradiated devices is used to demonstrate the functionality of the developed equipment. Concretely, chapter 4 compares the measured free-carrier concentration between unirradiated and irradiated power diodes, and chapter 5 shows measurements performed in a very thin region inside an irradiated and unirradiated PT-IGBT, where the thermal behaviour is also contrasted and analysed.

Chapter 2

THE EXPERIMENTAL RIG

2.1 Introduction

This chapter describes the designed and developed IIR-LD experimental rig. All different considerations taken in its design are further explained and discussed.

This method has been chosen for its higher precision, greater versatility, and lower complexity in comparison to the other optical probing techniques introduced in the previous chapter. Moreover, a brief analysis of the physical principles of this technique has also been carried out. Thus, the plasma-optical and thermo-optical effects are revisited analysing the more interesting points. Both effects demonstrate that the electronic phenomena, jointly with temperature, influence the optical properties of materials.

2.2 Operation Principle of Laser Probing Techniques

2.2.1 Dependence of Optical Properties

The optical properties of Silicon may be modulated by variations on its electronic properties, governed by free carrier concentration (plasma-optical effects) and temperature variations (thermo-optical effects). These modulations on refractive index, Δn, and absorption coefficient, $\Delta\alpha$, may be formally written in terms of free carrier and temperature variation, ΔC and ΔT, as:

$$\Delta n(C,T) = \left(\frac{\partial n}{\partial C}\right)_T \Delta C + \left(\frac{\partial n}{\partial T}\right)_C \Delta T \tag{2.2.1}$$

$$\Delta \alpha(C,T) = \left(\frac{\partial \alpha}{\partial C}\right)_T \Delta C + \left(\frac{\partial \alpha}{\partial T}\right)_C \Delta T \tag{2.2.2}$$

where $(\partial n/\partial C)_T$, $(\partial n/\partial T)_C$, $(\partial \alpha/\partial C)_T$, and $(\partial \alpha/\partial T)_C$ are the various proportionality coefficients, relating both coupled effects with refractive index and absorption coefficient. In bipolar devices, the free-carriers cannot be distinguished between them, i. e., electrons or holes, using the optical techniques previously mentioned. For this reason, the free-carriers are not distinguished in the notation of equations (2.2.1) and (2.2.2). From the physical point of view, these coupling effects are discussed for the case of bipolar Silicon power devices. Also, the values for all these proportionality coefficients will be reported.

2.2.2 Plasma-Optical Effect

Within a drift region of a power semiconductor device, the free carrier concentration can be thermally generated from the background doping level (impurity ionization) [30] or externally injected from emitter regions (heavier doped regions). For the usual working temperatures of such devices (150 - 450 K, approximately), the free-carriers coming from the ionized impurities remain constant with a concentration equal to the background doping one [30]. Optically, it does not make much difference whether carriers come from impurity ionization or from injection [31]. As a first approximation, the Drude's semi-classical model of radiation absorption in metals is extensively used with some modifications [32, 33]. From this model, the refractive index n and absorption coefficient α may be expressed in terms of the radiation wavelength λ and free carrier concentration, i. e., electrons concentration C_n and holes concentration C_p:

$$n = n_0 - \frac{q^2 \lambda^2}{8\pi^2 \varepsilon_0 n_0 v_c{}^2}\left(\frac{C_n}{m_n^*} + \frac{C_p}{m_p^*}\right) \tag{2.2.3}$$

$$\alpha = \frac{q^3\lambda^2}{4\pi^2\varepsilon_0 n_0 v_c^{\ 3}}\left(\frac{C_n}{m_n^{*2}\mu_n}+\frac{C_p}{m_p^{*2}\mu_p}\right) \qquad (2.2.4)$$

where m^*_n (m^*_p) is the effective mass of electrons (holes), μ_n (μ_p) represents the mobility of electrons (holes), and the physical constants n_0, q, v_c, ε_0 correspond to the refractive index of the unperturbed material, the electronic charge, the light velocity, and the permittivity of free space, respectively. This theory predicts a linear relationship between optical parameters and free-carriers concentration and a quadratic dependence on λ (λ^2-law). Moreover, a higher effectiveness of free electrons in perturbing the refractive index is shown, obtaining the opposite effect for the absorption coefficient, due to $m^*_n<m^*_p$ and $m^{*2}_n\mu_n>m^{*2}_p\mu_p$. However, this model does not take into account the effect of ionized impurities scattering.

Following a quantum-mechanical approach, Huang et al. [34] theoretically studied the influence of ionized impurities scattering on n and α, ranging the background doping concentration from 10^{15} cm^{-3} to 10^{18} cm^{-3} for two wavelengths, λ=1.3 μm and λ=1.6 μm, usually used in integrated optics and optical probing applications. They also considered all scattering processes with the lattice (phonons). As noticeable results, they obtained the same trends inferred from equations (2.2.3) and (2.2.4), but with lower values, when a lightly doped region (10^{16} cm^{-3}) is highly injected with free-carriers (10^{16}-10^{18} cm^{-3}). On the contrary, for a heavier doping concentration (10^{18} cm^{-3}), they found that the refractive index depends on free-carriers as $C_n^{0.91}$ and $C_p^{0.8}$, being more sensitive to free electrons variations than to free holes. They attribute this observed difference in behaviour to the partial ionization of impurities, which takes more relevance in the second case because of the higher concentration of thermally generated free-carriers. These last results agree with the experimental ones reported by Soref and Bennett [31], who collected experimental data about the absorption spectra of heavily doped samples and calculated the refractive index. Therefore, for usual power devices working conditions, optical properties of Silicon are linearly related with free carrier concentration under high injection conditions.

Table 2.1 contains a comparison of several values for each plasma-optical coefficient. All these values are extracted from the reported ones in [27] and they are determined under high injection condition ($C_n = C_p = 1\times10^{16}$ cm^{-3}), at room temperature (T= 300 K) and λ=1.3 µm. As for $(\partial n/\partial C)_T$, its reported values show a great variation. Nevertheless, this fact is not a great drawback, since $(\partial n/\partial T)_C$ predominantly modulates n at the usual operation conditions of power devices [27]. Concerning $(\partial\alpha/\partial C)_T$, a great similarity between the experimental results of Huang, Soref, and Horwitz is observed, whereas the Schierwater's and Schlögl's ones differ from the other results by a factor of 2, approximately. All these differences are related to the experimental working conditions. The selected value in this work will correspond to Schlögl's one, as further argued in Chapter 4.

Literature Resources	$(\partial n/\partial C)_T$ [cm^3]	$(\partial\alpha/\partial C)_T$ [cm^2]	*Data Procedence*
Drude Model [27]	-1.40×10^{-21}	6.42×10^{-19}	Theoretical
Huang et al. [34]	-4.36×10^{-22}	5.11×10^{-18}	Theoretical
Soref, Bennet [31]	-3.57×10^{-21}	5.92×10^{-18}	Experimental
Schierwater [35]	———	2.80×10^{-18}	Experimental
Horwitz, Swanson [36]	———	4.85×10^{-18}	Experimental
Deboy [37]	-4.58×10^{-21}	———	Experimental
Hille et al [38].	-1.81×10^{-21}	———	Experimental
Schlögl [39]	———	8.08×10^{-18}	Experimental

Table 2.1. *Reported values for both plasma-optical coefficients $(\partial n/\partial C)_T$ and $(\partial\alpha/\partial C)_T$ when $C_n = C_p = 1\times10^{16}$ cm^{-3}, at room temperature (T = 300 K) and λ=1.3 µm.*

2.2.3 Thermo-Optical Effect

Concerning the thermal effects on optical properties of Silicon, the temperature modulates the band gap energy and the probability distribution function of free-carriers and phonons [40]. Subsequently, the transitions between the valence, impurity and conduction bands (inter-band transitions), as well as the transitions within their sub-bands (intra-band transitions), are controlled by this parameter. As a consequence of the usual temperature working conditions of power devices, only the free carrier absorption is enhanced, since the other ones do not practically affect in this temperature range [41]. Consequently, under high injection conditions, the

injected carriers predominantly contribute in the absorption process; owing to the thermally generated free-carriers remain constant and approximately equal to the ionized impurities concentration. From experimental results, Sturm and Reaves [41] obtained a linear dependence on temperature of the absorption coefficient due to free-carriers in the range from 500ºC to 800ºC. However, this contribution to absorption coefficient is insignificant in comparison to the free-carrier concentration one, being negligible in the working temperature conditions of power devices [27].

The temperature dependence of refractive index was experimentally adjusted by Magunov [42], using the following expression:

$$n(\lambda,T)= n_0 + b\,T+ c\,T^2+ (d+e\,T+f\,T^2)\,\lambda^{-a} \qquad (2.2.5)$$

where a, b, c, d, e, and f are fitting parameters. In the case of Silicon, the quadratic term can be ignored, since it does not practically contribute on refractive index variations for the considered temperature range. On the other hand, G. Gosh [43] assumed a linear relation between refractive index and temperature. Analytically, he derived an expression for the proportionality factor in terms of the linear expansion coefficient, related with the acoustic phonons, and the variation of the diagram band on temperature. Its model results agree with the experimental data collected by H. H. Li [44]. H. H. Li searched, compiled and analysed the refractive index data and its temperature derivative in the wavelength and temperature ranges 1.2 – 14 μm and 100 – 740 K, respectively, recommending which is the best value in each case. Furthermore, in this reference, the different techniques employed for measuring $(\partial n/\partial T)_C$ are reported, as well.

Since temperature contribution to α may be neglected, the coefficient $(\partial n/\partial T)_C$ will be referred from now onwards as thermo-optical coefficient. Table 2.2 shows several values reported from the literature at λ=1.3 μm. It can be observed that the values from Bertolotti et al., Magunov, and Li differ within its experimental error (20% in the worst case). However, Seliger et al. and Hille et al. obtained a measured value lower than the other ones. This difference may be due to the followed

procedure for the determination of $(\partial n/\partial T)_C$. In the first case, the refractive index and temperature are simultaneously measured in Silicon samples; whereas, in the second case, a FPI equipment is calibrated using power MOSFETs finding $(\partial n/\partial T)_C$ by simulation. Between both procedures, the latter seems to be less reliable, because it is derived from non direct measurements.

Literature resources	$(\partial n/\partial T)_C$ [K^{-1}]	*Temperature Range*	*Data procedence*
Magunov [42]	2.0×10^{-4}	Room Temperature	Theoretical
Bertolotti et al. [45]	1.8×10^{-4}	15ºC – 35ºC	Experimental
Li [44]	1.9×10^{-4}	Room Temperature	Experimental
Seliger et al. [46]	1.6×10^{-4}	Room Temperature	Experimental
Hille et al. [38]	1.6×10^{-4}	25ºC – 150ºC	Experimental

Table 2.2. *Reported values for the thermo-optical coefficient* $(\partial n/\partial T)_C$ *at* λ*=1.3 µm.*

2.3 IIR-LD Technique Description

In the IIR-LD technique, an IR-laser probe beam goes through a biased device, striking on its lateral sides perpendicularly. Once the device is in conduction state, it shows free carrier injection in the drift region, originating the plasma-optical effect, and self-heating, causing the thermo-optical effect. Both effects produce a partial absorption (due to free-carriers) and deflection ("Mirage" effect) on the probe beam. "Mirage" effect lies in changes on Silicon refractive index as a consequence of both internal gradients of free-carriers concentration and temperature. This interaction is shown in Figure 2.3.1.

The viability of the IIR-LD depends on the doping level of the inspected layer and the lateral dimensions of the studied device. For doping levels higher than 1×10^{19} cm^{-3} [31] and device lateral dimensions larger than 2 mm, the IR-radiation is completely absorbed by the background free-carriers. For this reason, the free carrier concentration must be measured only in the low doped layer of bipolar power devices, where the high injection condition is reached during the device conduction state. In this situation, the free carrier concentration level is higher than the

background doping one, and, therefore, free carrier contribution to the induced variation in the IR-radiation power signal at turn-on and turn-off instants may be measured. To enhance the radiation transmission through the DUT, its lateral sides are polished until an optical quality is obtained.

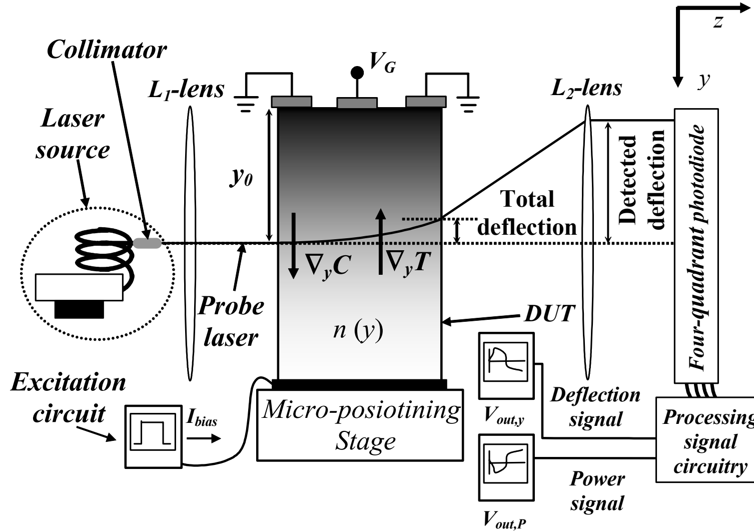

Figure 2.3.1. *Free-carriers and temperature gradient interaction with the probe laser beam in the IIR-LD technique.*

From the measurement of the transmitted power radiation and the beam deflection, it is possible to deduce a longitudinal averaged value for free carrier concentration and temperature gradients at a given depth y_0 (inspection depth) from the surface. Assuming an exponential decay of the transmitted radiation power with distance, the free carrier concentration at the inspection depth can be calculated from the variation between transmitted power during on- and off-state [47]. The corresponding expression is:

$$C = \frac{1}{L\left(\frac{\partial \alpha}{\partial C}\right)_T} Ln\left(\frac{V_{out,P_0}}{V_{out,P}}\right) \tag{2.3.1}$$

where L represents the length of interaction between the beam and DUT, $V_{out,P0}$ and $V_{out,P}$ denote the power signal detected when the device is in off-state and time evolution of the power signal, respectively.

From the deflection signal $V_{out,y}$, the refractive index gradient $\nabla_y n$ may be deduced from the geometrical ray tracing along the optical set-up (see Appendix A), giving:

$$\nabla_y n = \frac{NA \ V_{out,y}}{\kappa' L\left(\dfrac{L}{2 f_{L_2} n_0} + 1\right)} \tag{2.3.2}$$

where NA is the beam numerical aperture, f_{L_2} expresses the focal length of L_2-lens, and κ' corresponds to a calibration factor from the power and deflection sensing system, described further on. Remembering that $\nabla_y n$ may be expressed by:

$$\nabla_y n = \left(\frac{\partial n}{\partial C}\right)_T \nabla_y C + \left(\frac{\partial n}{\partial T}\right)_C \nabla_y T \tag{2.3.3}$$

Subsequently, the temperature gradient may be expressed as:

$$\nabla_y T = \frac{\nabla_y n - \left(\dfrac{\partial n}{\partial C}\right)_T \nabla_y C\Big|_{num}}{\left(\dfrac{\partial n}{\partial T}\right)_C} \tag{2.3.4}$$

yielding this final equation:

$$\nabla_y T = \frac{NA \ V_{out,y}}{\kappa' L\left(\dfrac{L}{2 f_{L_2} n_0} + 1\right)\left(\dfrac{\partial n}{\partial T}\right)_C} - \frac{\left(\dfrac{\partial n}{\partial C}\right)_T \nabla_y C\Big|_{num}}{\left(\dfrac{\partial n}{\partial T}\right)_C} \tag{2.3.5}$$

where $\nabla_y C|_{num}$ makes reference to the resulting gradient of free-carriers concentration numerically determined from C measurements at several inspection

depths, thus decoupling the effect of $\nabla_y C$ and $\nabla_y T$ on $V_{out,y}$. However, when the spot dimensions are similar to the inspected layer thickness, equation (2.3.5) is not applicable since IIR-LD measurements may be performed at only one inspection depth. In such situations, a time criterion consisting in the difference between time responses of both gradients must be followed. $V_{out,y}$ only depends on $\nabla_y C$ at the initial time instants ($t \approx 5$ μs), because $\nabla_y C$ rapidly reaches steady-state value whereas $\nabla_y T$ is negligible, as it will be discussed in Chapter 5. Taking into account this approximation, the temperature gradient is given by:

$$\nabla_y T = \frac{NA\,\left(V_{out,y} - V_{out,y}(t = 5\ \mu\mathrm{s})\right)}{\kappa' L\left(\dfrac{L}{2 f_{L_2} n_0} + 1\right)\left(\dfrac{\partial n}{\partial T}\right)_C} \tag{2.3.6}$$

where $V_{out,y}\,(t = 5$ μs) is the deflection signal value at the instant time $t = 5$ μs, which is subtracted to $V_{out,y}$.

2.4 Experimental Rig

The three main functional set-ups of the system and all their elements are shown in Figure 2.4.1. Firstly, the optical set-up consists of an IR-laser source and an optical system, formed by two lenses (L_1 and L_2) and a beam collimator. Secondly, the mechanical set-up is constituted by micro-positioning stages, adapting mechanical pieces and an optical breadboard. Thirdly, the electrical set-up consists of the power and deflection sensing system, DUT excitation system (power pulse generator), and acquiring signal equipment. The power and deflection sensing system is formed by a four-quadrant photodiode sensor (FQP), I/V converter (FQP preamplifier), and post-processing signal circuit. Concerning the acquiring equipment, an A6312 Tektronix Hall Effect current probe (with a bandwidth of 100 MHz), along with its AM 503B Tektronix amplifier, and a TDS 744A four channel digitizing oscilloscope perform the measurement of the biasing current and all output signals of the sensing system, respectively. In the next subsections, the main functional parts of the experimental rig will be described in more detail.

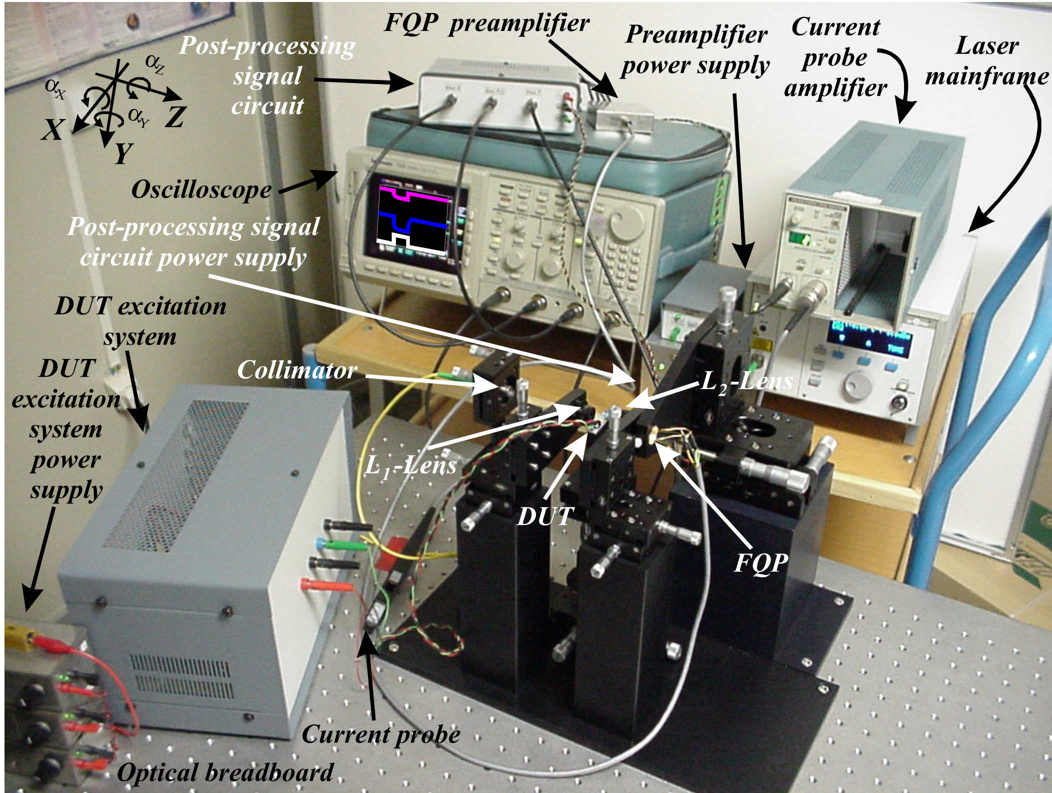

Figure 2.4.1. *Experimental rig phototgraph.*

2.5 Optical set-up

2.5.1 The laser probe beam

2.5.1.1 The Beam Waist: Spatial Resolution in IIR-LD Measurements

The beam waist [48] consists in the dispersion experienced by the diameter of a collimated laser beam along its propagation direction, as described for the following equations:

$$I(r,z) = I_0 \left[\frac{W_0}{W(z)} \right]^2 \exp\left[-\frac{2r^2}{W^2(z)} \right] \tag{2.5.1}$$

$$W(z) = W_0 \left[1 + \left(\frac{z}{z_0} \right)^2 \right]^{1/2} \tag{2.5.2}$$

$$W_0 = \left(\frac{\lambda \, z_0}{n_0 \, \pi} \right)^{1/2} \tag{2.5.3}$$

$$W_0 = \frac{\lambda}{\pi \, NA} \tag{2.5.4}$$

where z is the beam propagation direction, $I(r,z)$ and I_0 denote the laser intensity along the propagation direction and its maximum value, respectively, $W(z)$ and W_0 correspond to the beam radius along the propagation direction and the minimum radius, respectively, z_0 represents a characteristic distance where the beam diameter increases a 40% (*Rayleigh distance*), and NA indicates the beam numerical aperture, defined as the ratio between the beam radius and the focal length of a given lens.

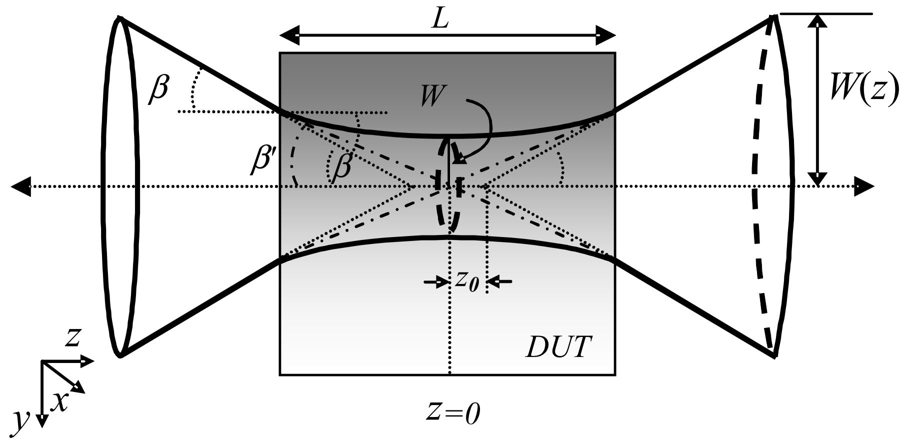

Figure 2.5.1. *Sketch of a laser beam traversing the analysed DUT, showing the main beam parameters.*

Figure 2.5.1 shows all geometrical parameters involved in equations (2.5.1)-(2.5.4). In this figure, it can also be observed that the beam diameter experiences the confinement of its radius due to differences between the refractive index of the two involved media, i. e., air and Silicon. This effect introduces two angles (β and β') related by Snell's law.

As a main requirement, the beam diameter (ϕ) must be approximately constant inside the DUT to achieve a uniform interaction of the laser beam with $\nabla_y n$ and C. This condition will be accomplished minimising the beam diameter on the DUT lateral sides once it is focused in the middle of the DUT, i. e.:

$$\frac{d}{d\phi}\left(W^2\left(z=\frac{L}{2}\right)\right)=0 \tag{2.5.5}$$

by applying the Leibniz rule to (2.5.5), it is derived that:

$$\frac{d}{dW_0^2}\left(W^2\left(z=\frac{L}{2}\right)\right)\frac{d}{dNA}\left(W_0^2\right)\frac{d}{d\phi}(NA)=0 \tag{2.5.6}$$

the previous condition is satisfied if:

$$\frac{d}{dW_0^2}\left(W^2\left(z=\frac{L}{2}\right)\right)=0 \tag{2.5.7}$$

inferring the following result from (2.5.2):

$$1-\frac{\left(\dfrac{\lambda\, L/2}{\pi\, n_0}\right)^2}{W_0^4}=0 \tag{2.5.8}$$

deducing that W_0 is:

$$W_0=\sqrt{\frac{\lambda\dfrac{L}{2}}{\pi\, n_0}} \tag{2.5.9}$$

by substituting (2.5.9) into (2.5.4), the following equation for an optimum NA ($NA|_{opt}$) accomplishing the aforementioned restrictions is inferred:

$$NA\Big|_{opt} = \sqrt{\frac{\lambda\, n_0}{\pi \frac{L}{2}}} \qquad (2.5.10)$$

Considering (2.5.3) and (2.5.4), this result corresponds to evaluate *NA* at z_0=*L*/2. By means of equation (2.5.10), it is possible to fix a criterion for the selection of the collimator and L_1-lens used in this experimental rig, as will be shown further on.

The spatial resolution in the performed measurements (i. e., radiation power and deflection) depends on the average value of beam diameter along *L* (ϕ'), since it fixes an average cross section during its interaction with the DUT. Moreover, the used probe beam also introduces a spatial error related to its radius average value along *L* (*W*'). By using equations (2.5.2)-(2.5.4), both the spatial error and resolution may be estimated. Assuming that the laser is focused in the middle of the DUT, the spatial error is calculated as:

$$W' = \frac{1}{L}\int_{-L/2}^{+L/2} dz\; W(z) \qquad (2.5.11)$$

eventually obtaining:

$$W' = W_0 \frac{z_0}{L}\left[arcSinh\left(\frac{L}{2z_0}\right) + \frac{L}{2z_0}\sqrt{1+\left(\frac{L}{2z_0}\right)^2}\right] \qquad (2.5.12)$$

Equation (2.5.12) demonstrates the dependence between the achieved spatial resolution and DUT length. When $NA=NA|_{opt}$, equation (2.5.12) can be rewritten as:

$$W'(NA\,|_{opt}) = \frac{arcSinh\,(1) + \sqrt{2}}{2}\sqrt{\frac{\lambda \frac{L}{2}}{\pi\, n_0}} \approx 1.15\sqrt{\frac{\lambda \frac{L}{2}}{\pi\, n_0}} \qquad (2.5.13)$$

In both situations, the theoretical achieved resolution will be twice *W'*. Figure 2.5.2 depicts the dependence of *W*' ($NA|_{opt}$) on *L*. For typical dimensions of power devices,

i. e., L ranging from 5 mm to 10 mm, Figure 2.5.2 shows how the spatial error increases from 20 μm to 28 μm, approximately. Therefore, it is possible finding a beam numerical aperture which would allow measurement of power devices with different lengths without excessively varying W', as shown further on.

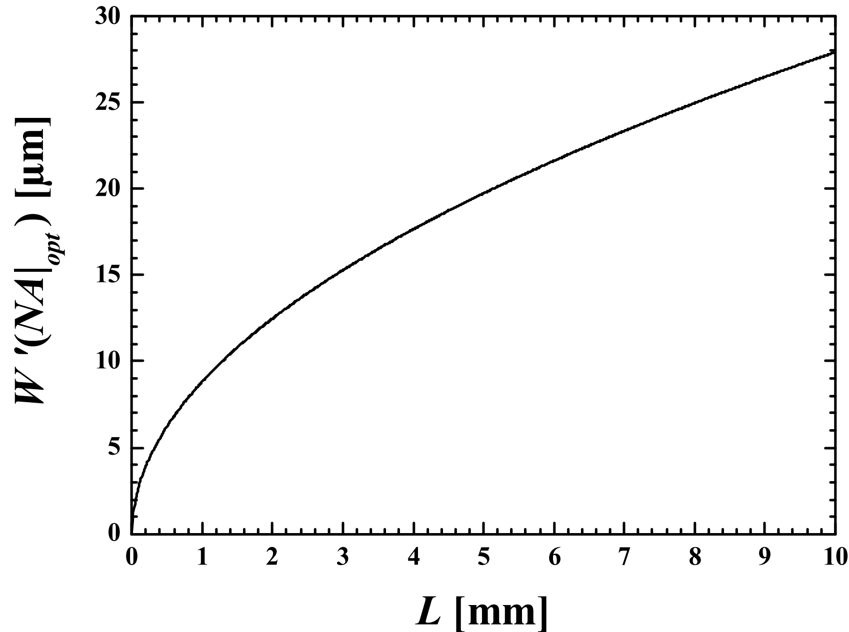

Figure 2.5.2. *Average value of the beam radius as a function of L, when* $NA = NA|_{opt}$.

2.5.1.2 Radiation Source Selection

Concerning the laser source characteristics, a 1315 nm wavelength (near-IR) semiconductor laser has been chosen. At this wavelength, inter-band optical transitions of free-carriers are avoided, as well as the required values for thermo-optical and plasma-optical coefficients can be easily found in the literature. In this IIR-LD set-up, the working power of the laser source is 2 mW. As a radiation source, a laser module from Profile (serial reference LS-81310DFBi-10) is used. It consists in a laser diode emitting by distributed feedback (DFB). In comparison to the conventional diodes, DFB laser diodes present a non-planar PN junction which improves its monochromaticity [49]. Its power is adjustable between 1 mW to 10 mW and operates in CW mode. Moreover, this module has an output connectable to an optical fibre (connection FC/APC). This module is mounted inside a mainframe (Profile PRO-800), which controls the radiation power and the diode temperature.

2.5.2 Optical System Design and Implementation

2.5.2.1 Collimator and L_1-lens Selection and Obtained Performances

As previously stated, the collimator determines the beam diameter on the L_1-lens surface, whereas the L_1-lens establishes the focal length. Consequently, they fix NA. Furthermore, both optical elements have been chosen for analysing DUTs with dimensions ranging from 5×5 mm^2 to 10×10 mm^2, very usual in power devices as IGBTs or MOSFETs. According to equations (2.5.10) and (2.5.13), $NA|_{opt}$ values must be comprised between 17×10^{-3} and 24×10^{-3} for the mentioned DUT dimensions, implying that the average value of the beam diameter will range from 40 µm to 56 µm. Figure 2.5.3 (a) and (b) depicts all this information.

In Figure 2.5.3 (a), the variation of the probe beam diameter on the chip lateral side (ϕ_{LatDUT}) as a function of NA for different values of L is shown. Besides, the minimum of each curve, together with equation (2.5.10), are also plotted. In this graph, the shrinkage of $NA|_{opt}$ when L increases, as well as a higher sensitivity of ϕ_{LatDUT} under variations of NA around the ϕ_{LatDUT} minimum, are evidenced. Moreover, it can be observed that both tendencies are minimised for NA=20×10^{-3}.

On the other hand, Figure 2.5.3 (b) illustrates the dependence of ϕ' on NA, also stressing ϕ' values achieved in the considered range of L when ϕ_{LatDUT} takes its minimum value. Notice that, for a $NA=20\times10^{-3}$, ϕ' varies from 44 µm to 52 µm within the selected range of L. From these results, a collimator from Optics Research (model CFC-2-IR1) and a lens from Newport (reference F-L10B) are selected, which theoretically provides a NA=21×10^{-3}. Both optical elements have antireflective coatings to enhance the radiation transmission at the working wavelength. The collimator assures a parallel beam with a 0.5 mm diameter, within a distance comprised from 2 mm to 20 mm. The F-L10B lens has a 12 mm focal length, 6 mm working distance, and 0.25 numerical aperture.

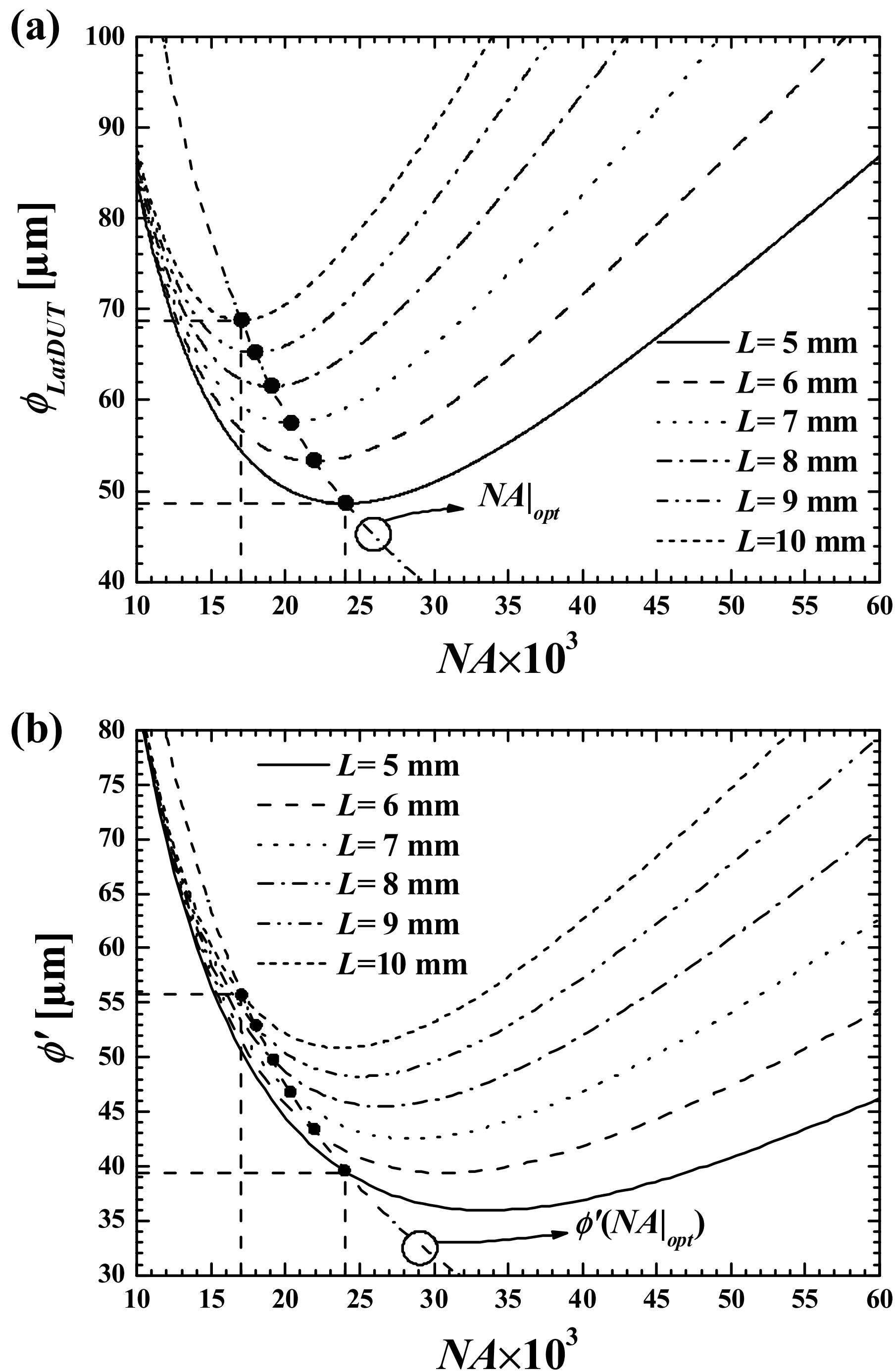

Figure 2.5.3. (*a*) *Variation of the probe beam diameter on the chip lateral side as a function of the beam numerical aperture for λ=1.3μm and different values of L, showing the minima corresponding to each case.* (*b*) *Variation of the beam diameter average value along L as a function of the beam numerical aperture, also stressing the reachable values for L=5 mm and L=10 mm by means of equation* (2.5.10).

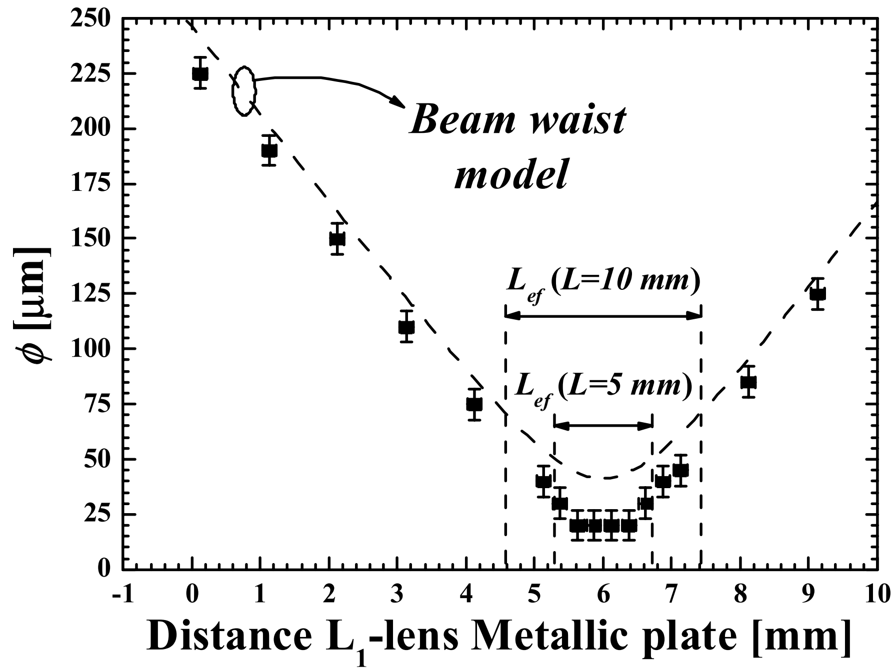

Figure 2.5.4. *Comparison between measured and predicted beam diameters, stressing L_{ef} where the optical set-up has been optimised.*

The beam diameter resulting from these two elements is experimentally determined. For this purpose, a thin metallic plate is interposed along the beam path. By vertically displacing it, variations on the detected power are induced. Since the laser beam presents a Gaussian profile, the beam diameter is defined as the vertical displacement required by the metallic plate, which induces a variation on the total detected power within the range of 86.5% - 13.5% [50]. Figure 2.5.4 depicts the comparison between the measured beam diameter and model prediction (equations (2.5.2)-(2.5.4)) for $NA=20\times10^{-3}$, illustrating as well the effective length (L_{ef}) where DUT and beam interact. L_{ef} accounts for the effect of material refractive index on L when a laser beam goes through the DUT, providing the effective length of the interaction between them ($L_{ef}=L/n$). From Figure 2.5.4, both beam shapes present the same trends, excessively not differing between them. Experimentally, a $NA = (19.89\pm0.49)\times10^{-3}$ and 20±7 μm minimum beam diameter are determined. For the lateral dimensions range of power devices previously considered (5-10 mm), ϕ_{LatDUT} along with the achieved spatial resolution and error are experimentally

extracted from Figure 2.5.4, as well. ϕ_{LatDUT} varies within 35-57 μm, whereas the spatial resolution is comprised in the 22-32 μm range, establishing from 11 μm to 16 μm the spatial error.

2.5.2.2 L_2-lens Selection and Results

The L_2-lens fixes the beam diameter on the detector. For this reason, the selection of such lens is constrained by the maximum displacement of beam spot on the chosen FQP (2 mm), which is limited by the sensor lateral dimensions. Subsequently, the maximum focal length of L_2-lens ($f_{L_2}|_{\max}$) can be obtained from:

$$f_{L_2}|_{\max} = \frac{\phi_{FQP,\max}}{2NA} \tag{2.5.14}$$

where $\phi_{FQP,\max}$ is the maximum beam spot diameter on the sensor. In the present work, taking $\phi_{FQP,\max}$ =2 mm and NA=20×10^{-3}, $f_{L_2}|_{\max}$ =50 mm is found. Comparing various lenses commercially available, the lens F-L10B is selected, since it has a 25.6 mm focal length, a 19.95 mm working distance, and a 0.156 numerical aperture, as well as a good transmission at the working wavelength. It has been experimentally determined that this lens assures on the FQP a 1 mm beam spot, approximately. The method consisted in displacing along one direction (x or y) the FQP in such a way that the spot will impinge out of the active region, obtaining a decrease in the sensed radiation power. Following the criterion on radiation power variation previously stated, the beam diameter is measured.

2.6 Micro-Positioning Displacement Modules

The IIR-LD experimental rig has been divided in six displacement modules corresponding to each element which actively interacts with the IR-laser beam, i. e., the collimator, L_1-lens, DUT, L_2-lens, and FQP. Thus, their alignment in the same optical axis, as well as the DUT positioning during the measurements, is facilitated. Each module is formed by various micro-positioning stages and adapting mechanical pieces. The latter make functions of supporting and fixing both the micro-positioning

stages and the mentioned optical elements. For this reason, they are made of aluminium, because it provides the required rigidity and stability for the present application. As main common characteristics, they present three degrees of freedom corresponding to the coordinates X, Y, and Z, as shown in Figure 2.6.1. In the case of the DUT module, three angular degrees of freedom (α_X, α_Y, α_Z) are also included to assure that the beam strikes on the DUT lateral sides perpendicularly. Concerning the collimator module, it presents two additional angular degrees of freedom (α_X, α_Y) facilitating the system alignment.

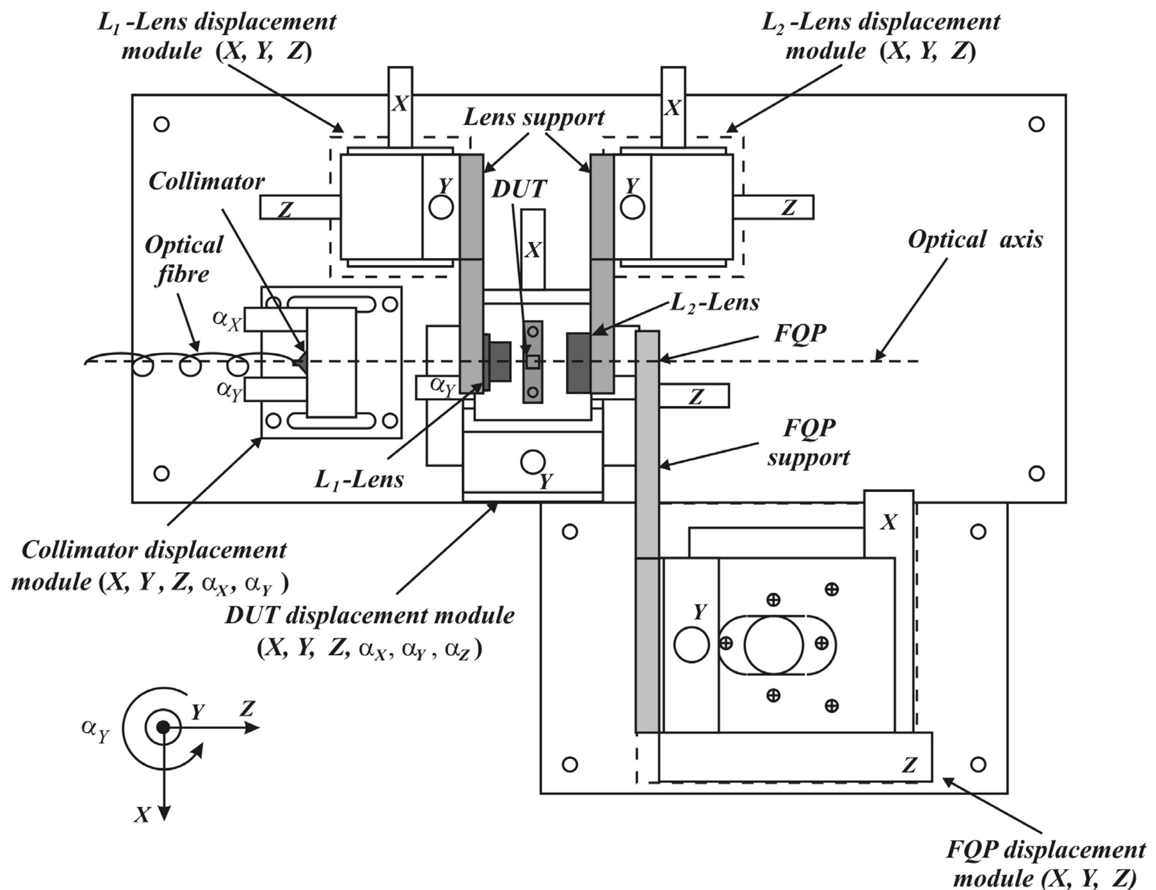

Figure 2.6.1. *Top view of the positioning system schematic, stressing its several parts.*

The uncertainty in the optical centring process is ±5 μm, whereas in the DUT positioning it is ±7 μm. The former is directly given by the micrometers resolution of the micro-positioning stages; while the latter is determined by applying uncertainties propagation formula since a differential measurement (incremental displacement) is

performed. Namely, the uncertainty in DUT positioning will be $(5^2+5^2)^{1/2} = \pm 7$ µm, being very similar to the spatial error originated by the beam probe. In order to isolate the experimental rig from environmental mechanical vibrations, all the displacement modules are supported on a 900×900 mm^2 optical breadboard manufactured by *Melles Griot* with a passive shock absorber system (*Pump & Go*®) and a beehive internal structure, assuring a vertical and horizontal resonance frequency of 3.5 Hz.

2.7 Electrical set-up I: Power and Deflection Sensing System

2.7.1 System Description and Constraints

The designed system consists of a Germanium FQP as a sensing device, a FQP pre-amplifier as an adaptation stage, and a post-processing signal circuit, as shown in Figure 2.7.1. During the measurement process, an IR-laser spot strikes on the FQP surface, generating four photocurrents I_{Qj} where the j subscript denotes the quadrant number. Afterwards, the current signal is pre-amplified and converted to a voltage V_{Qj}. Finally, the post-processing signal circuit obtains $V_{out,P}$, $V_{out,y}$, and $V_{out,x}$.

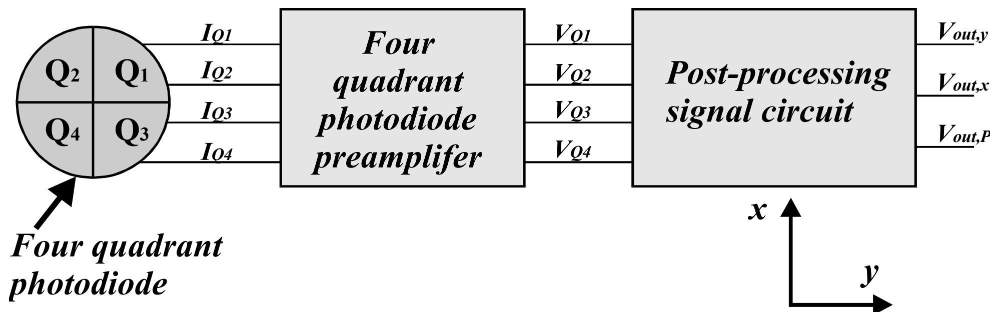

Figure 2.7.1. *Block diagram of the whole sensing system, showing its main variables.*

The system bandwidth, radiation working wavelength, and noise level establish the limitations for the whole system design. These parameters are restricted by the characteristics of the analysed DUTs, jointly with the desired resolution in the performed measurements. Thus, as the free carrier time response is within the range

of 1-5 μs for the analysed power devices [51], the system bandwidth must be at least 1 MHz. Moreover, the sensing device must operate at the working wavelength (λ=1.3 μm). On the other hand, the achieved resolution in position and radiation power measurements is directly related with the obtained noise level at the sensing system outputs, as discussed further on.

2.7.2 Sensing Device and Adaptation Stage

The selected FQP is a Germanium J16QUAD-8D6-R05M from Judson Technologies (5 mm diameter, squared and with a 37 μm gap distance). This device has a wavelength spectral response comprised in the 0.8-1.8 μm range and works at ambient temperature without reverse biasing (photovoltaic mode). This sensing device has been selected rather than continuum PSDs or CCD cameras, since it shows higher spatial resolution than the former and higher time resolution than the latter. The selected FQP must work at an incident radiation power of 2 mW, since its response is saturated around 3 mW and the noise level is also reduced. The FQP preamplifier is a four channel Judson preamplifier (model n^0 490181) which allows pre-amplifying each photodiode signal independently.

Preamplifier Nominal Bandwidth [MHz]	1.4
Output Offset Voltage$\|_{max}$ [mV]	±4.5
Input Bias Current [μA]	1.2
Input Noise Voltage @ 1KHz [nV/√Hz]	6
Output Impedance [Ω]	50
Maximum Output Current [mA]	25
Maximum Output Voltage [V]	±2.5
Transimpedance Gain Z_m [Ω]	134
Germanium Responsivity Re @ 1300 nm [A/mW]	600×10^{-6}

Table 2.3. *The main performances of the four channel preamplifier and FQP.*

Table 2.3 summarizes the main electrical characteristics of the selected preamplifier and FQP. From these data, some interesting restrictions over the post-processing stage can be extracted, since the FQP and preamplifier impose the electrical constrains to the whole system [52]. Firstly, the bandwidth has to be higher than 1.4 MHz once the gain response versus frequency has decreased 0.1dB ($BW_{@-0.1}$

$_{dB}$), in order to keep the nominal bandwidth of the preamplifier. Secondly, the output offset voltage of the preamplifier must be corrected using a trim circuit (compensation stage) in the post-processing signal circuit. Thirdly, the post-processing circuit input impedance must be 50 Ω.

2.7.3 Position and Power Measurement Principle

For the chosen sensing device, $V_{out,x}$, $V_{out,y}$, and $V_{out,P}$ may be electronically obtained according to the next generic equations [52, 53]:

$$V_{out,y} = A_{v0,2} \frac{(V_{Q1} + V_{Q2}) - (V_{Q3} + V_{Q4})}{V_{Q1} + V_{Q2} + V_{Q3} + V_{Q4}} \quad (2.7.1)$$

$$V_{out,x} = A_{v0,2} \frac{(V_{Q1} + V_{Q3}) - (V_{Q2} + V_{Q4})}{V_{Q1} + V_{Q2} + V_{Q3} + V_{Q4}} \quad (2.7.2)$$

$$V_{out,P} = A_{v0,1}(V_{Q1} + V_{Q2} + V_{Q3} + V_{Q4}) \quad (2.7.3)$$

where $A_{v0,1}$ and $A_{v0,2}$ are generic gains; and V_{Q1}, V_{Q2}, V_{Q3}, V_{Q4} correspond to the post-processing circuit input voltages. From $V_{out,y}$ and $V_{out,x}$, the laser spot position from the FQP centre can be deduced from the following equations [52, 53]:

$$y = \frac{(\phi - g)}{2} \frac{V_{out,y}}{\kappa'} \quad (2.7.4)$$

$$x = \frac{(\phi - g)}{2} \frac{V_{out,x}}{\kappa'} \quad (2.7.5)$$

where ϕ [µm] is the IR-laser spot diameter on the FQP, g [µm] denotes the separation gap between photodiodes and κ' [V] is the sensitivity which takes into account the response of the whole sensing system, relating the beam diameter displacement to the output voltage. From $V_{out,P}$ signal, the incident radiation power (P) can be evaluated by using the following equation:

$$P = \frac{1}{Z_m \operatorname{Re} A_{v0,1}} V_{out,p} \tag{2.7.6}$$

where Z_m [Ω] is the transimpedance gain associated to each preamplifier channel and Re [A/mW] is the responsivity of the four quadrant detector, which relates the incident radiation power to the photo-generated current.

2.7.4 Post-Processing Signal Circuit Design

2.7.4.1 Block Diagram of the Post-Processing Signal Circuit

According to equations (2.7.1), (2.7.2), and (2.7.3), the block diagram for the post-processing circuit can be functionally designed as shown in Figure 2.7.2. It is analogically implemented using operational amplifier (op amp) based adders (first stage) and analogue divisors (second stage).

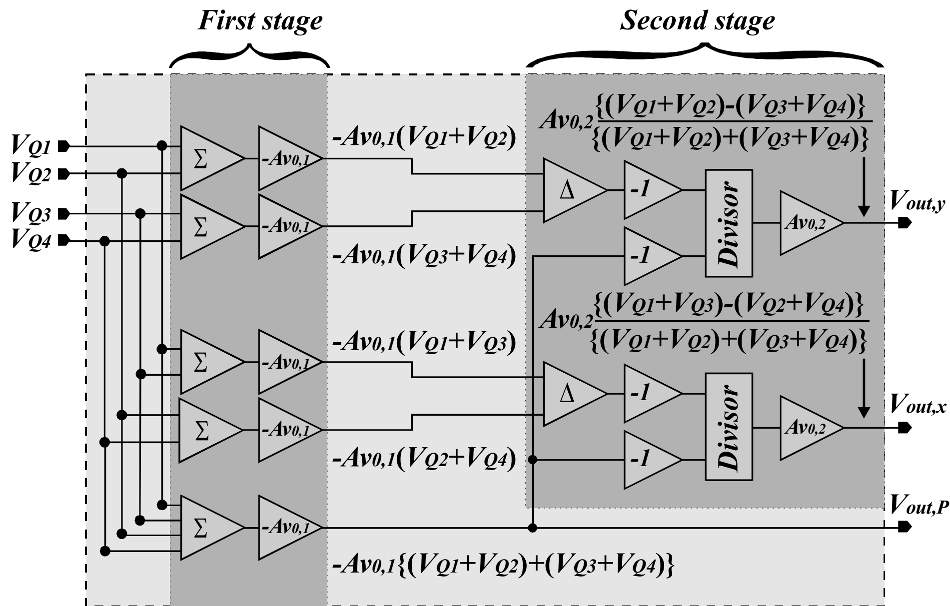

Figure 2.7.2. *Block diagram corresponding to the post-processing circuit.*

2.7.4.2 First Stage Design

Op amp based adders can be implemented by means of two different topologies (non-inverting and inverting) as observed in Figure 2.7.3 (a) and (b). The output voltage equations for the non-inverting ($V_{out,non}$) and inverting ($V_{out,inv}$) in terms of the kth-adder input resistors ($R_{in,k}$) and voltages ($V_{in,k}$) are expressed as follows:

$$V_{out,non} = \left(1 + R_F / R\right) \sum_{k=1}^{N} \frac{R_{in,k} R_S}{R_{in,k} + R_S} V_{in,k} \tag{2.7.7}$$

$$V_{out,inv} = -R_F \sum_{k=1}^{N} \frac{V_{in,k}}{R_{in,k}} \tag{2.7.8}$$

where R_F corresponds to the op amp feedback resistor for each configuration, and R_S denotes the resistance of non-inverting op amp input. From equations (2.7.7) and (2.7.8), it can be inferred that the amplifier gain is adjusted with a higher accuracy and precision using the inverting topology. Subsequently, the latter has been chosen in this work.

The main problem involved in this stage is the offset voltage. This voltage (input offset voltage) is introduced by the previous block and generated in the present stage. Regarding its electronic origin, the problem can be solved designing an external trim circuit or correcting the op amp non-idealities. Moreover, the suppression of this undesired effect must be tackled in the design of this stage, since the offset compensation cannot be easily performed at the second stage output due to its nonlinear operation. Figure 2.7.4 shows a simplified schematic of the trim circuit used for removing the input offset voltage coming from the FQP preamplifier [54]. In this circuit, two precision voltage references (V_{REF}), one positive and the other one negative, are connected to a variable resistor (R_{CQJ}) which acts as a voltage divisor. The main characteristics of V_{REF} must be a low noise generation, low thermal drift, and adjustable voltage value. At the output of this simple circuit, the compensation voltage V_{CQJ} is maintained constant by means of C_{CQJ}. In this notation, the J subscript denotes the FQP quadrant number. The trim circuit output is connected to one of the adder inputs, applying a final gain which diminishes V_{CQJ}. Thus, its maximum compensation range, at least ± 4.5 mV according to Table 2.3, depends on the V_{REF} value and the adder configuration gain (input adder resistance $R_{in,k}$, exactly). Eventually, the input offset voltage is compensated by tuning the variable resistor.

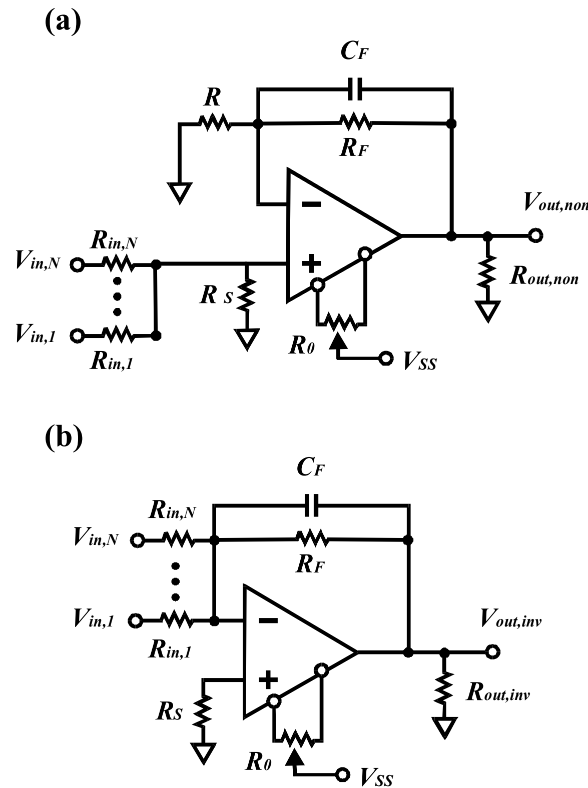

Figure 2.7.3. *N-input op amp based voltage adders with offset compensation:* (*a*) *Non-inverting configuration,* (*b*) *Inverting configuration.*

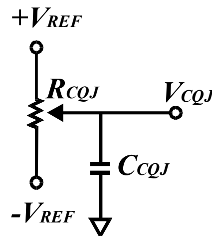

Figure 2.7.4. *Proposed schematic to remove input voltage offset for each signal channel.*

The output offset voltage originated from op amp non-idealities may be compensated with a correct op amp selection. Basically, these non-idealities correspond to internal op amp differential-pair mismatching, operational biasing current and thermal drift effects. The first contribution to output voltage offset is avoided with an internal compensation mechanism. The second one can be cancelled by means of a suitable selection of the resistor R_S that, for the chosen adder configuration, must verify the following expression [54]:

$$R_S = \left(R_F^{-1} + \sum_{j=1}^{N} R_{in,k}^{-1} \right)^{-1} \tag{2.7.9}$$

Depending on the selected op amp, thermal drift effects can be also neglected. In conclusion, the selected op amp must show: internal mechanism for voltage offset compensation, low thermal drift, low noise level, and high bandwidth (higher than 1.4 MHz).

2.7.5 Circuit Implementation

In the first stage, the analogue adders have been implemented using AD797 op amps [55], satisfying all the above stated conditions: $BW_{@-0.1\ dB}$ = 2.4 MHz, V_{Noise} = 1.8 nV/√Hz, internal offset adjustment and low thermal drift (1 µV/ºC). The desired gain has been configured using high precision resistors (0.1% tolerance), thus assuring a good accuracy in its implementation. In order to cancel the input offset voltage, additional adder inputs are used as explained above. All the values of the components shown in Figure 2.7.3 (a) are summarized in Figure 2.7.5. For this stage, an amplification value ($A_{v0,1}$) of 10 has been selected, as explained further on. Figure 2.7.6 shows the implemented circuit for compensating the input offset voltage. In this circuit, ±5 V AD586 [56] have been chosen as voltage references of high precision. This voltage reference is adjusted by means of the variable resistors R_{T+} and R_{T-}. Moreover, the AD586 introduce low noise to the established voltage reference, which can be minimised connecting a 1 µF capacitor between the noise reduction pin (*NR*) and the ground pin (*Gnd*) of the selected voltage reference. As a consequence, only 160 $\mu V_{p\text{-}p}$ voltage noise level is achieved. For this design, it is possible to remove input offset voltages in the range of ±5 mV tuning the variable resistors R_{CQ1}, R_{CQ2}, R_{CQ3}, and R_{CQ4}.

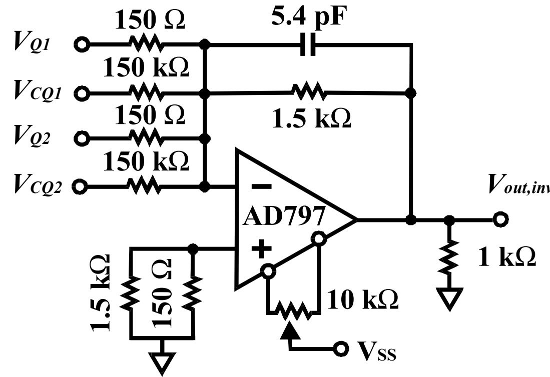

Figure 2.7.5. *Implemented adder with two input signals and the corresponding nulling offset voltages.*

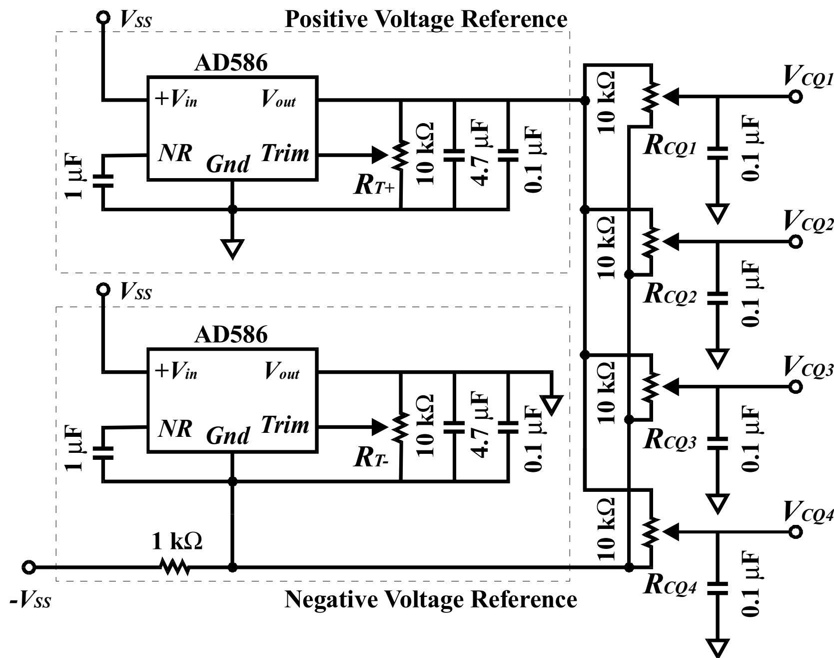

Figure 2.7.6. *Circuit schematic showing the stage for compensating the input offset voltage.*

For the second stage, two four quadrants multipliers AD734 and two dual op amp AD512 [57] have been selected, as shown in Figure 2.7.7 (a). The first IC implements the dividend sum and also performs the whole division. With the AD512, a tuneable gain (thanks to the 100 KΩ variable resistors) is introduced, as well as a low current level between the two inputs of the AD734 is kept. As Figure 2.7.7 (b) shows, the AD734 bandwidth depends on the denominator value. In order to achieve a bandwidth higher than 1.4 MHz, 1V denominator working value and 20 dB

voltage gain are required ($A_{v0,2} = 10$), as observed in the curve II of Figure 2.7.7 (b). Hence, for the nominal working radiation power (2 mW), the mentioned denominator condition can also be satisfied for a first stage gain of 20 dB ($A_{v0,1}$=10).

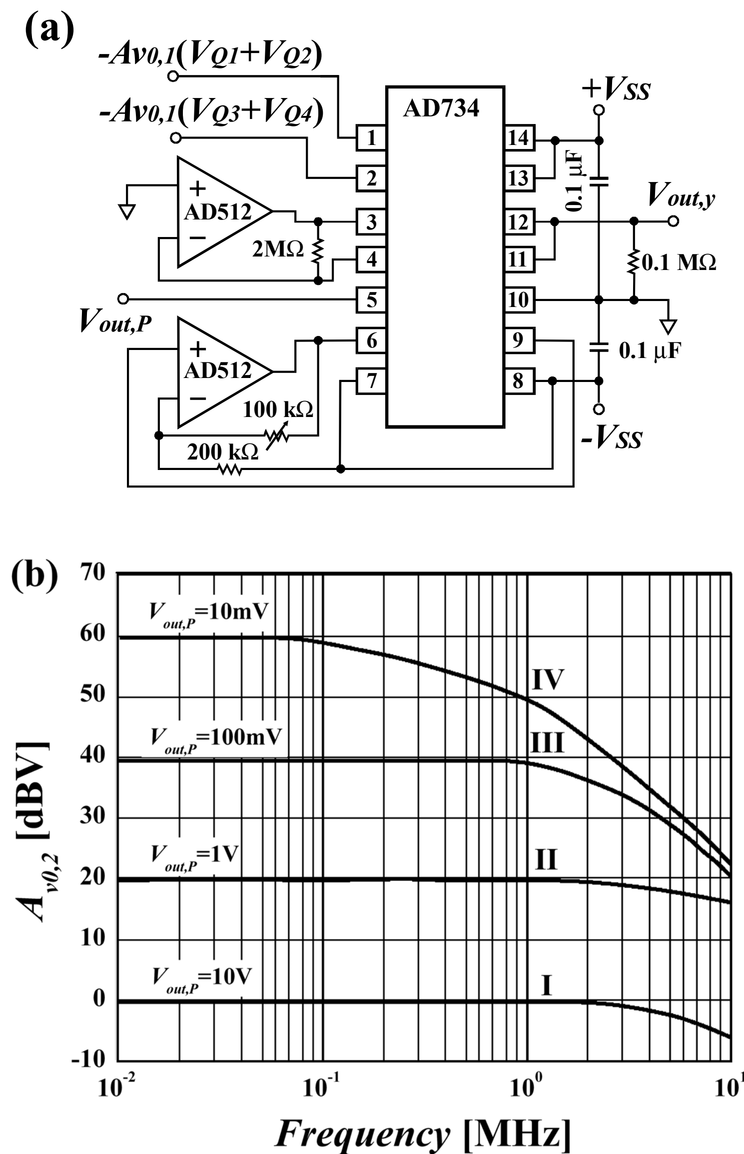

Figure 2.7.7. (*a*) *Schematic of the designed divisor to calculate* $V_{out,y}$. (*b*) *Nominal frequency response of the divisor gain depending on denominator value* $V_{out,P}$.

This circuit has been developed in a standard PCB-board, employing low noise techniques such as ground planes to shield the signal channels, design considerations for the maximum layout symmetry, and peripheral distribution of the supply lines.

Furthermore, EMI reduction techniques have also been followed. All elements have been supplied at 15 V supply (V_{SS}). To take full advantage of the wide bandwidth and dynamic range capabilities required in this application, multiple bypassing have been performed by means of tantalum and ceramic capacitors connected in parallel. For the input supply bus, 4.7 µF tantalum and 0.1 µF ceramic capacitors are used, while, for each IC, 0.1 µF tantalum and 0.1 µF ceramic capacitors are employed.

2.7.6 Performances and Features of the Post-Processing signal Circuit

From the obtained performances point of view, in the case of the deflection signals ($V_{out,x}$ and $V_{out,y}$), a 2 MHz $BW_{@-0.1\ dB}$ and a 14 mVrms noise level for the working radiation power (2 mW) has been achieved. Concerning $V_{out,P}$, a 2.4 MHz $BW_{@-0.1\ dB}$ and a 3.5 mVrms noise level have also been measured. On the other hand, κ' has also been extracted from Figure 2.7.8 (a). Figure 2.7.8 (a) shows the experimental static characterisation of the system response, where $V_{out,y}$ signal versus the relative displacement normalized to the spot radius (W) is plotted. The obtained slope in the linear response region is $\kappa' = 10.13$ V. The relationship between P and $V_{out,P}$ has been experimentally determined, as shown in Figure 2.7.8 (b). Notice that in Figure 2.7.8 (b) the absolute value of $V_{out,P}$ is plotted. From the linear fit, the obtained proportionality factor (806×10^{-3} V/mW) agrees with the theoretical value calculated from equation (2.7.6), corresponding to 804×10^{-3} V/mW.

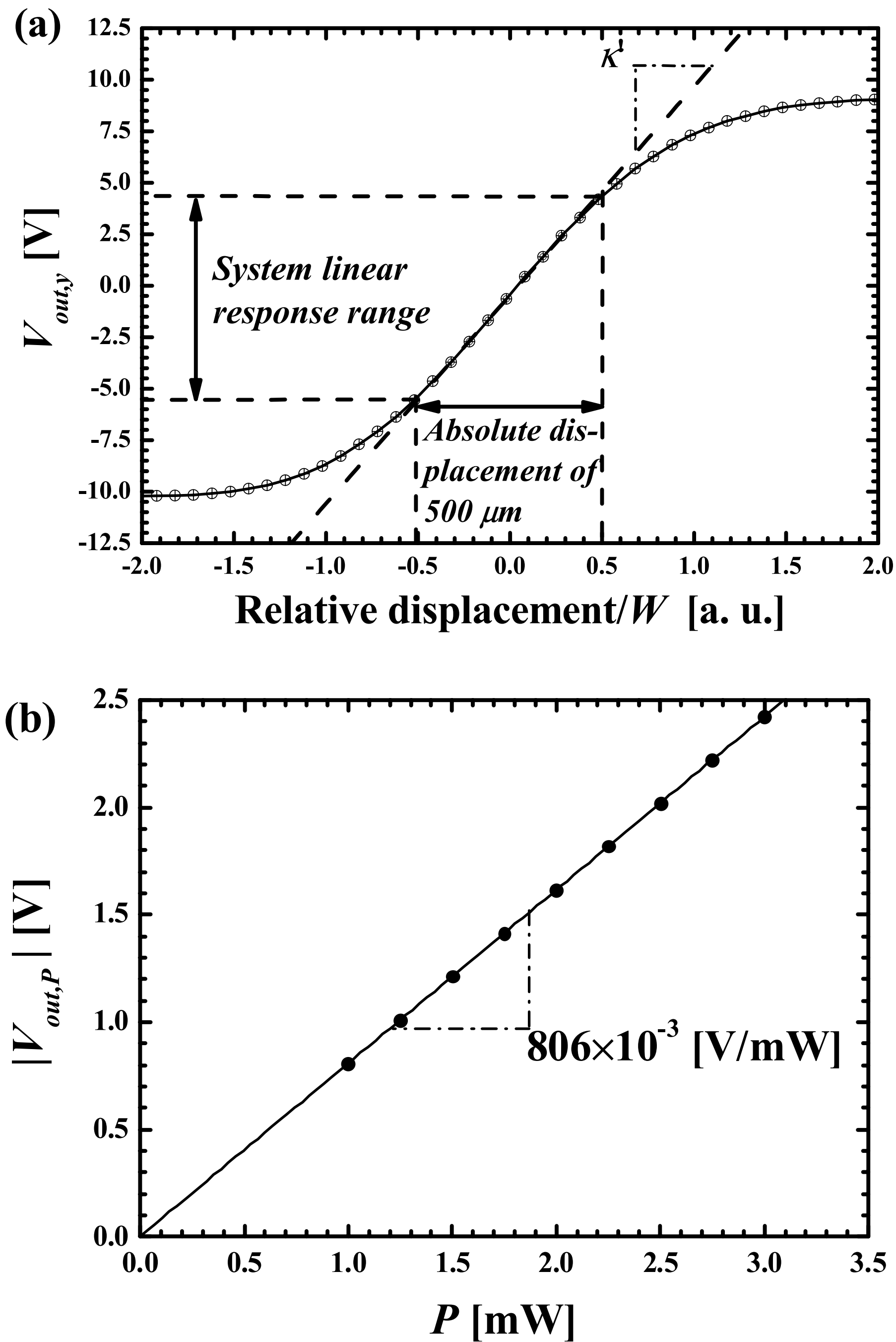

Figure 2.7.8. (*a*) *Experimental characterisation of the static system response, corresponding to* $V_{out,y}$ *vs spot relative displacement.* (*b*) *Experimental determination of the proportionality factor which relates P with* $V_{out,P}$.

2.7.7 Experimental Analysis of the Sensing System Noise

In the FQP, two current noise sources can be identified. They are physically originated by random fluctuations in the number of charge carriers during its motion (shot noise) and their thermal agitation (Johnson or thermal noise). The contributions to shot noise are the current flowing in a reverse biased FQP when there is no incident radiation (leakage current or dark current), and the photo-generated current I_J [58]. Although the dominating noise source usually is Johnson noise in an unbiased FQP, the I_J component of the shot noise takes a higher contribution due to the high power radiation value (2 mW) used in this work. The preamplifier input noise sources are, aside from FQP shot noise, the Johnson noise related with the used resistors and the one resulting from op amp operation, i. e., an input noise current and an input noise voltage [58]. It has been experimentally determined which of both, FQP or preamplifier, has the major contribution to the total voltage noise at the preamplifier output. The test consists in changing, from 0 to 2 mW, the incident radiation power on the FQP to check the induced variations on the voltage noise. As a result, the voltage noise has been unchanged. This fact implies that the preamplifier noise sources fix the output voltage noise. For the working power radiation value, a 45.26 dB signal-to-noise ratio (SNR) is measured.

For the post-processing circuit case, the contribution to the noise level at the first stage output is related to the resistors (Johnson noise) and the used op amp (AD797). The SNR at its first stage output is also measured for a 2 mW laser spot centred on the FQP. In this case, a 51.13 dB SNR is measured at the output of the two input adders (involved in $V_{out,y}$ and $V_{out,x}$ determination), whereas, a 54.71 dB is obtained at the output of the four input adder ($V_{out,P}$ output). Both values are higher than the one measured at the preamplifier output due to the performed operation in each adder. Notice that, in this stage, the noise level introduced into the signal noise is not so important as to degrade drastically the SNR. At the second stage, the signal noise is mainly produced by the AD734. The description of AD734 noise sources is not as simple as in the other cases, since this IC performs a non-linear operation. Its main limiting features are its static error and its total output noise density. The first one

provides the AD734 accuracy when it performs the operations shown in Figure 2.7.1. This limitation is due to the combination of scaling voltage (denominator voltage variations), internal offsets, and non-linear effects during AD734 operation. This IC establishes the total signal noise at the post-processing circuit output (14 mVrms, as previously stated).

2.7.8 Achieved Resolution in Spot Displacement and Power Sensing

The PSD theoretical resolution in spot displacement determination ($\sigma_{position}$) is provided by SNR of each preamplifier output, according to the following equation [59]:

$$\sigma_{position} = \frac{\pi}{16}\frac{\phi}{SNR} \tag{2.7.10}$$

This expression is inferred for a uniform circular spot ϕ, being valid for short spot displacements around the PSD centre. For $P = 2$ mW and ϕ=1 mm, a 45.26 dB SNR is measured at each preamplifier output which provides a theoretical resolution of 1.07 μm. Nevertheless, the achieved resolution in spot displacement sensing with the developed system cannot be evaluated using equation (2.7.10). When the laser spot is located at the FQP centre, both deflection signals and their corresponding SNR values are null giving an infinite $\sigma_{position}$. Subsequently, an alternative expression for calculating the obtained resolution from the achieved uncertainty in the spot displacement sensing (Δy and Δx) is proposed. Δy and Δx may be derived from (2.7.4) and (2.7.5) assuming that the main measurement error is the electronic noise in both post-processing circuit outputs, as expressed in the following equations:

$$\Delta y = \sqrt{2}\,\frac{(\phi - g)}{2}\frac{V_{noise,y}}{\kappa'} \tag{2.7.11}$$

$$\Delta x = \sqrt{2}\,\frac{(\phi - g)}{2}\frac{V_{noise,x}}{\kappa'} \tag{2.7.12}$$

where $V_{noise,y}$ and $V_{noise,x}$ represent the measured rms noise values at both deflection outputs $V_{out,y}$ and $V_{out,x}$, respectively. Once the spot is centred at the FQP, the resolution would be twice the uncertainty value (i. e., $\sigma_y=2\times\Delta y$ and $\sigma_x=2\times\Delta x$), because this establishes the upper and lower limits where different beam deflections may be distinguished between them. In the present work (ϕ=1 mm and g=37 µm), a ±0.94 µm uncertainty and 1.88 µm resolution in spot displacement sensing are obtained. Concerning the uncertainty and resolution in power sensing (ΔP, σ_{Pw}), an expression may be derived from (2.7.6), following the same steps as in the previous case, i. e.:

$$\Delta P = \sqrt{2}\,\frac{1}{Z_m \operatorname{Re} A_{v0,1}} V_{noise,P} \qquad (2.7.13)$$

$$\sigma_{Pw}=2\times\Delta P \qquad (2.7.14)$$

giving in the present work (2 mW working power) ΔP= ±6.13 µW and σ_{Pw}=12.3 µW.

2.8 Electrical Set-up II: DUT Excitation System

2.8.1 General Description

For biasing the DUT with short current pulses, a modified buck converter, based on a modular characterisation system developed for power devices [60], has been implemented. As depicted in Figure 2.8.1, the electrical excitation system can be divided in three functional sub-circuits: the Buck converter, gate-drive circuit, and synchronisation and control unit (SCU). The Buck converter is formed by the passive components, power devices, and protection diodes shown in Figure 2.8.1. The gate-drive circuit, or driver, controls the state of MOS-gated power devices, i. e., conduction or blocking, immediately providing or subtracting the required current for charging or discharging its input gate capacitance. In this system, two drivers are required, as explained further on. The SCU, externally controlled by a control signal $V_{generator}$, manages the activation or deactivation of both drivers, as well as their

synchronisation. As for external elements required for the system operation, they carried out tasks of power supplying, external control and current measurement. A voltage source manufactured by Metrix (0-60 V) is used as a power supply of the Buck converter (V_S), whereas the drivers and SCU are supplied by floating voltage sources (0-24 V). $V_{generator}$ is provided by a waveform generator (HP33120A). The current is measured with an active current probe (Tektronix A6312), together with its preamplifier (Tektronix preamplifier AM 503B), allowing acquisition of current level by means of a digital oscilloscope (TEK 744A). Regarding the general operation of the DUT excitation system, the generation of the current pulse starts when SCU detects a rising edge in $V_{generator}$. After that, SCU selects and activates the corresponding driver to turn-on the MOS-gated switch. At that moment, a current I_C flows through the converter. When the falling edge of $V_{generator}$ is detected by SCU, the driver is deactivated, turning off the power device. Thus, the conduction time is established by the duration of $V_{generator}$ pulse, whilst the reached current level is adjusted by V_S value.

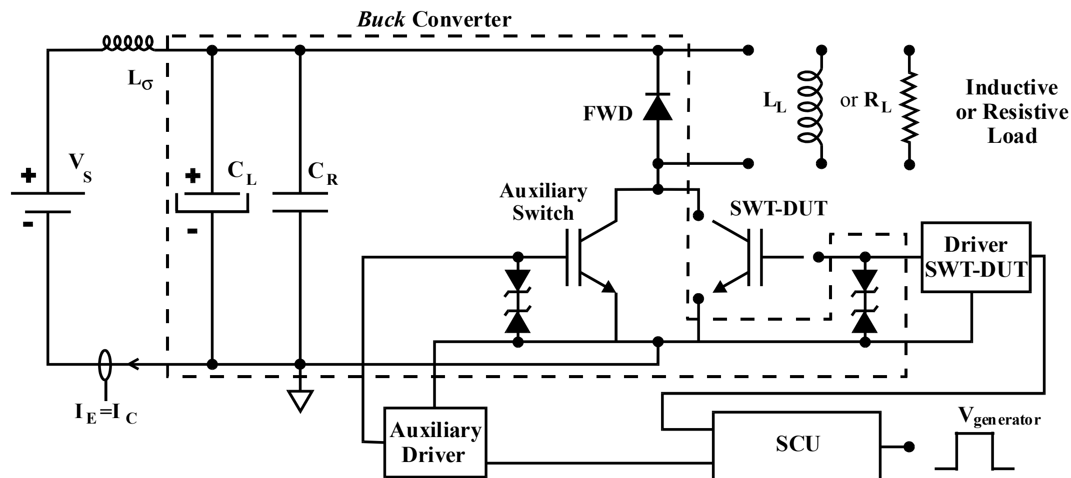

Figure 2.8.1. *Schematic of the excitation System for DUT biasing under real operating conditions.*

2.8.2 Buck Converter

In more detail, the Buck converter consists of the decoupling capacitors, load, DUT, auxiliary switch, free-wheel diode (FWD) and Zener diodes, all together shown in Figure 2.8.1. The capacitors rapidly provide the current level required by the switch

turn-on, since the voltage source has limited its current rise time due to the stray inductance L_σ. Basically, V_S charges the capacitors and they provide the current pulse. In this circuit, fast and slow capacitors can be distinguished. The fast capacitors (C_R), located very close to the commutated switches, provide the initial current during the commutation process. In contrast, the slow electrolytic capacitors (C_L) maintain approximately constant the V_S value and supply the high currents required in the commutation process. The auxiliary switch, connected in parallel with the DUT, minimises the DUT self-heating during single-shoot inductive load tests and generates the current pulses that will bias other DUTs, such as power diodes. The role of the FWD obeys protection purposes. When an inductive load is connected to the converter and the switch is in blocking state, the free-wheel diode establishes an alternative way for discharging the stored magnetic flux, avoiding undesired over-voltage peaks at the inductor terminals. The Zener diodes protect the switch gate, limiting the transient overvoltages.

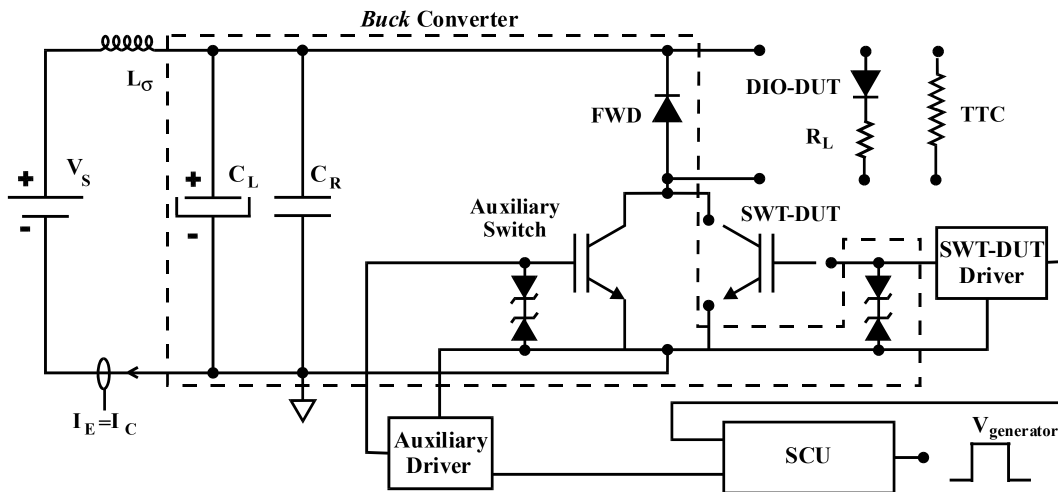

Figure 2.8.2. *Schematic for the connectivity of other kind of devices, such as diodes or thermal test chips.*

The connection of the different types of DUTs to the excitation system is illustrated in Figure 2.8.2. Inspected MOS-gated switches (SWT-DUT) are connected as the main switch in the buck converter, whereas power diodes (DIO-DUT) or the thermal test chip (TTC, denoted by a resistor), used for the equipment

thermal calibration and shown in the next chapter, are connected in parallel with FWD.

2.8.3 Gate-Drive Circuit

As previously mentioned, the gate-drive circuit controls the gate-to-emitter voltage of all MOS-gated switches (DUT or auxiliary). Its basic scheme is shown in Figure 2.8.3. The main point concerning this driver is that four floating voltage power supplies have been used, simultaneously allowing the correct optocoupler biasing at the input stage (V_{O1} and V_{O2}) and variable output voltages applied between the gate and emitter terminals of the DUT (V_{Gon} and V_{Goff}). In addition, the included jumpers J_1 and J_2 allow this driver operating with only two floating voltage power supplies, if for the test conditions V_{O1}=V_{Gon} and V_{O2}=V_{Goff}.

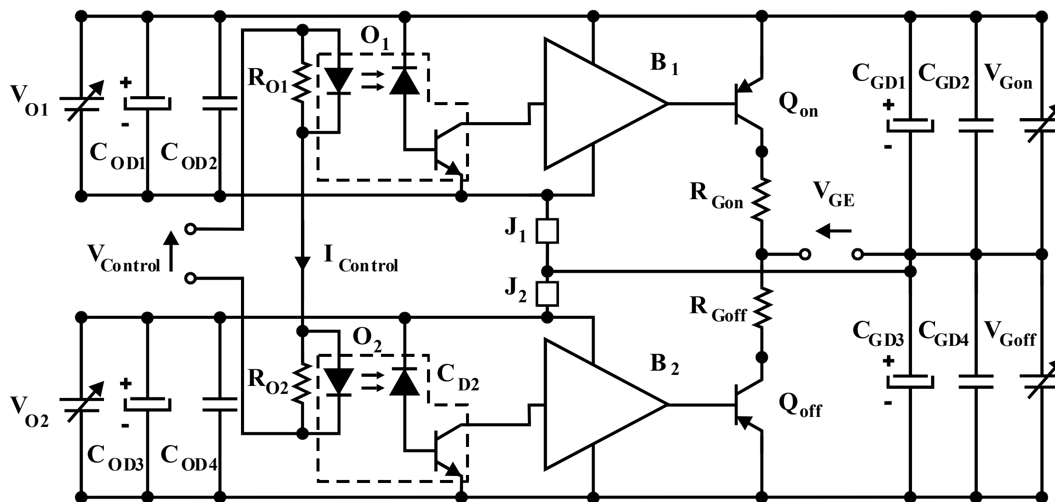

Figure 2.8.3. *Simplified scheme of the gate-drive circuit.*

All capacitors illustrated in Figure 2.8.3 are used for bypass purposes. The driver input is controlled by the signal $V_{Control}$ which will oppositely activate the optocouplers O_1 and O_2 with the current $I_{Control}$. At O_1 and O_2 outputs, the current buffers B1 and B2 amplify the incoming current to turn-on or turn-off the transistors at the output stage. The driver output stage is implemented by bipolar transistors (Q_{on} and Q_{off}), showing fast switching times. On- and Off-gate resistors (R_{Gon} and R_{Goff}) can also be fixed independently.

2.8.4 Synchronisation and Control Unit

As previously explained, SCU is triggered by $V_{generator}$ edges. From this signal, three inverted pulses are generated to activate and synchronise the DUT with the auxiliary switch, as depicted in Figure 2.8.4. For this purpose, four monostables M (CD4098B) are used, as demonstrated in Figure 2.8.5. Each monostable is configured with a variable resistor, allowing adjustment of the time parameters also shown in Figure 2.8.4. t_1 and t_2 (t_3 and t_4) represent the delay time respect to the $V_{Control,SWT\text{-}DUT/AUX}$ rise (fall) edge and the pulse duration at $V_{Control,Switch}$ ($V_{Control,SWT\text{-}DUT}$), obtained from the monostables M_1 and M_2 (M_3 and M_4) by tuning the resistors R_5 and R_7 (R_{11} and R_{14}), respectively. The SCU output stage is implemented with bipolar transistors (Q_1, Q_2, Q_3), which invert $V_{generator}$ and the output waveform from monostables, assuring a high rise time for each control signal. Depending on the used load or analysed DUT, the appropriate SCU output must be connected to the corresponding driver input. $V_{Control,Switch}$ is connected to the DUT driver only when a MOS-gated switch under resistive load conditions is measured. When this switch is measured under inductive conditions, $V_{Control,SWT\text{-}DUT/AUX}$ and $V_{Control,SWT\text{-}DUT}$ are connected to the auxiliary switch driver and the DUT driver, respectively. Finally, when measuring diodes, $V_{Control,SWT\text{-}DUT}$ is connected to the auxiliary switch driver.

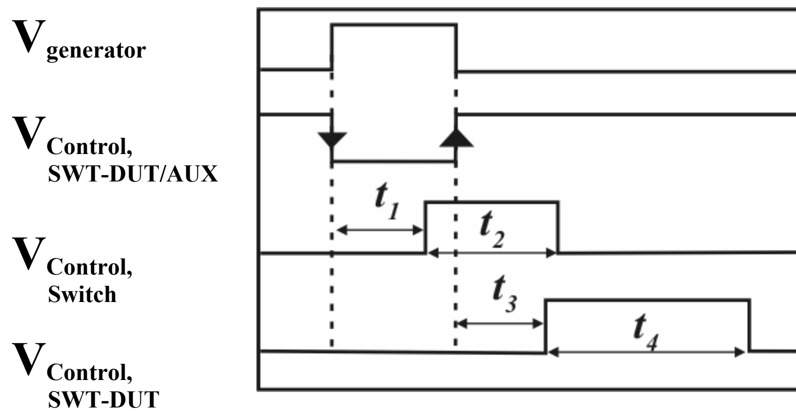

Figure 2.8.4. *Cronogram of $V_{generator}$ and the three pulses generated by the SCU.*

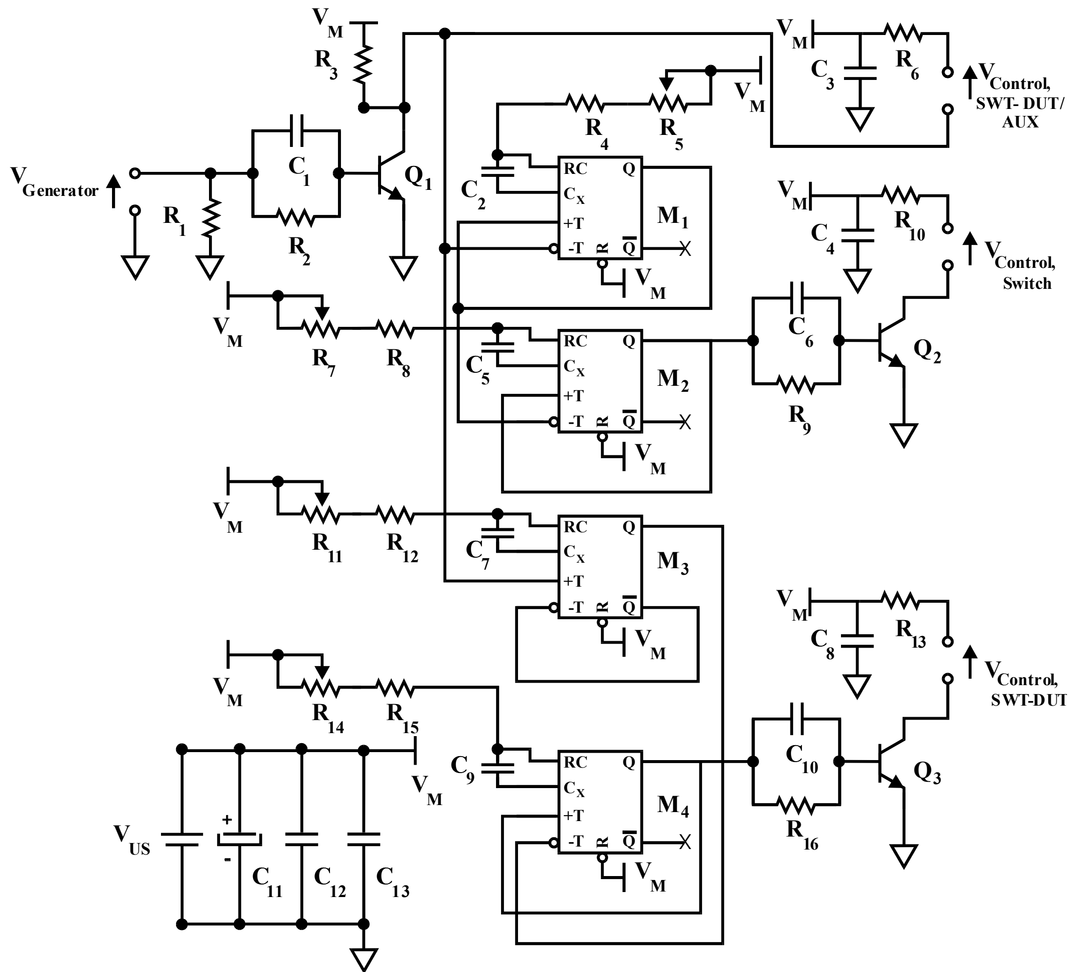

Figure 2.8.5. *Schematic of the SCU, showing the monostables and tuning resistors configuration.*

2.9 Conclusions

In this chapter, the design and development process of an experimental rig based on the Internal IR-Laser Deflection (IIR-LD) technique is described. This technique shows a high versatility, since it allows measuring temperature gradients and free carrier concentration inside power devices. The IIR-LD physical principles are based on the plasma-optical and thermo-optical effects produced in a biased DUT, inducing the deflection and radiation absorption on a probe laser beam. Both effects are linearly related with the refractive index and absorption coefficient, as further discussed in this chapter. Thus, the first step towards any measurement is the determination of these proportionality factors. For this reason, a research in the

literature resources has been performed for the experimental conditions of this work ($\lambda = 1.3\mu m$). Moreover, the set of equations relating the measured signals with temperature gradients and free carrier concentration are also shown, and completely derived in Appendix A.

The developed experimental rig is divided in three main set-ups: optical, mechanical, and electrical. The optical set-up is formed by an IR-laser source and an optical system (two lenses and a beam collimator). By means of the optical system, the beam diameter across the DUT and onto the FQP surface is controlled. This fact is an important issue, because the spatial resolution depends on the beam spot dimensions. The beam shape along the interaction with the DUT has been optimised for typical DUT lengths (5-10 mm). The obtained beam shape has been measured using a thin metallic plate, and, afterwards, it has been compared with a simple model prediction, obtaining a very good qualitative agreement. From this experimental result, a $(19.89 \pm 0.49) \times 10^{-3}$ beam numerical aperture and 20±7 µm minimum beam diameter are determined. For typical lateral dimensions of power devices (within 5-10 mm), the beam diameter on DUT lateral sides varies within 35-57 µm. In these conditions, the achieved spatial resolution goes from 22 µm to 32 µm, yielding a spatial error range from 11 µm to 16 µm. Concerning the spot dimensions on the sensing device surface, a 1 mm beam diameter is experimentally measured.

The mechanical set-up is constituted by six displacement modules. When the optical centring or measurements on DUT are performed, they assure the displacement for the collimator, each lens, DUT, and sensor. Each displacement module consists of different micro-positioning stages and adapting pieces, which assure a ±7 µm and ±5 µm uncertainties in DUT incremental displacement and optical centring, respectively. Notice that the spatial error introduced by the probe beam and the uncertainty given by micro-positioning stages in DUT displacement is very similar. All the displacement modules are supported on an optical breadboard to isolate the experimental rig from environmental mechanical vibrations.

The electrical set-up consists of the power and deflection sensing system, the DUT excitation system, and the acquiring signal equipment. The power and deflection sensing system is formed by a four-quadrant photodiode sensor (FQP), I/V converter (FQP preamplifier), and post-processing signal circuit. Concretely, the post-processing signal circuit implements real-time arithmetical operations among the signals incoming from FQP. The power and deflection sensing system has been optimised to obtain a high resolution in radiation power measurements, position sensing, and time. Electronically, these requirements can be interpreted as a constraint on the noise level (deflection and radiation power resolution) and bandwidth (time resolution). For a 2 mW radiation working power, the noise level of deflection signals is 14 mVrms, while the radiation power one is 3.5 mVrms. This fact provides a spatial and radiation power resolution of 2 µm and 12 µW, respectively. Concerning the system bandwidth, a 1.4 MHz is obtained approximately providing a 350 ns time resolution. This fact is an important issue for resolving gradients of temperature and free-carriers concentration from the deflection signal, because they contribute to refractive index gradient following different time constants. Namely, a free-carrier concentration gradient is first established, and afterwards, a temperature gradient is produced inside the device, as shown in Chapter 5.

In order to bias the DUT with short current pulses, a modified Buck converter has been implemented. It can be divided in three functional sub-circuits: the Buck converter, MOS-gated drive circuit, and synchronisation and control unit (SCU). The Buck converter is the main sub-circuit where all passive components and power devices are connected. The MOS-gated drive circuit controls the state of MOS-gated power devices. The SCU manages the activation or deactivation of both drivers, as well as their synchronisation. All these actions are performed from an external control signal $V_{generator}$ provided by a waveform generator (HP33120A).Concerning the acquiring equipment, an A6312 Tektronix Hall Effect current probe (with a bandwidth of 100 MHz), along with its AM 503B Tektronix amplifier, and a TDS 744A four channel digitizing oscilloscope perform the measurement of the biasing current and all output signals of the sensing system, respectively.

Chapter 3

THERMAL CALIBRATION

3.1 Introduction

A procedure to calibrate the temperature measurements of the internal IR-laser deflection (IIR-LD) equipment is treated in this chapter. The presented method is based on the use of a thermal test chip whose behaviour is analytically well described by a simple analytical model thanks to the chosen structure and heating conditions. The model validity is justified by means of 3-D simulations using the FLOTHERM package. As a result of this process, it is possible determining the thermo-optical coefficient which relates the measured gradient of refractive index with the temperature gradient. This is an important issue since it allows obtaining more information on the right constants of the semiconductor involved in the temperature extraction.

3.2 Motivation

As shown in the previous chapter, the developed equipment requires the proportionality factors relating the material optical properties with T and C. Although this information may be found in the literature, the values of $(\partial n/\partial C)|_T$ therein reported show a high dispersion between them (22%), being very difficult its correct selection. This coefficient is very important in $\nabla_y T$ determination, as may be inferred from equation (2.3.5) when $\nabla_y C = 0$:

$$\nabla_y T = \frac{NA}{\kappa' L\left(\dfrac{L}{2 f_{L_2} n_0} + 1\right)\left(\dfrac{\partial n}{\partial T}\right)_C} V_{out,y} \tag{3.2.1}$$

where all the involved parameters can be measured with a higher accuracy than the dispersion shown by $(\partial n/\partial T)|_C$ in the literature. For this reason, a calibration method based on a thermal test chip (TTC) has been followed to select the suitable coefficient. This device was developed to test the thermal behaviour of different power substrates and packages [61], though it can be also used for internal temperature measurements, as it will be described further on. For the chosen experimental conditions, the TTC thermal behaviour is easily described by an analytical thermal model. Thus, the calibration procedure has consisted in estimating the temperature profile using IIR-LD measurements, and, then, comparing it with the predictions of the TTC analytical model.

3.3 The Thermal Test Chip

3.3.1 Structure Description

As Figure 3.3.1 shows, the TTC structure consists of a 525 μm Silicon substrate (low doped) with two stripe-shaped resistors of Poly-Silicon (heating resistor) and Platinum (sensing resistor) on its top surface. Two kinds of substrates have been used for the TTC manufacturing: N-type (1×10^{14} cm^{-3}) and P-type (1×10^{15} cm^{-3}). A detail of the TTC topside can be observed in Figure 3.3.2, where both stripe layouts are depicted. This stripe-shape topology of the resistors assures that the current density is uniformly distributed inside them, reaching a higher sensing accuracy as well as a uniform heating of the substrate topside. Both resistors are electrically isolated from the Silicon substrate by a very thin SiO_2 layer (38 nm), practically not affecting the heating and sensing processes. Concerning the heating resistor, its stripes are 20 μm wide and 5.52 mm long, separated between them 17 μm (see Figure 3.3.1 (a)), practically covering all substrate topside. They are connected in parallel, obtaining a 60 Ω resistance value. These dimensions lead to achieve a perfect vertical heat flow

from a given depth (30 µm, approximately), reaching a 1-D temperature profile along the TTC depth, as shown further on.

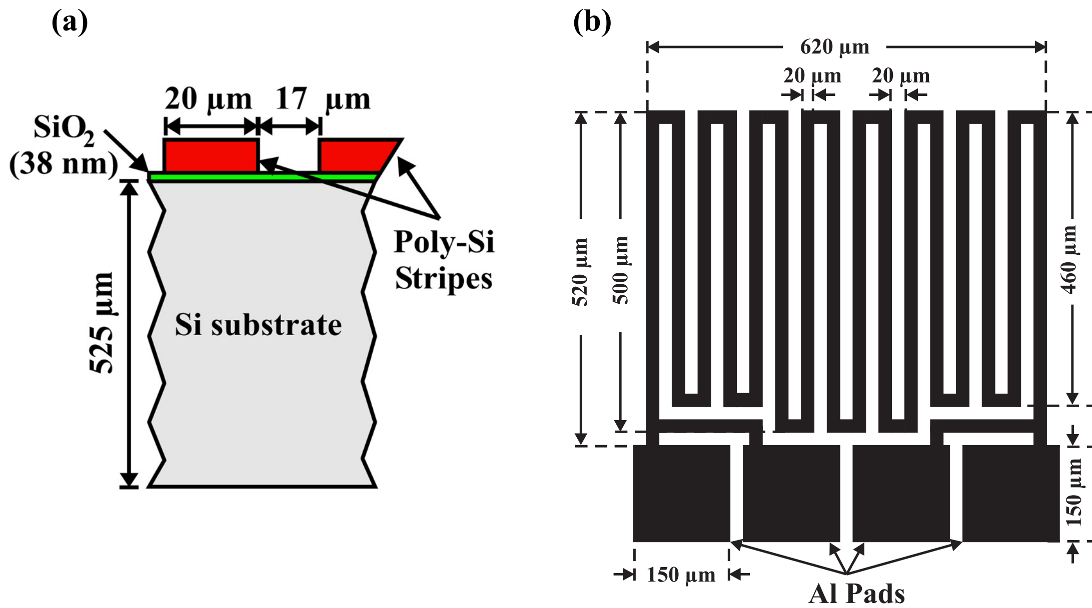

Figure 3.3.1. (*a*) *Schematic cross-sectional view of the TTC (not to scale), showing the substrate, the oxide layer, and the poly-Silicon dimensions.* (*b*) *Dimensions of the Pt sensing resistor.*

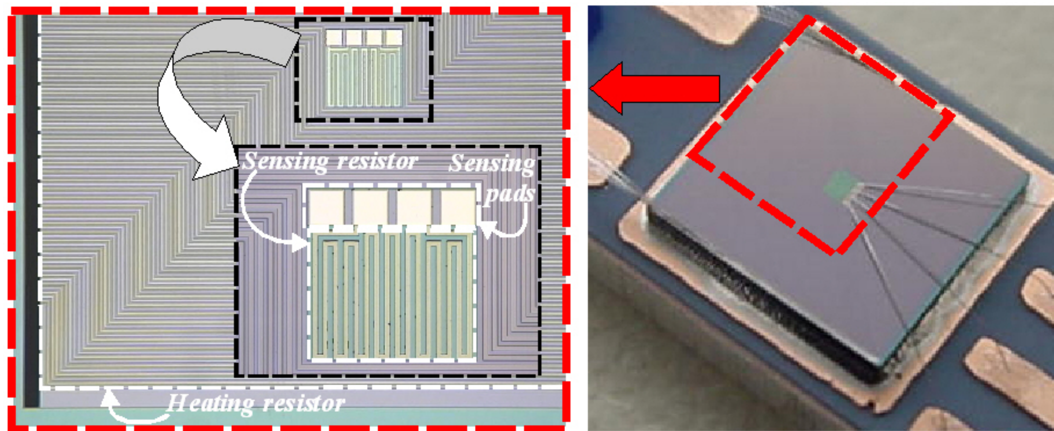

Figure 3.3.2. *Top view of a TTC part, showing both the heating and sensing resistors.*

On the other hand, the sensing resistor is a stripe packaged within a 500×620 µm^2 region in the TTC topside centre with four pads for measuring its resistance value by means of the four-wire method. The stripe dimensions are 20 µm wide and 7.98 mm long, providing a 600 Ω resistance value at room temperature (293 K). The pads are

squared occupying each one a 150×150 μm^2 area, as illustrated in Figure 3.3.1 (b). The sensor is integrated within a 717×717 μm^2 area, being in direct contact with the TTC top surface. In this configuration, the sensor cannot be used during the thermal calibration, since the TTC is heated during short times (<300 μs) not giving enough time to obtain an appreciable temperature rise below the sensor, as discussed further on. Indeed, the TTC was conceived and designed for power substrates and packages characterisation, where studied thermal phenomena are produced at higher time scales (millisecond range), in which a uniform temperature below the temperature sensor is perfectly established.

3.3.2 TTC Simulated Thermal Behaviour

3.3.2.1 Temperature Increase Profile

In order to demonstrate that the stripes distribution of the heating resistor allows obtaining a 1-D profile of temperature rise within the TTC, 3D simulations using FLOTHERM package [62] are performed. Figure 3.3.3 illustrates the 3D structure used for this purpose, corresponding to a part of the fabricated TTC. In this figure, it can be observed a substrate of 373 μm×600 μm lateral dimensions and 525 μm thickness, with 10 Poly-Silicon stripes (20 μm wide) on its topside, distanced between them 17 μm. The basic thermal behaviour of the full size (6×6 mm^2) TTC can be understood with such a simplified structure, avoiding excessive simulation times. The thin SiO_2 layer, placed between the Poly-Silicon and the Silicon substrate, has not been taken into account in the performed simulations, since its transient thermal effects do not affect the heat flow evolution at the time scale analysed in the present work. Regarding the simulation conditions, a constant power has been dissipated for each stripe, deriving its value from the heat flux density dissipated on the full size TTC top (45 mW for each stripe corresponding to 60 W for the whole TTC). The initial temperature condition is room temperature (293 K), and the boundary conditions are adiabatic on the top surface of the simulated structure and room isothermal on the bottom (293 K). The main simulation results are shown in Figures 3.3.4 and 3.3.5.

Figure 3.3.4 shows the temperature distribution along x axis for several depths, ranging y from 0 to 40 μm, at the time instant t=50 μs. As it can be observed, the temperature distribution along x is almost constant from y=30 μm. Subsequently, a 1-D temperature profile is achieved from a given depth inside the TTC. For this reason, all measurements will be performed from 70 μm depth, assuring that a 1-D profile of ΔT is well established.

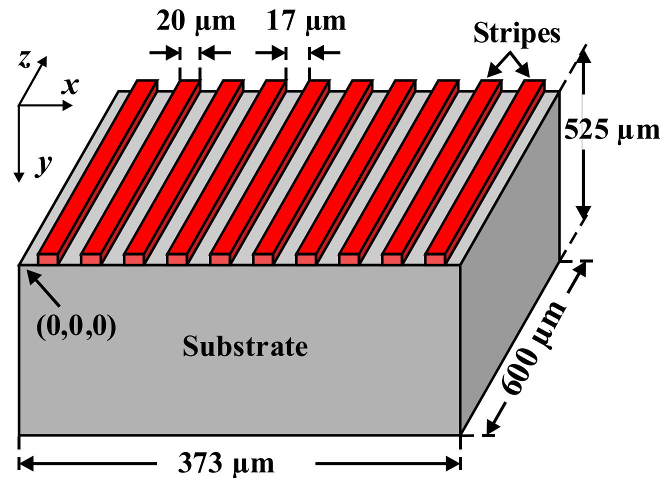

Figure 3.3.3. *Simulated 3D-structure, part of the full size TTC, showing its dimensions (not to scale).*

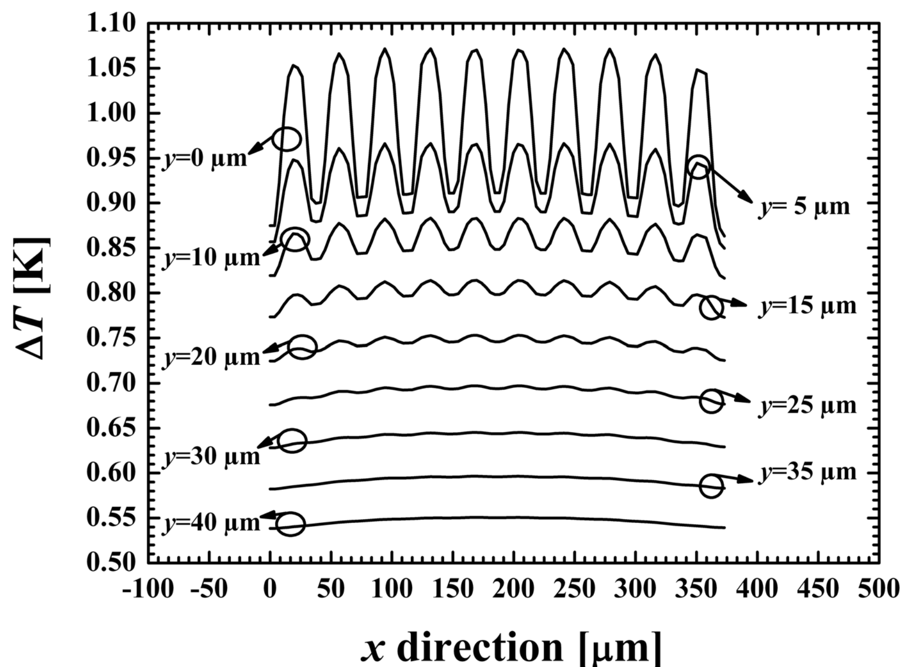

Figure 3.3.4. *Simulated temperature increase profile along x direction for several depths at t=50 μs for the structure of Figure 3.3.3.*

In Figure 3.3.5, the 2D cross-sectional view of the temperature distribution corresponding to the *x*-*y* plane located at *z*=300 μm is shown at the time instant t=250 μs. As a main noticeable fact, the isothermal line corresponding to T=293 K is 135 μm from the structure backside, indicating that the heat front has not reached it yet. Consequently, in this range of excitation times, the TTC can be thermally considered as a semi-infinite medium. Moreover, a significant temperature rise (below 2.5 K for *t*=250μs) is obtained for a 60 W equivalent power dissipated on the whole TTC top, also assuring that the involved thermal parameters, i. e., the thermal conductivity and diffusivity, remain constant.

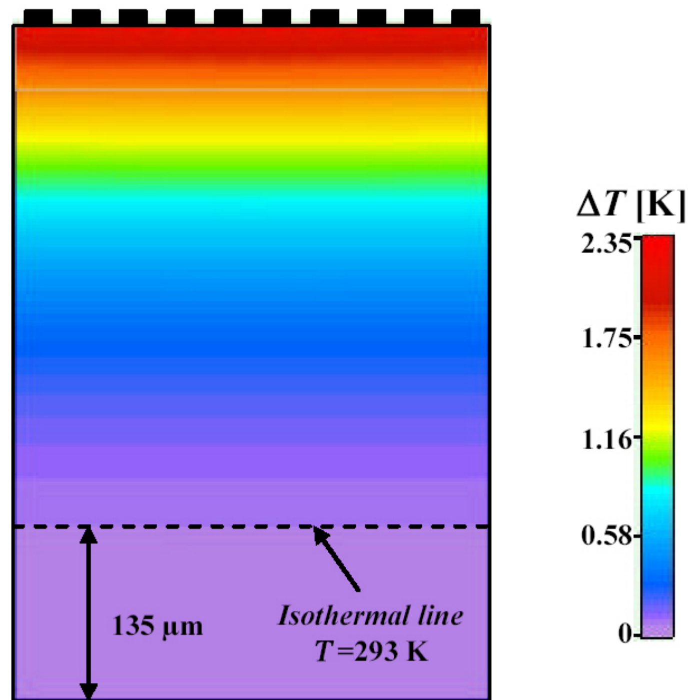

Figure 3.3.5. *2D cross-sectional view of the simulated temperature distribution at z=300 μm and t=250 μs, showing that the isothermal line T=293 K is located 135 μm from the structure backside.*

3.3.2.2 Suitability of the Sensing Resistor

3D simulations are also performed using FLOTHERM to analyse the suitability of the sensing resistor during the thermal calibration. Figure 3.3.6 depicts the used 3D structure for this purpose. In this figure, it can be observed a substrate of 6000×6000 μm^2 lateral dimensions and 525 μm thickness, where a surface

(5500×5500 μm^2) with a hole in the middle (700×700 μm^2) uniformly dissipates a constant power during the heating time. With this power source the dissipation process of the different stripes is emulated, checking the thermal behaviour in the region under the sensing resistor. Thereby, the heating effect of all the stripes is approximated by only a surface uniformly dissipating the same total power flux as in the TTC. This is a valid hypothesis since all the stripes are very close between them. Moreover, the thin SiO_2 layer, placed between the Poly-Silicon and the Silicon substrate, has not been taken into account in the present simulations for the same reasons previously stated. The same boundary conditions as in 3.3.2.1 are taken into account, dissipating a 60 W overall the power source.

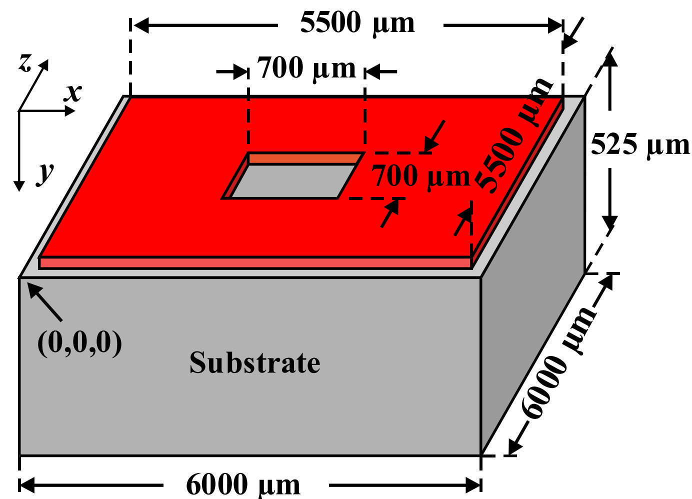

Figure 3.3.6. *Simulated structure, showing its dimensions (not to scale), for inspecting ΔT under the TTC sensor.*

Figure 3.3.7 illustrates, at different times, the *ΔT* profile corresponding to 1-D cut along *x* direction at *y*=0 μm and *z*=3000 μm. All the profiles reach their greatest values below the dissipating area, rapidly decreasing to a few Kelvins close to the border of the heating source. The most noticeable fact is that, under the area covered by the temperature sensor, *ΔT* is practically zero even at the end of the heating time. According to this simulation results, the sensor does not therefore allow a reliable temperature measurement on the TTC topside for the heating times considered in this work. From Figure 3.3.7, it can be also derived that vertical temperature profiles

must be measured avoiding the effects of the sense resistor. For instance, in Figure 3.3.7, the vertical temperature profile for *x* directions ranging from 0.75 to 2.4 μm and from 3.75 to 5.25 μm is the same as a homogeneous heat surface on the device topside. Furthermore, an abrupt decrease of ΔT is produced at the boundary of the dissipating area, implying that the interaction length between the heat flow and laser beam is approximately reduced to 5.5 mm. Subsequently, this value will be the interaction length considered for the extraction of ΔT values when equation (3.2.1) is used in section 3.5.

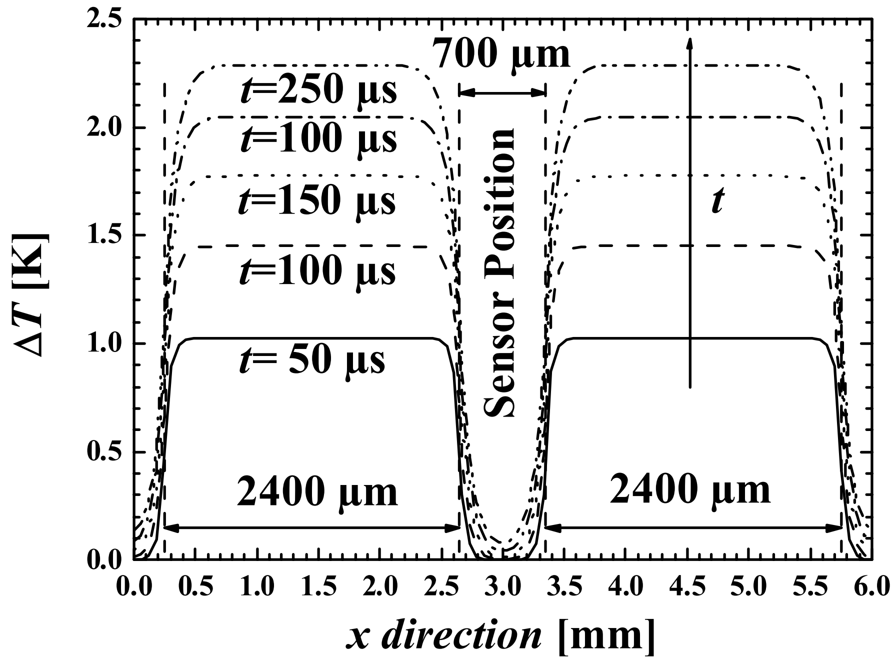

Figure 3.3.7. *Time evolution of ΔT 1-D cut along x direction performed at y=0 and z=3000 μm.*

3.3.3 TTC Modelling

According to simulation results from section 3.2.2.1, the evolution of the temperature rise inside the TTC may be described using the solution of the 1-D equation of heat conduction in a semi-infinite solid with a power source at y=0 dissipating a constant power P_0 in a given area A [63]:

$$\Delta T = -2\nabla_y T\,|_0 \left\{ \sqrt{\frac{D_\alpha t}{\pi}} \exp\left(\frac{-y^2}{4D_\alpha t}\right) - \frac{y}{2} erfc\left(\frac{y}{\sqrt{4D_\alpha t}}\right) \right\} \qquad (3.3.1)$$

where $\nabla_y T|_0$ and D_α denote the steady-state temperature gradient and the thermal diffusivity of Silicon, respectively. Moreover, $\nabla_y T|_0$ may be expressed as follows:

$$\nabla_y T|_0 = \frac{P_0}{Ak} \tag{3.3.2}$$

where A and k correspond to the device active area (30 mm^2) and the thermal conductivity of Silicon (0.148 W $mm^{-1}K^{-1}$ [64]), respectively. D_α may be derived from:

$$D_\alpha = \frac{k}{\rho c} \tag{3.3.3}$$

where ρ and c are the mass density of Silicon (2.33×10^{-6} kg mm^{-3} [64]) and the specific heat capacity of Silicon (713 J kg^{-1} K^{-1} [64]), respectively. Equation (3.3.1) shows that the time evolution of ΔT profile does not depend on the dissipated power level on the TTC top. In addition, a time constant τ_{heat} may be defined as follows:

$$\tau_{heat} = \frac{y^2}{4D_\alpha} \tag{3.3.4}$$

which gives the required time for obtaining a 15.73% of the ΔT steady state value at a given depth y.

3.4 The Thermal Calibration Procedure

The calibration procedure will exactly consist in estimating the vertical temperature profile from direct measurement, using equation (3.2.1), and comparing it with the model prediction of equations (3.3.2)-(3.3.4). To evaluate equation (3.2.1), aside from directly involved equipment parameters easily determined (L, κ', n_0, NA, f_{L_2}), the $(\partial n/\partial T)|_C$ value is also required. Subsequently, different values found in the literature, summarised in Chapter 2 (see Table 2.2), are employed. Thus, the main objective lies in identify the most suitable value for

$(\partial n/\partial T)|_C$ that fits the experimental temperature profile with the calculated one. For the proposed calibration procedure, the selection of the model parameters k and α is critical. The selected values have been taken from the literature for the experimental conditions of this work. k shows the main contribution on the uncertainty of the model prediction, and a 10% variation of its value is found depending on the different references. Nevertheless, equation (3.3.1) is very robust under the variation of this parameter. Namely, when k experiences a 10%, the temperature prediction shows a variation below 2% for all observed depths (from y=70 μm to 495 μm).

As experimental conditions, a maximum heating time of 250 μs has been chosen to be in the validity conditions of equation (3.3.1), as shown in subsection 3.3.2.1. Regarding the dissipated power on the TTC top, a maximum value of 60 W is selected, since the thermal conductivity and the thermal diffusivity remain constant for the subsequent temperature increase, as demonstrated in subsection 3.3.2.1. Heating time and dissipated power are controlled by the electrical excitation circuit already presented in Chapter 2. In Figure 3.4.1, a simplified schematic of the connection of the TTC to the electrical excitation circuit is depicted. The dissipated power is established by the level of the current pulse I_C conducted in the Poly-Silicon stripes (Joule effect), which is adjusted through the V_S voltage.

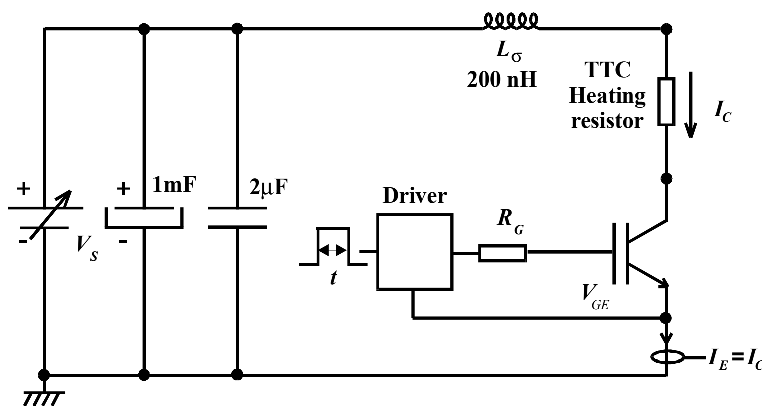

Figure 3.4.1. *Schematic illustrating the TTC connection to the excitation circuit.*

3.5 Equipment Thermal Calibration

3.5.1 Measured Signals and $(\partial n/\partial T)_C$ Selection

In the same experimental conditions, the obtained results for both TTC substrates (N- and P-type) do not excessively diverge between them. For this reason, in this section, the results corresponding to the measured $V_{out,y}$, as well as the influence of the thermo-optical coefficient to ΔT estimation, are shown for the P-Type TTC. Figure 3.5.1 shows the time evolution of $V_{out,y}$ at the various depths considered in this work during a heating time of 250 μs for P_0=60 W. As inferred from equation (1), note that $\nabla_y T$ follows the same behaviour as $V_{out,y}$. For measuring depths close to the chip top (70 μm, 95 μm, and 120 μm), $V_{out,y}$ presents oscillations. They are due to interference phenomena on the detector surface, as a result of the superposition of the probe beam (main ray) with its multiple reflections into the TTC lateral sides [28]. Its origin is a consequence of the refractive index increase with temperature, which changes the optical path between all the interacting rays (Fabry-Perot interference). This effect is more important closer to the heat source, since the temperature increase is higher. Figure 3.5.2 depicts the aforementioned comparison between theory and experiment for t=250 μs to stress the $(\partial n/\partial T)_C$ coefficient influence on the determination of ΔT. In this case, the non repeated values of Table 2.2 (Chapter 2) are used to evaluate equation (3.3.1), obtaining the dispersion in ΔT observed in Figure 3.5.2. The best agreement with the theoretical model is achieved considering Magunov's coefficient value [42], being the suitable thermo-optical coefficient in the present case. It can be observed that the estimated ΔT using Magunov's, Bertolotti's and Li's reported values agree between them and diverge from the estimation corresponding to Seliger's coefficient when their experimental error is considered. This difference might arise from the experimental method followed by Seliger et al. Whilst the former measured both the refractive index and the temperature variation for $(\partial n/\partial T)_C$ determination, Seliger et al. obtained this value comparing FPI measurements with a simulated temperature profile [46].

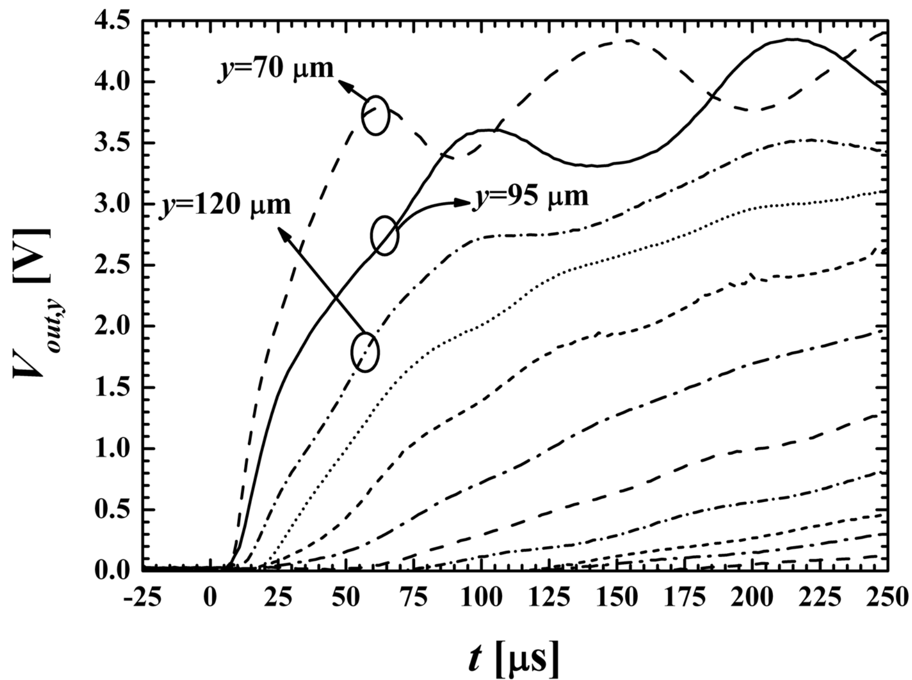

Figure 3.5.1. *Heating time dependence of the measured $V_{out,y}$ waveforms at different measurement depths, ranging from 45 µm to 470 µm with 25 µm steps.*

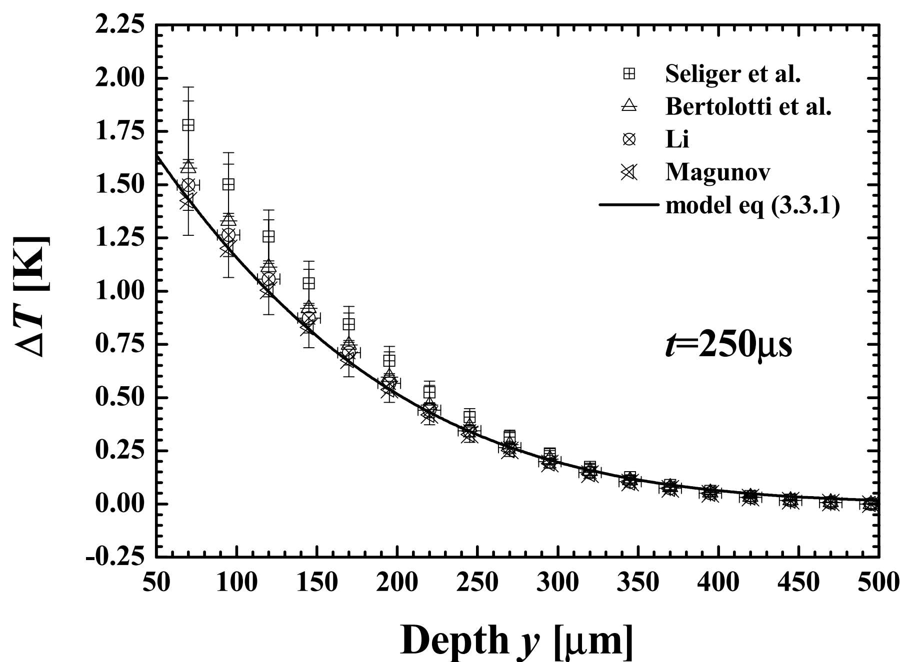

Figure 3.5.2. *Extracted temperature profile evaluated for* $(\partial n/\partial T)_C$ *reported values and its comparison with the prediction of equation* (3.3.1) *for t=250 µs.*

3.5.2 Temperature Rise Measurements

Once the suitable thermo-optical coefficient is found, reliable ΔT values can be measured in both kinds of TTC substrates. Thus, aside from direct comparison between 1-D model and measurements, the obtained results are verified. This is possible since $(\partial n/\partial T)_C$ does not depend on doping level [42, 65], and subsequently, the thermal proportionality factor is not also affected. Figure 3.5.3 presents the model prediction on ΔT and the experimental results using the Magunov's coefficient for different heating times. These results are contrasted for each TTC type, presenting the P-type case in Figure 3.5.3 (a) and the N-type in Figure 3.5.3 (b). As observed, a very good agreement between theory and experiment is obtained.

For further verification, ΔT inside the N-type TTC is also measured for two different P_0 values and compared with the model prediction, as shown in Figure 3.5.4. Concretely, Figure 3.5.4 (a) and (b) depict ΔT comparison for P_0=30 W and P_0=15 W, respectively, ranging the heating time from 50 μs to 250 μs. From these results, it can be observed as the measured ΔT in both cases are scaled by a factor 2 which corresponds to the ratio between dissipated powers. This fact agrees with theory as it can be inferred from equation (3.3.1), where, at a given time, ΔT value only depends on the dissipated power. In both cases, the difference between measurements and model prediction is 17% for t=50 μs, but, from t=150 μs, it is drastically reduced below 5%. This higher difference for short heating times (t=50 μs and t=100 μs) can be associated to experimental limitations. However, the accuracy of this technique allows, inside a 6×6 mm^2 chip, ΔT measurements as lower as 100 mK with a discrepancy from the model prediction of 17 mK.

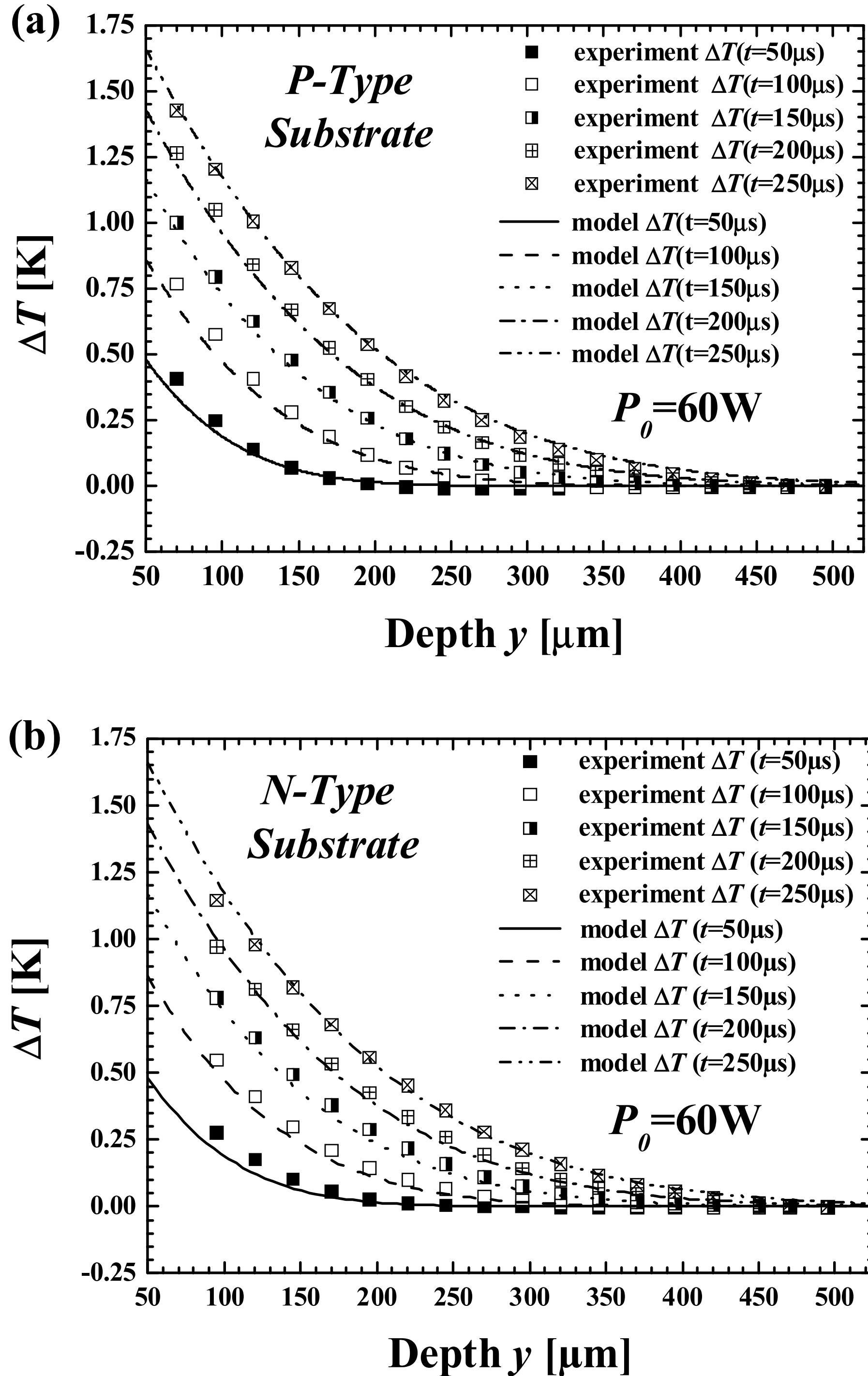

Figure 3.5.3. *Extracted temperature profile compared with the prediction of equation* (3.3.1) *for several heating times, using* $(\partial n/\partial T)_C$ *Magunov's value, for:* (*a*) *P-type substrate and* (*b*) *N-type substrate. Points are experimental values and lines display the predictions of the considered model using equation* (3.3.1).

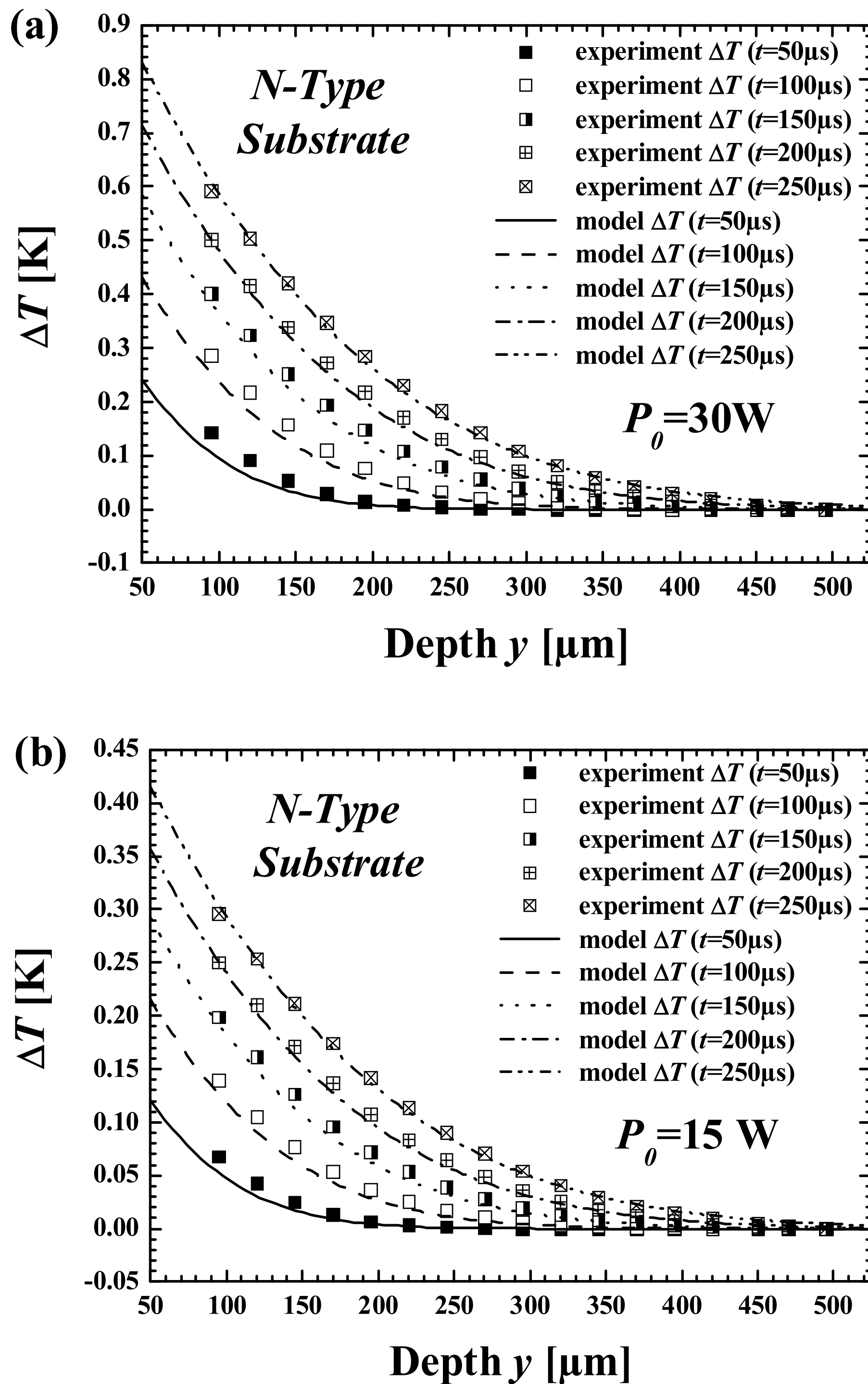

Figure 3.5.4. *Comparison between the model results and the extracted temperature profile from the N-type TTC for (a) P_0=30W and (b) P_0=15W for several heating times, using $(\partial n/\partial T)_C$ Magunov's value.*

3.6 Conclusions

A thermal calibration procedure for the IIR-LD equipment shown in Chapter 2 is presented. The method is based on a thermal test chip, whose behaviour is well described by an analytical thermal model. The structure of the thermal test chip is basically a 525-μm Silicon substrate with a heating resistor on its top. During short heating times (250 μs), a vertical heat flow is created inside the chip, maintaining its backside temperature constant. In these conditions, IIR-LD measurements have been performed at different depths, obtaining the corresponding voltage deflection signals. These signals have been numerically integrated along the observation depth for different heating times (ranging from 50 μs to 250 μs). From these results, the temperature rise is estimated by means of equation (3.3.1). In this expression, different reported values for the coefficient $(\partial n/\partial T)_C$ are taken into account for its evaluation, since $(\partial n/\partial T)_C$ introduces the highest error in $\nabla_y T$ determination. From comparing experimental results and model predictions, a discrepancy less than 17% between theory and experiment is reached in the worst case selecting a $(\partial n/\partial T)_C$ of 2.0×10^{-4} K^{-1} when a temperature rise ranging from 0 to 1.4 K is measured. Therefore, the presented procedure can be used to thermally calibrate optical probing equipments for measuring thermal behaviour of power devices, as well as to determine thermal parameters of other materials, such as SiC and GaN. The method benefits are that the fabrication of a TTC is easier than an active device, such as power MOSFET, due to its higher structural simplicity.

Chapter 4

Free-Carrier Concentration Measurements on Diodes

4.1 Introduction

In order to show the equipment performances in free-carrier concentration measurements, high power diodes are measured. Concretely, the profiles of free-carrier concentration and their decay time along the drift region are compared between an irradiated and unirradiated device. As explained in Chapter 1, the irradiation of bipolar devices is a common lifetime killing technique to improve their switching response, which changes the free-carrier behaviour inside the drift region of the device. This fact is totally evidenced in the performed measurements, where very different free-carrier distributions are obtained. Moreover, experimental results are also verified by electrical simulations, since, even if such diodes are not specifically fabricated for this work, their internal characteristics and relevant electrical parameters are well known. As a result, a good agreement between simulation results and experiment is found, demonstrating the suitability of the proposed IIR-LD experimental rig , not only for temperature measurements, but also for detailed electrical characterisation of power devices. Unfortunately, measurements of temperature increase only originated from device self-heating can not be performed due to the presence of a high contact resistance introduced during the preparation process, as discussed further on.

4.2 Lifetime Killing Methods

In lifetime killing [2], a defect distribution is generated inside bipolar power devices. These profiles may be created by diffusing into the device noble metal atoms or irradiating them with electrons or ions. In the former case, platinum or gold are diffused by means of a post implantation "drive in" process at high temperatures (700-1000ºC). Such process is performed before completing device fabrication, since the contact metallization will not withstand these temperatures. As a consequence, a constant risk of contamination of other equipments or technological process is possible. In addition, the used metals are extremely rapid diffusers, being very difficult to control and reproduce the resulting defect profiles.

During device irradiation, incoming ions or electrons collide with target Silicon atoms, creating unstable mobile interstitials and vacancies. Subsequently, to stabilize them, an annealing process (200-350ºC) is followed. From the device electrical performances point of view, the most important are the divacancies $V_2^{(-/0)}$ and vacancy-oxygen pairs $VO^{(-/0)}$, which control the device electrical behaviour during low and high injection regimes [66], respectively. Although defect concentration depends on several factors, once the irradiation and annealing processes are well-established the projectile energy and fluence constitute the main parameters for the device turn-off optimisation. This technique allows reaching a high reproducibility in defect creation, with the added advantage that is performed as a back-end fabrication process.

Depending on the selected method, different profile shapes are created. Noble metals usually provide a U-shaped defect distribution along the device. In electron irradiation a uniformly decreased lifetime along the device is obtained. By contrast, defect profiles originated from ion irradiation show a prominent defect peak followed by a residual tail resulting from both the electronic and nuclear stopping. This difference between the profile shapes in ion and electron irradiation is ought to the much higher mass of ions, limiting the ion penetration range to be lower than the usual thickness of power devices. The peak position and its concentration level are

usually tailored by selecting the irradiation energy and projectiles fluence, respectively. With this technique a spatially local control of free-carriers lifetime is possible, giving a lot of advantages from the other ones. Nowadays, the trend is to combine ion irradiation with electron irradiation and noble metal diffusion, obtaining taylored lifetime profiles inside the device [67].

Up to now, the previous studies for optimal irradiation processes have been assisted by numerical simulation of involved physical phenomena [68], in which an accurate selection of the physical models and their correct parameters is required. Although existing traditional techniques, e. g., deep-level transient spectroscopy (DLTS) or C-V profiling, may provide information about recombination centres characteristics (energy levels and spatial distribution), the evolution of free-carrier concentration in the drift region for a biased device is not directly measured. In this framework, the free-carrier absorption technique has provided a spatially well-resolved way to tackle this problem. By means of this technique, Rosling et al have measured the free-carrier concentration with electron and proton irradiated PIN diodes [69]. In this chapter, similar measurements with alpha irradiated power diodes will be performed to demonstrate the developed experimental rig functionality in free-carrier concentration measurements.

4.3 Diode Structure and Experimental Conditions

4.3.1 Diodes Characteristics

The studied devices are 100 A/2.5 kV circular power diodes (16 mm diameter, 2 cm^2 area) fabricated by Polovodiče a. s. (Prague) on 110 Ωcm N-type Silicon (FZ NTD <111> oriented) [70]. Their total thickness is 390 µm, also considering top and bottom aluminium contacts (10 µm each one). As depicted in Figure 4.3.1, their internal structure is based on $P^+PN^-N^+$ layers, showing a wide drift region (297 µm). This fact is an important issue, since it allows the free-carrier measurement inside the device without having spatial restrictions imposed by the sample dimensions.

Regarding diodes termination, it consists in a positive bevel with surface passivation using rubber forms. The ion irradiation process, which has been designed by J. Vobecký, has been performed through the anode with a low fluence (10^{10} cm^{-2}) for a given energy of 11 MeV. Afterwards, all diodes have been annealed at 200 ºC during 60 minutes to stabilise radiation defects. As a result, the carrier lifetime is slightly altered close to the PN junction depth.

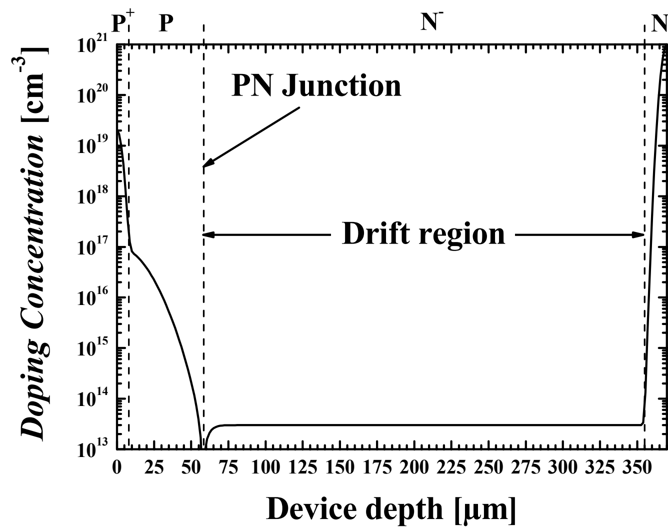

Figure 4.3.1. *Internal structure of the studied devices.*

4.3.2 Experimental Conditions

As for the samples preparation, the diodes have been cut in stripes (diode stripes) of 1.65×10 mm^2 and, afterwards, all their lateral faces have been polished. Thereby, the spatial resolution and radiation power transmission are enhanced, as well as the recombination process on the faces is also reduced. After that, the diode stripes have been finally soldered and bonded on a power substrate (Insulated Metal Substrate). This last step introduces a high contact resistance on the measured samples, since their standard mounting is in press pack housing, supporting pressures about 100 kN/cm^2. However, depending on the chosen biasing conditions, this parasitic resistance would not excessively influence on the real distribution of free-carrier concentration inside the device. For this reason, the device is biased with short current pulses of low intensity using the DUT excitation system, previously

described in Chapter 2. An IGBT is connected in series with the resistive load and the diode under test, as shown in Figure 2.8.2. Switching on and off the IGBT, the diode is forward biased with current pulses up to 11 A/cm^2 during 84 μs. Thus, device self-heating effects, as well as contact heating problems or current instabilities due to the high contact resistance, are avoided.

Basically, all measurements will be performed inside the drift region, since all relevant physical phenomena related to forward current conduction in diodes are produced there. As previously explained, C is determined from power signals detected when the device is in off- and on-state ($V_{out,P0}$ and $V_{out,P}$, respectively) by using expression (2.3.1), i. e.:

$$C = \frac{1}{L\left(\frac{\partial \alpha}{\partial C}\right)_T} Ln\left(\frac{V_{out,P_0}}{V_{out,P}}\right) \tag{4.3.1}$$

As a calibration constant $(\partial\alpha/\partial C)|_T$, the reported value by Schlögl [40]:

$$(\partial\alpha/\partial C)|_T = 8.08\times10^{-18}\ \text{cm}^2$$

is taken into account. This value was obtained from a calibration process for a FCA equipment at a laser wavelength of 1.3 μm with specifically designed PIN diode structures. The diode structures were biased at low current densities (below 1 A/cm^2) to avoid influence of carrier concentration on all semiconductor physical parameters (carrier mobility, lifetime, etc.), being approximately constant. These conditions are very similar to the ones of the present work.

4.4 Simulation Aspects of the Analysed Diodes

4.4.1 Simulations Motivation

In order to qualitatively corroborate the measured profiles of C, device simulations using the software package ISE-TCAD [71] have been performed. In such electrical simulations, the key point lies on the correct adjustment and comprehension of

recombination models supported by the simulation package. Furthermore, simulation results also allowed the analysis of the effects of surface recombination in the polished lateral faces of the diode stripes.

4.4.2 Considerations on Recombination Processes in Simulations

In Silicon devices, two main mechanisms are responsible of recombination processes during device conduction state: multiphonon assisted (Shocley-Read-Hall model –SRH–) and band-to-band Auger [72]. The former consists in electron-hole pair recombination thanks to the presence of material structural defects; whereas, the latter is a process in which an electron and a hole recombine in a band-to-band transition by means of a third carrier. At low and medium free-carrier concentration, the SRH recombination is the dominant process, taking a higher importance the Auger mechanism from 10^{18} cm^{-3}.

From the simulation point of view, Auger lifetime can be easily calculated since it basically depends on the free-carrier concentration, which is iteratively computed from semiconductor equations. Nevertheless, SRH mechanism has a complex transient model [71] where a detailed knowledge of the defect structure is required. Physically, structural defects introduce allowed energy levels in the bandgap (energy deep-levels) that thermally capture or emit carriers. In SRH dynamic model, all electron transitions between conduction band, deep-levels and valence band are considered, following various restrictions. Once a state associated to an energy deep-level (trap or recombination centre) is filled by an electron, it can not accept another one. This carrier occupying the trap can in a second step fall into an empty state in the valence band, thereby completing the recombination process in two steps. The generation process occurs conversely. This process must be taken into account for each one of the created defect types.

Another important aspect in SRH recombination processes is that they can be produced either inside the bulk or at the material interfaces, e. g., interface Silicon-air. In bulk recombination, electrons and holes have associated a characteristic time

called minority carrier lifetime, which is related to either electrons (τ_n) or holes (τ_p) for a given energy deep-level E_T with a density of states N_T. Both parameters are expressed as:

$$\tau_n = \frac{1}{\sigma_n v_{th,n} N_T} \tag{4.4.1}$$

$$\tau_p = \frac{1}{\sigma_p v_{th,p} N_T} \tag{4.4.2}$$

where $v_{th,n}$ ($v_{th,p}$) and σ_n (σ_p) correspond to the thermal velocity of electrons (holes) and trap capture cross section for electrons (holes), respectively. In diodes, when the high injection condition is reached, the carriers lifetime due to SRH mechanism (τ_{SRH}) is given by the direct addition of τ_n and τ_p [73]. τ_{SRH} can be easily measured by means of Open Circuit Voltage Decay (OCVD) method [74], facilitating the device modelling. By contrast, in surface recombination, each carrier has associated an equivalent parameter: the surface recombination velocity (S_{SRH}). However, the measurement of such velocity is very difficult. Moreover, when surface recombination is not assumed, the performed simulations are less time consuming because of the less complex structure requirement. This dilemma about the consideration of surface recombination on the polished surfaces of the tested diode stripes is further discussed in the next subsection.

4.4.3 Stripe Diodes Preparation Effects on *C*

Electrical simulations have been performed to evaluate which is the incidence of surface recombination effects on the *C* profiles. The simulated structure corresponds to half cross section of a diode stripe flowing a current density of 8 A/cm^2, where the interface defined between air and Silicon at one of the lateral sides is also assumed. As a parameters, $\tau_{SRH} = 94$ µs and $S_{SRH} = 2800$ cm/s are used. They are extracted from OCVD measurements on the device and reported values measured in Silicon wafers polished surfaces [75], respectively. Only the electron concentration in steady state (C_n) is discussed here, since both free-carriers types have the same

concentration in the inspected region. Moreover, the obtained results are discussed in terms of C_n normalized to its highest value achieved close to the PN junction ($C_{n,max}$). Thereby, the presented results allow the direct visualisation of recombination surface effects in percentual mode.

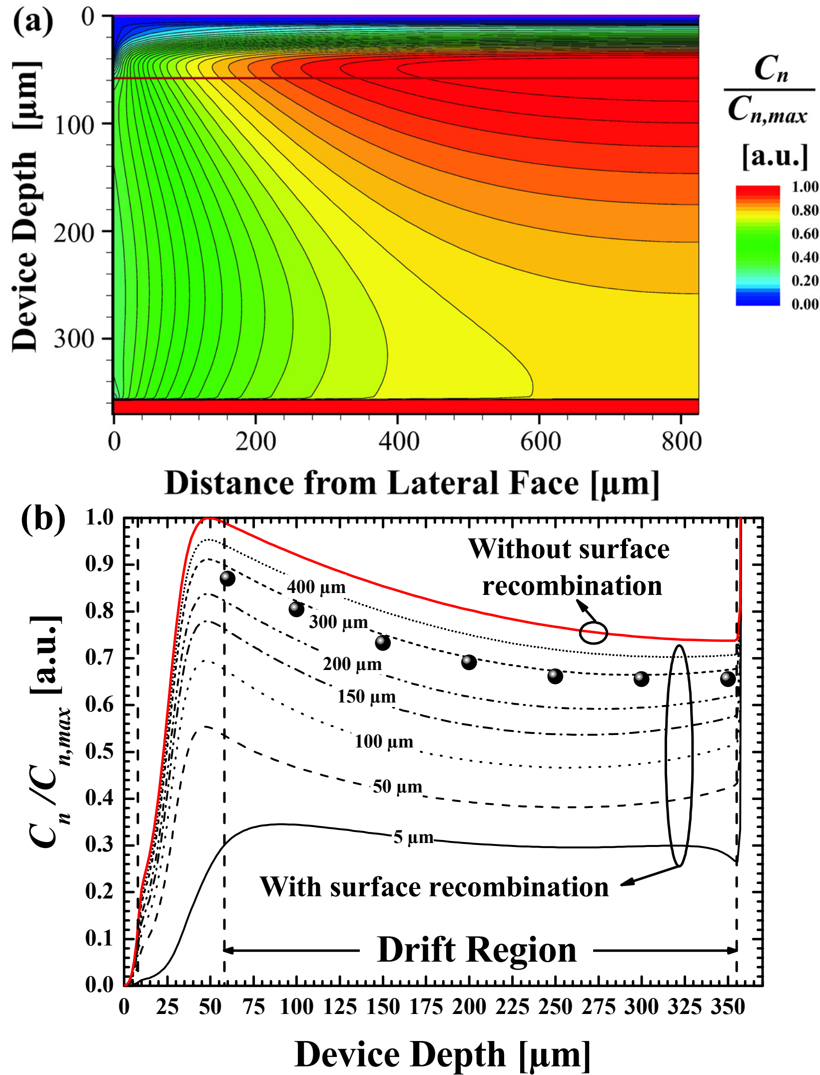

Figure 4.4.1. (*a*) *2D electrons density inside the simulated unirradiated diode where a surface recombination velocity of 2800 cm/s is considered.* (*b*) *Comparison of one-dimensional vertical profiles of electrons concentration obtained from considering* (*black lines*) *and not considering* (*red line*) *recombination at lateral faces, as well as electrons concentration average along the interaction length* (●).

Figure 4.4.1 (a) and (b) contain both the 2-D and 1-D cuts of $C_n/C_{n,max}$. Figure 4.4.1 (a) visually shows how at 600 µm from the polished lateral face, $C_n/C_{n,max}$ profile in the drift region experiences a transition from a 1-D vertical profile to a 2-D

distribution, gradually decreasing until it reaches a constant value of 30 % at the lateral face. This effect is clearly evidenced in Figure 4.4.1 (b), where the consequences on assuming the surface recombination is depicted. In this figure, various vertical cuts of $C_n / C_{n,max}$ ranging the distance from the lateral face between 5 to 400 µm (black lines) are compared with the simulation results without assuming such surface effects (red line). From these simulation results assuming surface effects, C_n profiles at several depths inside the drift region have been averaged along the half interaction length (in the figure, distance from lateral face) to estimate the influence of surface recombination on measurements. After normalising them to $C_{n,max}$ (●), they are also represented in Figure 4.4.1 (b). As observed, only a deviation of 14 % from simulation results without considering surface effects is obtained. Thus, since the consideration of such effect in polished faces does not excessively modifies the simulation results, only bulk recombination will be assumed in all the performed simulations.

4.4.4 Simulation Procedure

For performing predictive simulations, τ_n and τ_p have been determined by fitting the experimental and simulated forward I-V characteristics of each diode varying N_T, σ_n and σ_p values. The lifetime value previous to alpha irradiation has been extracted from the fitting process of the unirradiated diode. To account for the irradiation effects on carrier lifetime, the primary defect profiles generated from ion irradiation are simulated with a Monte Carlo simulation code called SRIM (Stopping and Range of Ions in Matter) [76], taking into account the projectile type, its energy and fluence. In this profile, only two types of defects, i. e., divacancies $V_2^{(-/0)}$ and vacancy-oxygen pairs $VO^{(-/0)}$, are considered. As aforementioned, each of them determines the lifetime change during the diode forward regimes of low and high injection, respectively. Finally, the profile corresponding to each defect is rescaled until obtaining a good fitting between experiment and simulation. In this last step, σ_n and σ_p values are taken from the reported values in [77].

4.5 Free-Carrier Concentration Measurements

4.5.1 Time Evolution of Free-Carrier Concentration

Figure 4.5.1 (a) and (b) show the typical waveforms of C inside the drift region at various depths (y, origin taken at PN junction) of the irradiated and unirradiated devices (current density of 8 A/cm^2), calculated from measured power signals by using expression (4.3.1). As this figure shows, the evolution of C is well resolved in time thanks to the good time response of the designed post-processing circuit, shown in Chapter 2. The peaks of the C waveform at turn-on and -off instants are induced by the excitation circuit (IGBT switching and stray inductances). From these graphs, it is clearly evidenced that C increases with time until reaching its steady state value in both devices. In steady state, the irradiated diode has a lower level of free-carriers closer to the ion penetration range, and shows a C increase of 50% along the device drift region. On the contrary, the unirradiated diode shows a higher C value with a lower variation (22%) along the drift region. Once the IGBT is switched off, the behaviour of C during the diode turn-off is also observed depicting the free-carriers decay by recombination. As observed from Figure 4.5.1, both devices show different free-carriers decay waveforms. For a further insight to these differences in behaviour between irradiated and unirradiated devices, the measured profiles of C in steady state (C_{SS}) and the decay time (τ_{dec}) along the drift region are analysed in the next section, also comparing C_{SS} measurements with simulation results. τ_{dec} has been derived by fitting a exponential decay function and extracting the corresponding time constant.

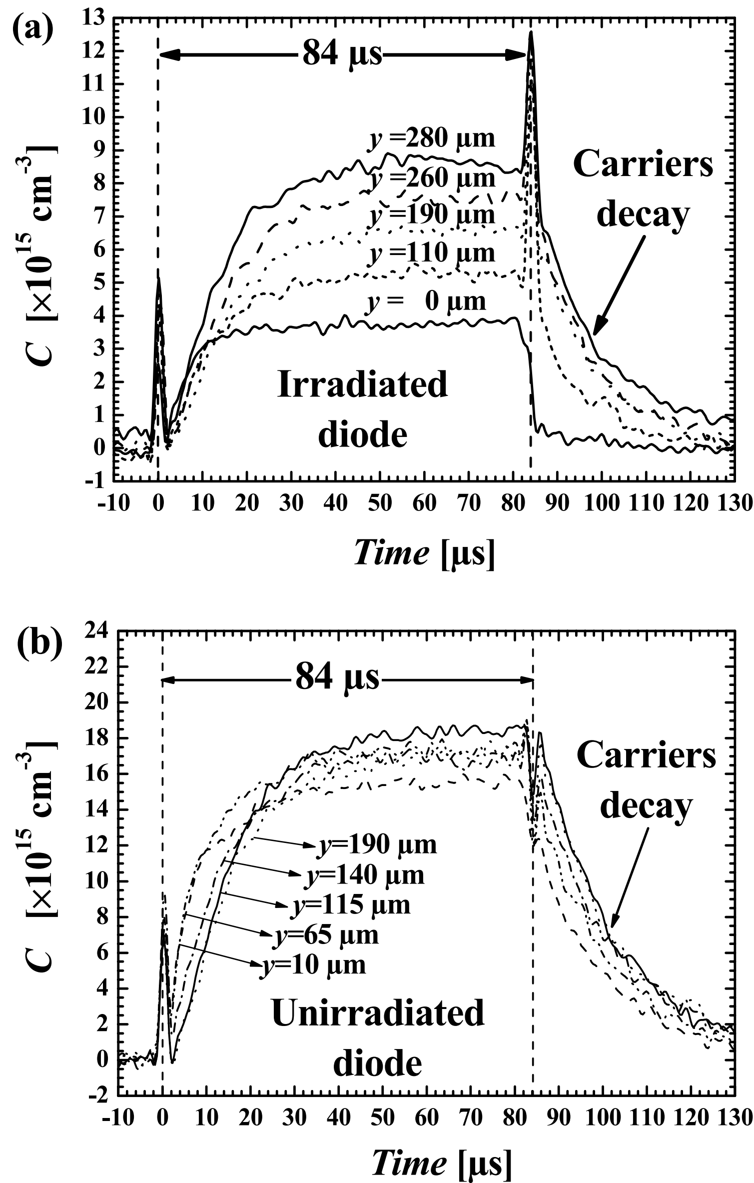

Figure 4.5.1. *Measured waveforms of the time evolution of free-carrier concentration at various depths inside the drift region* (*y*) *for irradiated* (*a*) *and unirradiated* (*b*) *diodes, when a current density of 8 A/cm^2 is flowing through them.*

4.5.2 Steady State Free-Carrier and Decay Time Profiles

Figure 4.5.2 graphically illustrates the ion irradiation effect on C_{SS} at a current density of 5 A/cm^2. In this graph, the experimental (points) and simulation (solid lines) results are compared. In addition, the background doping profile (brown dashed line) is also shown for a better comprehension. From the simulation results, it

can be observed that the electron (C_n, black solid lines) and hole (C_p, red solid lines) concentrations reach the same level along the drift region for both devices (high injection condition). By contrast, C_p and C_n are very different outside this region. Depending on the difference between free-carriers and doping concentrations, C_n and C_p either increase following the doping profile (majority carrier case) or rapidly decrease to very low concentrations (minority carrier case). The main difference between both devices stems from the behaviour of C_n and C_p in the drift region. In comparison to the unirradiated case, the created defects at the ion penetration range induce a decrease in C_{SS} along the drift region. As Figure 4.5.2 shows, this fact is experimentally observed, obtaining a good agreement with simulation results.

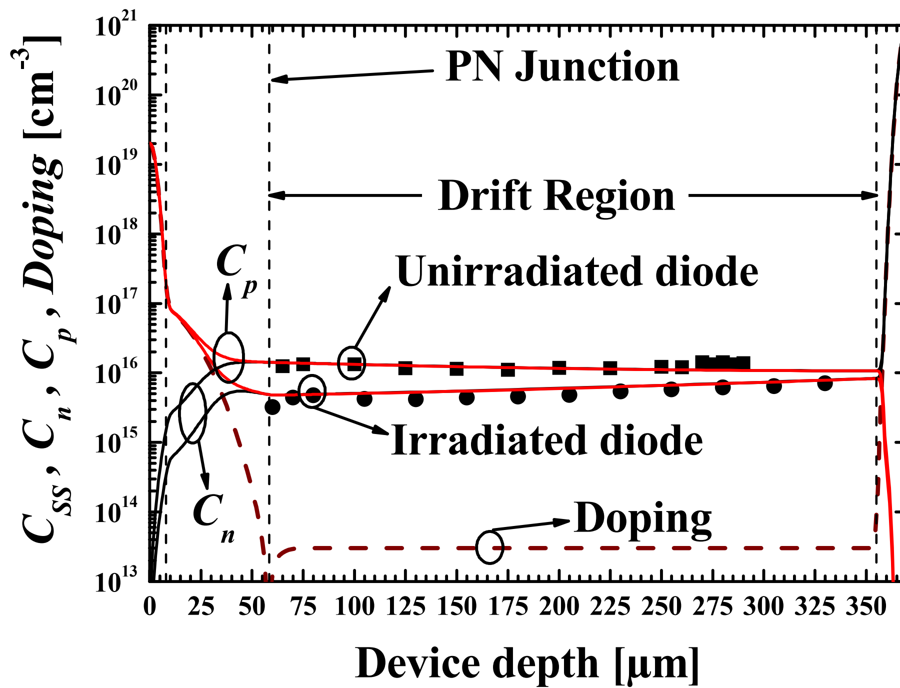

Figure 4.5.2. *Comparison between experiment (■,●) and simulation results (solid lines) for both devices, also showing holes (red solid lines) and electron (black solid lines) densities (C_p, C_n), as well as the doping profile (brown dashed line), along the entire device.*

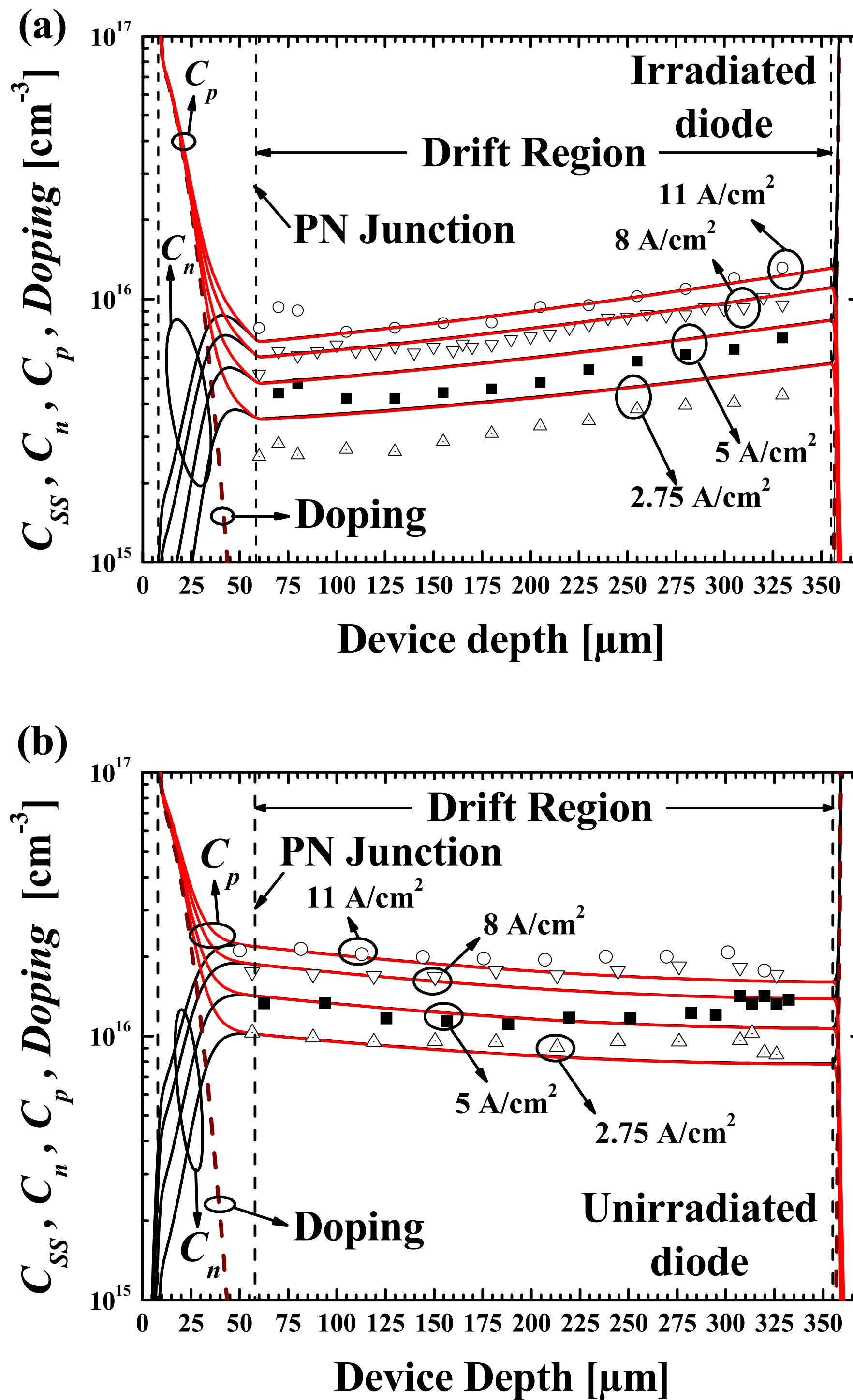

Figure 4.5.3. *Comparison of free-carriers in the drift region between measurement (points) and simulation (solid lines) at current densities of 2.75 (△), 5 (■), 8 (▽), and 11 (○) A/cm² for both diodes: irradiated (a) and unirradiated (b). From simulation results, holes (red solid lines) and electron (black solid lines) densities (C_p, C_n), as well as the doping profile (brown dashed line) are also shown.*

Figure 4.5.3 (a) and (b) illustrate the dependence of C_{SS} profiles on current density for the irradiated and unirradiated diodes, respectively. For this purpose, several C_{SS} profiles have been determined from measurement and simulation at 2.75, 5, 8, and 11 A/cm^2. From this graph, it can be extracted that in both cases, C_{SS} increases with the current density, maintaining its profile shape. From the comparison between simulation and experiment, they qualitatively agree, as well. As observed from Figure 4.5.3 (a), the difference in values between experiment and simulation increases, when the current density decreases. Nonetheless, the higher discrepancies between experiment and simulation are observed in the unirradiated diode when C_{SS} is measured closer to the cathode side. As Figure 4.5.3 (b) shows, experimental points deviate their trend respect the simulation results. This fact could be due to the aforementioned problems in the diode stripe mounting. In particular, from the measured I-V characteristic, a peculiar quadratic shape is observed that should be explained with a current-dependent contact resistance or N$^+$ emitter efficiency [27]. All these relevant physical effects are not considered in the performed device simulations.

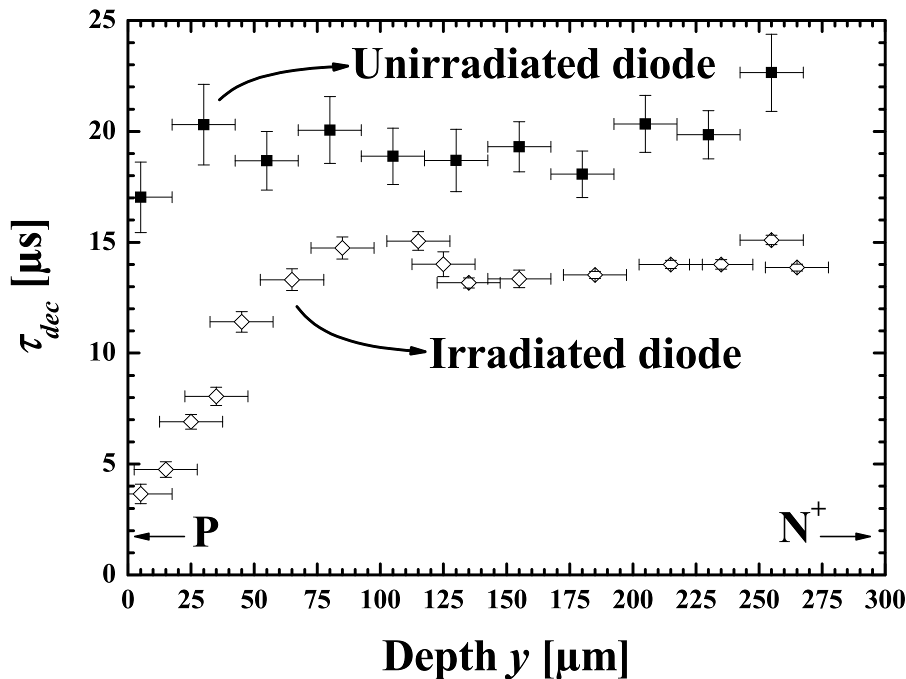

Figure 4.5.4. *Comparison between the measured carriers decay time τ_{dec} for both devices* (■, *unirradiated;* ◇, *irradiated*).

Figure 4.5.4 compares τ_{dec} between both diodes only in the drift region (y, origin is at the junction). The error in τ_{dec} is obtained from the exponential fitting performed on the carrier decay of the measured C waveforms. Its spatial error is associated to the beam radius averaged along the interaction length with the diode (±12.5 μm). The main difference between them is the sudden increase of τ_{dec} from 4 to 15 μs experienced closer to the ion penetration range (PN junction) for the irradiated diode (■), which contrasts to the constant profile (around 20 μs) obtained in the other case (◇). This fact gives evidence for the local lifetime change, as previously noticed, and allows direct observation of the irradiation effects inside the device.

4.6 Conclusions

In order to show the functionality in free-carrier concentration measurements of the developed IIR-LD equipment, the ion irradiation effects on free-carrier concentration of power diodes have been experimentally determined. For this purpose, the free-carrier concentration is measured in an irradiated and unirradiated diode. From the comparison between experimental results, it is clearly demonstrated how the free-carrier concentration in steady state, jointly with carriers decay time, are modified. Such measurements have been performed biasing the diode at low current density levels (up to 11 A/cm^2) during short times (84 μs) to avoid the parasitic effects of the high contact resistance existing between substrate and diode. Moreover, due to the heating effects associated to this resistance, internal temperature increments purely due to device physics can not be measured. For this reason, further efforts must be directed towards packaging improvement for this type of samples prior to proceed to the internal temperature measurement. For further verification of experimental results, the measured free-carrier concentration has been compared with the derived one from performed electrical simulations. The agreement between both is qualitatively good. Simulation and measurements show that in irradiated diodes, a higher discrepancy at lower current densities is observed, whereas in the other devices, the deviation is higher close to the cathode. This fact should be related to experimental limitations on current measurements performed by a hall effect probe,

IIR-LD set-up accuracy and relevant effects not considered in the performed simulation. Despite all these problems, the time related to waveforms decay, which depends on free-carriers lifetime, at various depths and free-carriers concentration along the drift region have been extracted, being possible to observe the local effects induced by the irradiation process.

Chapter 5

IIR-LD MEASUREMENTS ON IGBTs

5.1 Introduction

In order to show the versatility and spatial resolution of the developed IIR-LD experimental rig, electro-thermal phenomena in a very thin region inside 600 V PT-IGBTs are inspected. Concretely, unirradiated and proton irradiated 600V PT-IGBT devices (5.9×5.9 mm^2) are investigated. In these devices, the dimensions of the drift regions are similar to the beam diameter. Under these spatial restrictions, the free-carrier concentration and temperature gradient are measured only in the middle of the low doped region. From the temperature gradient measurements, two thermal parameters, i. e., heat diffusion time and temperature gradient in steady state, are extracted by using a simple analytical model.

5.2 Importance of IGBTs in Power Electronics

Due to the diversity of Power Electronics applications, the development of a unique power switch has been impossible [78]. However, the commercial power switch which currently covers a wider application range are IGBTs. This versatility arises from its hybrid nature between bipolar and MOS-gated transistors, i. e., low forward voltage drop and voltage gate control. Thus, IGBTs offer a current handling capacity ranging from 20 A to several kA, a blocking voltage up to 6.5 kV, and a maximum switching frequency up to 50 kHz . These performances are achieved thanks to new design concepts, which have provided them this spectacular growth in the last 10 years.

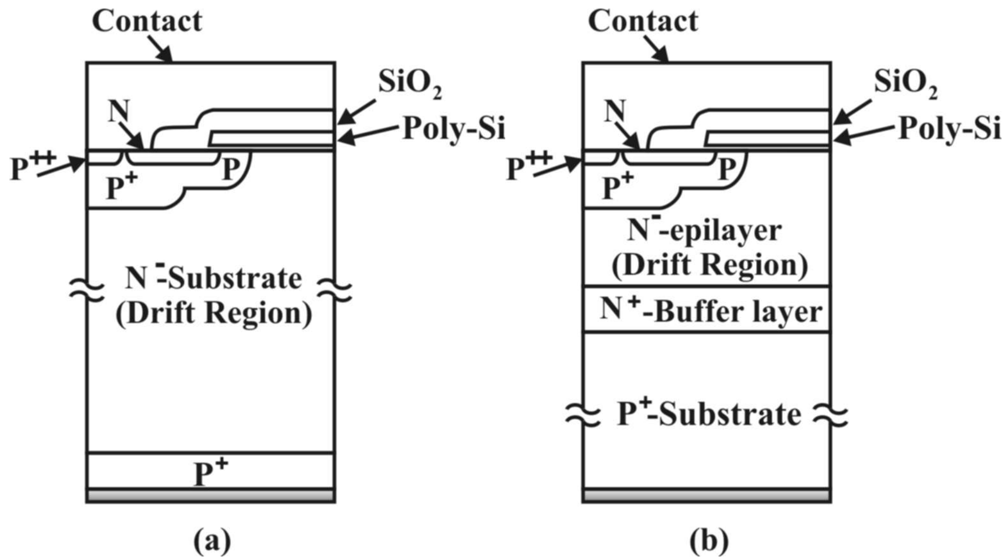

Figure 5.2.1. *View of the basic half-cell cross-sections of the main types of IGBTs:* (*a*) *NPT-IGBT* (*b*) *PT-IGBT.*

From the technological point of view, IGBTs, as well as power MOSFETs, comprise an array of thousands of single cells (or basic cells) interconnected in parallel that allows them conducting the current ratings required in power applications. Depending on their basic cell structure (c.f. Figure 5.2.1 (a) and (b)), they may be categorised in punch-trough (PT) and non-punch-trough (NPT). In both cases, the basic cell consists of a PNP bipolar transistor (P^+ injecting layer, N^- drift region, and P body) whose base (drift region) is driven by a N-channel MOSFET (N^- diffused region, body, and drift region). Depending on the gate voltage, the N-channel is turned-on or turned-off, controlling the base current. Thereby, the carrier injection process is monitored. In the blocking state, apart from the device terminations, the voltage is supported by the junction between the drift region and P body. The main structural difference between both types of IGBTs is the presence of an additional N^+-layer (buffer layer) in PT-IGBTs, as observed from Figure 5.2.1 (a) and (b). Thanks to this layer and with the same edge termination structure, PT-IGBTs may support the same blocking voltage as their counterparts with a thinner drift region . As in the case of diodes, IGBTs also store a certain amount of carriers in the drift region that increase their power losses and time response during the turn-off. This feature can be improved by applying lifetime killing methods. Nowadays, these

techniques are widely used in NPT-IGBTs [79] specially ion or proton irradiation, as explained in the previous chapter. In order to perform temperature measurements inside IGBTs, NPT-IGBTs are better candidates than their counterparts because of their wider drift region (high blocking voltages), allowing the inspection inside the device at various depth. However, NPT-IGBTs have not been available in this work, presenting only thermal phenomena measurements in PT-IGBTs. This fact introduces some difficulties for the determination of temperature increase inside such devices, as explained in the next sections.

5.3 PT-IGBTs Structure and Experimental Conditions

5.3.1 PT-IGBTS Caracteristics

The studied devices are squared 5.9×5.9 mm^2 600V PT-IGBTs fabricated at clean room facility of Centre Nacional de Microelectrònica (CNM). Its fabrication process includes 8 photolithographic steps on 4 inch <100> wafers. In order to proceed to proton irradiation of the fabricated devices, the processed wafers have been polished from the backside and their final P^+-substrate thickness was 375 μm. Its internal structure corresponds to a P^+-substrate (boron doping concentration of 2×10^{19} cm^{-3}), N^+-buffer layer (thickness of 10 μm and phosphorus doping of 10^{17} cm^{-3}) and N^--epilayer or drift region (thickness of 60 μm and phosphorus doping of 10^{14} cm^{-3}). All these dimensions have been summarized in Figure 5.3.1, where the cross-sectional view of the IGBT basic half-cell is shown. In this case, the inspected region is much thinner than the previously studied diodes. This fact restricts the temperature gradients measurements inside the drift region, as explained futher on.

Designed by J. Vobecký [80], the proton irradiation process was performed from the device backside, avoiding damage in the MOS structure of the IGBT. As a result, a defect concentration peak inside the drift region, 54 μm from the device topside, has been obtained for a proton energy of 7.35 MeV and a dose of 3×10^{12} cm^{-2}. The devices irradiated with these parameters are not optimal from the application point of view, since they present high power dissipation losses (high forward voltage drop)

during on-state. Nevertheless, they have been useful to validate the IIR-LD equipment comparing their thermal behaviour with that of the unirradiated devices.

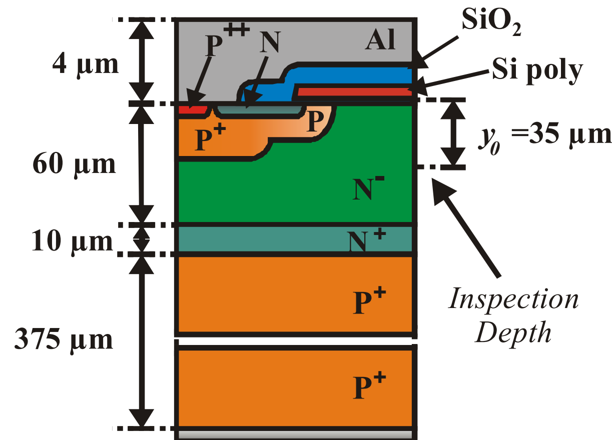

Figure 5.3.1. *Cross-section of the basic half-cell of the 600V PT-IGBT, showing its main parts and dimensions.*

5.3.2 Experimental Conditions

As in the previous chapter, the preparation process required by both studied IGBTs comprises polishing their lateral sides which interact with IR-radiation and soldering them on an insulated metal substrate (IMS). In contrast to the diode stripes, full size IGBTs (5.9×5.9 mm^2) are measured at only one inspection depth, because of the thinner drift region of these IGBTs in comparison to the average value of beam diameter along the interaction length (35 µm). As Figure 5.3.1 shows, the temperature gradient has been measured at y_0=35 µm, thereby avoiding the beam reflections at the top metallization and N$^+$-buffer layer boundary. Performing such measurements is very difficult since a perfect alignment along the optical axis must be assured. Moreover, the device terminations, are not affected by the polishing process, not having surface recombination as in the diodes case. In addition, This fact allows applying relatively high voltages to the devices to obtain high collector currents without influencing on the free-carrier concentration distribution inside the IGBT.

By means of the developed system for DUT excitation, the devices have been switched on and off applying short voltage pulses of 10 V at their control terminal by

means of the excitation circuit described in Chapter 2 (Figure 2.8.2). The pulse duration (t_{on}) ranges from 100 µs to 300 µs in the unirradiated case, and from 50 µs to 400 µs in the other case. By adjusting the voltage source V_{CE}, collector current levels (I_{Con}) ranging from 5 to 15 A are induced during device on-state. In these conditions, the temperature at the PT-IGBT backside is maintained constant, since the generated heat flux has not enough time to reach there. Moreover, these experimental conditions are very favourable to compare experiment and simulation results with analytical model predictions, which will also allow thermal parameter extraction, as demonstrated further on.

5.4 Deflection Signals Simulation

5.4.1 Motivation and Electro-thermal Simulation Conditions

In order to qualitatively understand which are the main contributions to the beam deflection signal, numerical 2-D electro-thermal simulations (ISE-TCAD package [81], DESSIS-ISE) have been performed to assist the experimental investigations. For this purpose, only the unirradiated device has been analysed. As discussed further on, in this device the electro-thermal coupling is produced when measuring the deflection signals, in contrast to the irradiated one (only temperature gradient measurements are available). The test conditions are reproduced for t_{on}= 100 µs and I_{Con} = 10 A. In the chosen experimental conditions, the heat conduction from the top of the device to the IMS substrate (acting as heat-sink) is the predominant cooling mechanism. Moreover, because of the low dissipation energies involved in the tests (short excitation pulses), the temperature at the chip backside is considered isothermal during the simulations.

5.4.2 Electro-thermal Simulation Results

The main simulation results are summarised in Figure 5.4.1 and Figure 5.4.2. Figure 5.4.1 demonstrates that holes concentration profile in steady state increases along the drift region, where y is the depth inside the device (origin at the N^{-}-epitaxy top). Furthermore, their dependence on I_{Con} as dictates the conductivity modulation is also

depicted. This behaviour is also observed for electrons concentration as a consequence of high injection condition, which forces the same concentration values for both carriers. However, these free-carrier concentration profiles can not be exactly measured because of the set-up spatial resolution (beam diameter). As shown further on, an average value of free-carrier concentration is obtained inside the drift region.

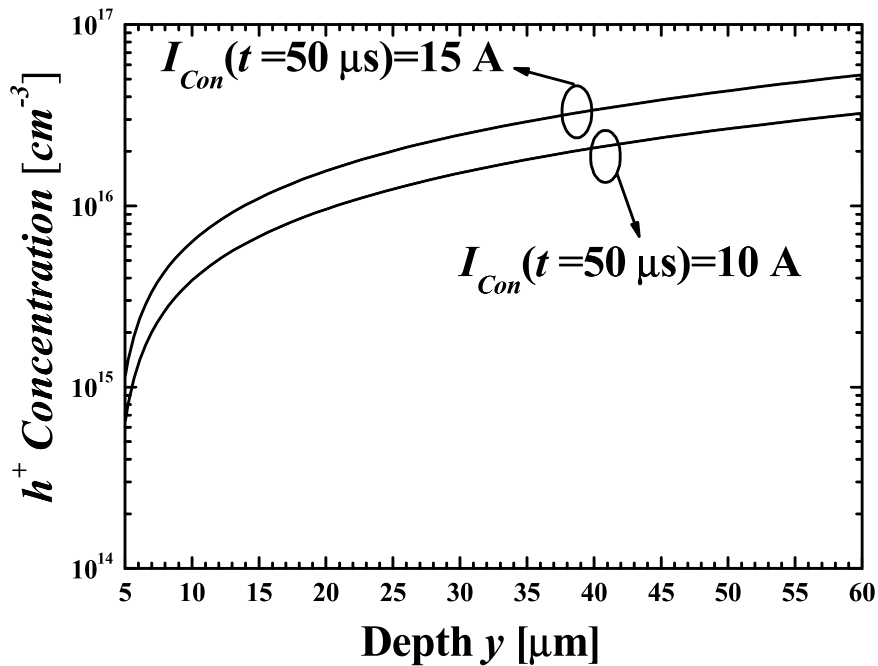

Figure 5.4.1. *Simulated profile of holes concentration corresponding to a cut under the channel.*

Figure 5.4.2 illustrates the evolution of internal temperature obtained from the performed simulation. As observed from this figure, the internal temperature raises during device on-state with a maximum in the channel region (y=0 μm). Moreover, in the P^+-substrate-N^+-buffer junction (y=70 μm, dashed lines), a gradient variation is produced. The curves of Figure 5.4.2 corresponding to t=125 μs and t=150 μs show the cooling process. From these simulation results, temperature gradient dependence on device depth (y) can be observed. This gradient is not constant under short current pulses, as in steady state (see inset of Figure 5.4.2), and it is difficult to extrapolate the absolute temperature from the gradient measured at only one depth within the drift region (y_0=35 μm). For this reason, only measurements of the temperature

gradient can be presented during transient state. In steady state, the reached temperature gradient provides only information on the drift region, since as the inset of Figure 5.4.2 illustrates, two different slopes are found. This fact is mainly related to the location of two heat generation sources inside the device, at the topside (due to contact and N-channel dissipation by Joule effect) and junction defined between the N^+-buffer layer and P^+-substrate, which originate such difference between the observed temperature gradients. Subsequently, since the temperature measurement at the P^+-substrate-N^+-buffer junction is not directly available; the temperature increase referred from the device backside can not be measured. For this reason, only the steady state temperature gradient inside the drift region will be shown. Furthermore, as a first approximation, the main contribution to the generated heat is due to the heat source located at the device topside, since in the junction, a slight temperature variation is observed in Figure 5.4.2.

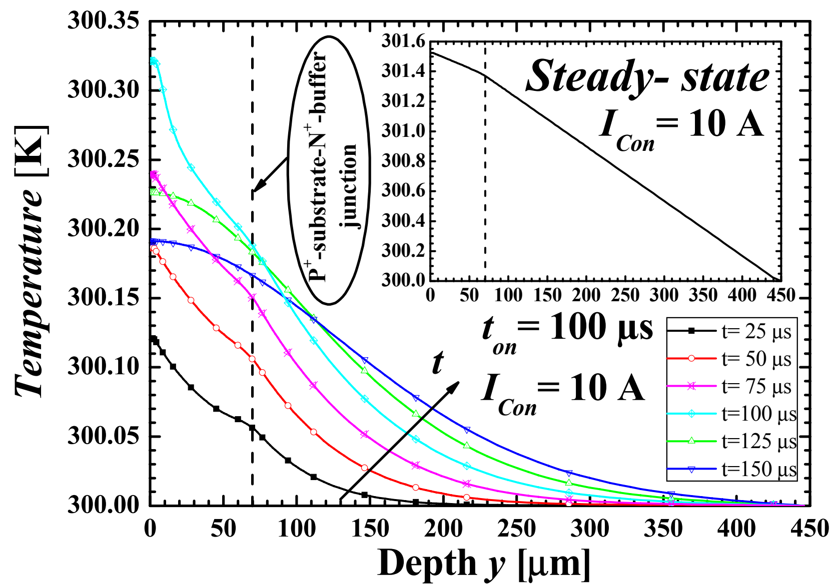

Figure 5.4.2. *Simulated time evolution of vertical temperature distributions in the unirradiated PT-IGBT.*

5.4.3 Expected Deflection Signals

As confirmed from simulation results, temperature and free-carrier concentration only depend on the device depth in the central and deeper part of the drift region because of the chosen experimental thermal conditions and internal device physical behaviour (vertical conduction in the drift region). Therefore, only vertical beam deflections are expected. To infer the beam deflection signal, the refraction index

gradient $\nabla_y n$ in the centre of the drift region is evaluated from simulation results. For this purpose, C and T are taken at two different depths to calculate $\nabla_y C$ and $\nabla_y T$. Finally, the refraction index gradient is evaluated by means of the following equation:

$$\nabla_y n = \left(\frac{\partial n}{\partial C}\right)_T \nabla_y C + \left(\frac{\partial n}{\partial T}\right)_C \nabla_y T \tag{5.4.1}$$

where $(\partial n/\partial T)|_C = 2.0\times10^{-4}$ K^{-1} is taken from the derived value in Chapter 3, and $(\partial n/\partial C)|_T = 3.57\times10^{-21}$ cm^3 is used from the reported result by Soref et al [31], presented in Chapter 2.

Figure 5.4.3 summarises the forward collector current I_C and the time evolution of the three mentioned gradients extracted from simulation results. As shown in these waveforms, I_C is applied at instant t=0 (Figure 5.4.3 (a)). During the conduction time t_{on}, a $\nabla_y C$ is firstly established (Figure 5.4.3 (b)). Then, a $\nabla_y T$ is produced as a result of the heat dissipated on the device top region. As a consequence of these two physical effects (thermal and electrical), a vertical Silicon refraction index gradient $\nabla_y n$ appears. During the conduction state, $\nabla_y C$, $\nabla_y T$, and $\nabla_y n$ show an initial fast variation during the first 4-5 μs. After t=3 μs, the value of $\nabla_y C$ is constant, while $\nabla_y T$ slowly rises in absolute value. The addition of these two tendencies can be observed in the $\nabla_y n$. When the device is turned off, the $\nabla_y n$ reaches its minimum value which corresponds to the maximum of the electrical power losses shown in Figure 5.4.3 (a). Afterwards, n initial value is restored and $\nabla_y n$ returns to zero, due to heat evacuation mechanisms (mainly conduction to the backside IMS substrate). This fact establishes finally the temperature to its equilibrium value.

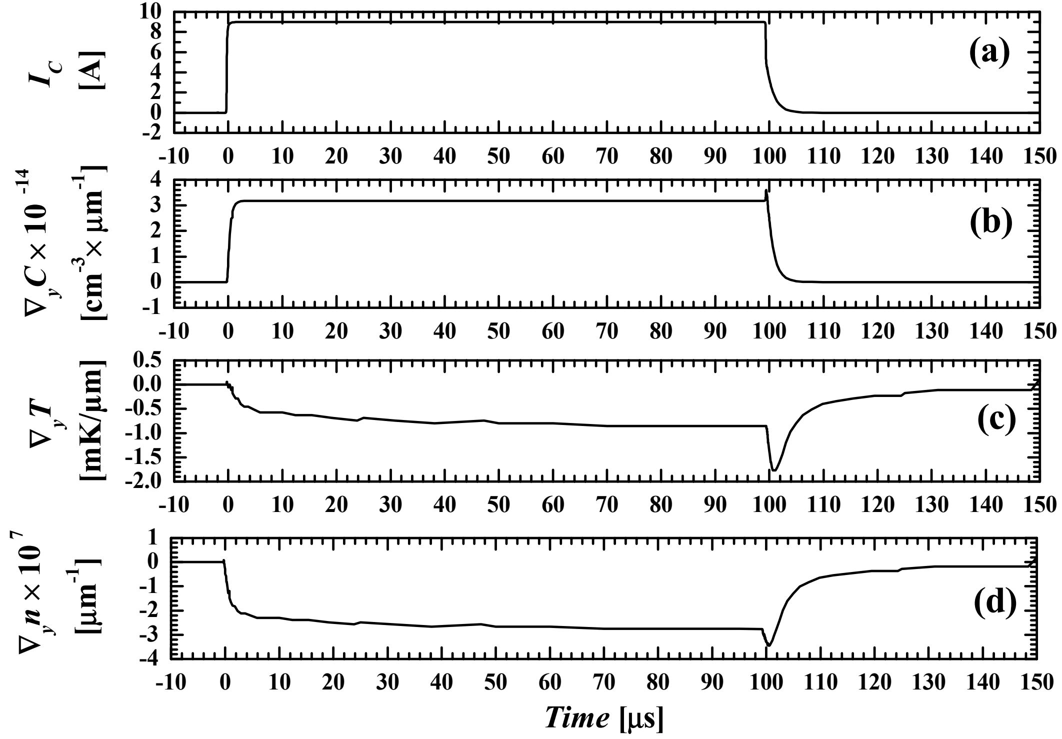

Figure 5.4.3. *Summary of the numerical simulation results for the PT-IGBT (forward collector current pulse I_{Con}=9 A and t_{on}=100 µs): (a) collector current I_C, (b) free-carrier concentration gradient, (c) temperature gradient, (d) refraction index gradient. Gradients evaluated in the drift region using two coordinates y_1=22.5 µm and y_2=47.5 µm.*

5.5 Performed measurements

5.5.1 Bias Waveforms of the Analysed IGBTs

For a better comprehension of the experimental results presented in the next subsections, the typical bias waveforms (V_{CE} and I_C) and dissipated power losses for both devices are shown in Figure 5.5.1 (a) and (b). The dissipated electrical power $P_{dissipated}$ is computed from V_{CE} and I_C waveforms, while dissipated energy $E_{dissipated}$ is deduced by numerical integration of $P_{dissipated}$ during t_{on} (the on-state bias time). In Figure 5.5.1 (a), the maximum power losses in the unirradiated device are produced during the device turn-off process, whereas, in Figure 5.5.1 (b), the main dissipation losses in the irradiated IGBT are produced during the device on-state. This difference

in the electrical behaviour is due to the lifetime local reduction caused by the proton irradiation, increasing on-state voltage drop and diminishing the turn-off time.

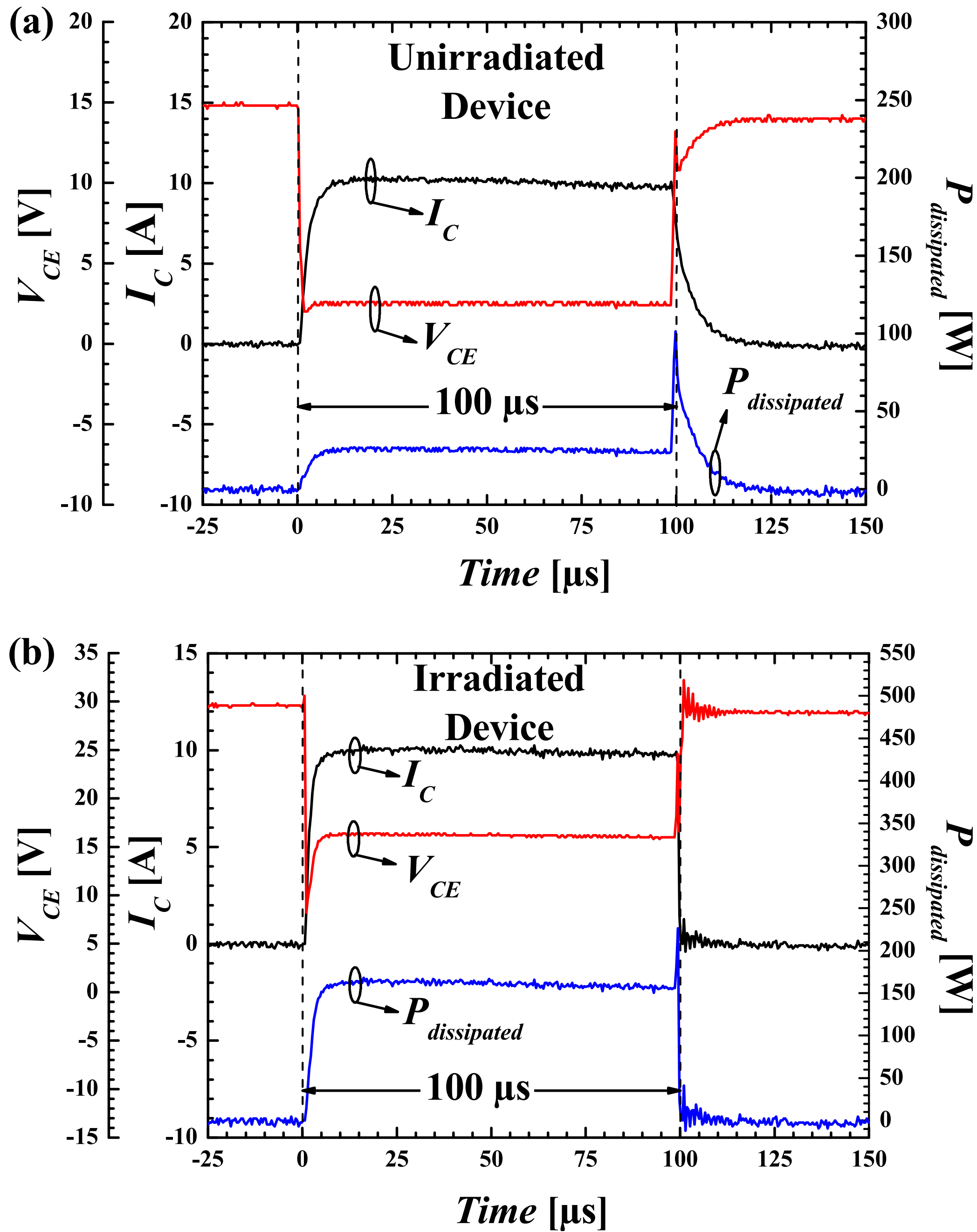

Figure 5.5.1. *Typical waveforms obtained for both biased PT-IGBT (t_{on}=100µs, I_{Con}=10A, V_{GE}=10V): (a) unirradiated, $E_{dissipated}$=2.80 mJ, (b) irradiated, $E_{dissipated}$=15.53 mJ.*

5.5.2 Measured Free-Carriers Evolution in the Drift Region

Figure 5.5.2 depicts the time evolution of C inside the drift region of the unirradiated PT-IGBT at current levels of 5, 10 and 15 A (t_{on}= 100 µs), calculated by using expression (4.3.1). As observed from this figure, C is injected to the device drift region at the device turn-on instant, reaching a constant level during the on-state for each bias current. Once the device is turned-off, the injected free-carriers are removed by recombination and diffusion mechanisms. This effect corresponds to the observed free-carrier concentration decay in Figure 5.5.2. During device on-state, the obtained free-carrier concentrations are higher than the simulated ones (see Figure 5.4.3 (b)). The reason is that C corresponds to an average value inside the drift region, because its thickness (60 µm) is similar to the average value of the spot diameter along the interaction with the device (35 µm). As inferred from Figure 5.5.2, C is linearly related to the current. This fact is a direct consequence of carrier conductivity modulation, by which the drift region resistance is reduced during device on-state.

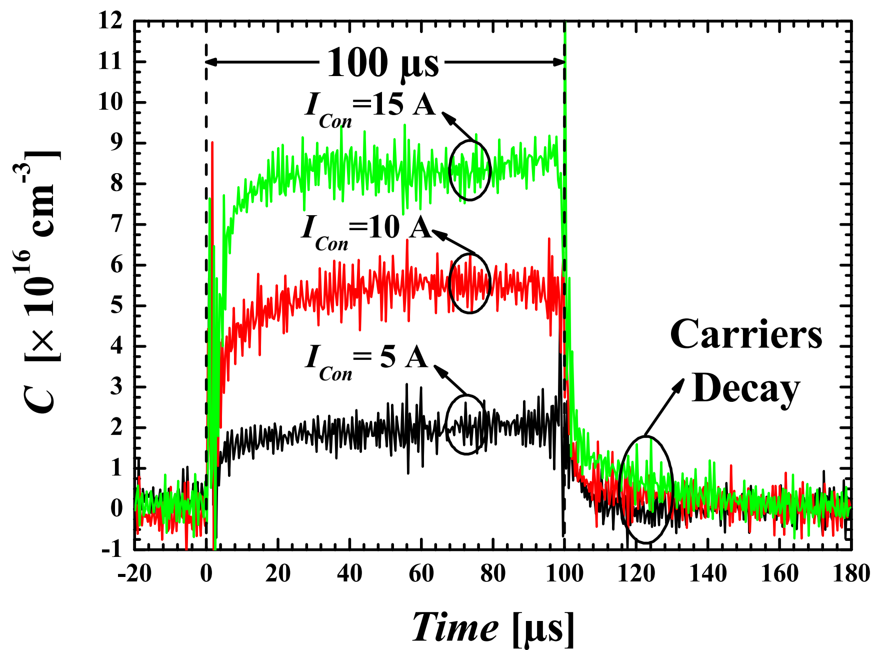

Figure 5.5.2. *Measured free-carrier concentration inside the drift region of the unirradiated PT-IGBT*

The measurement of free-carriers concentration inside the drift region of irradiated PT-IGBT is not possible. This is a direct consequence of the irradiation

process. Due to the fact that defects range is situated inside the drift region, free-carriers rapidly recombine being impossible to produce the conductivity modulation effect. As a result, the irradiated IGBT behaves as a power MOSFET with a high series resistance. Therefore, the high injection condition is not reached and free-carrier concentration measurements are not available.

5.5.3 Temperature Gradient Comparison Depending on I_{Con}

Figure 5.5.3 (a) and (b) represent the measured temperature gradients in the experimental conditions previously explained. The most relevant result is the qualitative coincidence between the experimental waveforms of Figure 5.5.3 (a) and the simulated one of Figure 5.4.3 (c). It is also possible to distinguish that the irradiated PT-IGBT presents a higher temperature gradient during on-state. In addition, $\nabla_y T$ increases with the bias current for both devices. This expected behaviour is a consequence of the increase of Joule power losses with bias current. In the case of the unirradiated PT-IGBT, the value of temperature gradients (at the time instant $t=t_{on}$) ranges from –0.5 to –1.4 mK/µm for a collector current and dissipated energies ranging from 5 to 15 A and 1.05 to 5.35 mJ, respectively. Similar measurements of the irradiated PT-IGBT for two pulse durations (50 µs and 100 µs) provide, for bias currents from 5 to 10 A, the following ranges of results: temperature gradients from –0.5 to –3 mK/µm and dissipated energies from 1.77 to 15.53 mJ. From these results, it can be observed that for similar dissipated energies, the measured temperature gradients are alike independently of the inspected device. The main difference between both devices is the temperature gradient peak (for I_{Con} 10 and 15 A) depicted in Figure 5.5.3 (a) that cannot be resolved in Figure 5.5.3 (b). This is directly related to the observed peak in the turn-off losses represented in Figure 5.5.1 (a), which is associated to the recombination of the stored charge in the drift region of the unirradiated PT-IGBT. This process is extremely fast in the irradiated device (100 ns).

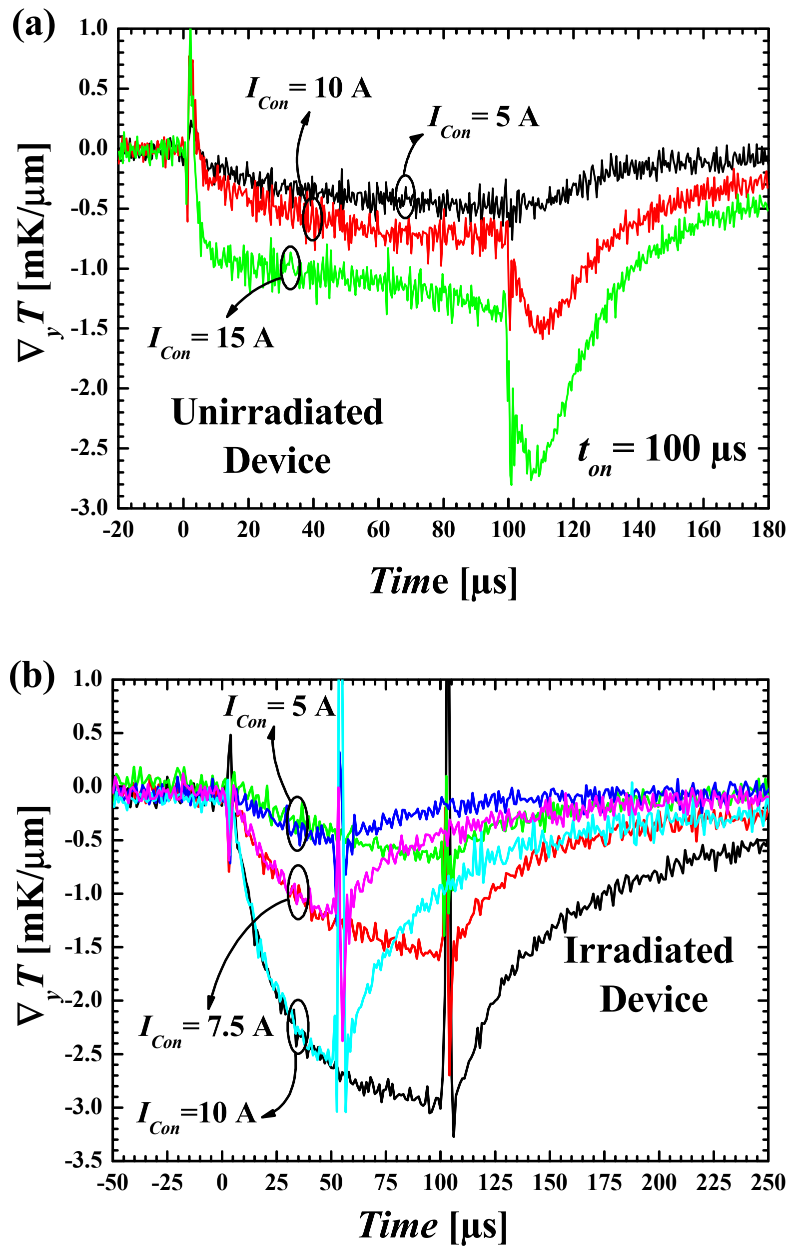

Figure 5.5.3. *Measured temperature gradients in the PT-IGBT drift region* (y_0=35 µm) *for*: (*a*) *unirradiated and* (*b*) *irradiated device.*

5.5.4 Temperature Gradient Comparison Depending on t_{on}

Figure 5.5.4 shows the time evolution of the temperature gradient in the drift region for each PT-IGBT. As in the previous case, a different thermal behaviour has been also obtained. In general, all curves can be divided in two clearly distinguishable

regimes of dissipation corresponding to on-state and turn-off losses inducing the observed evolution of temperature gradients.

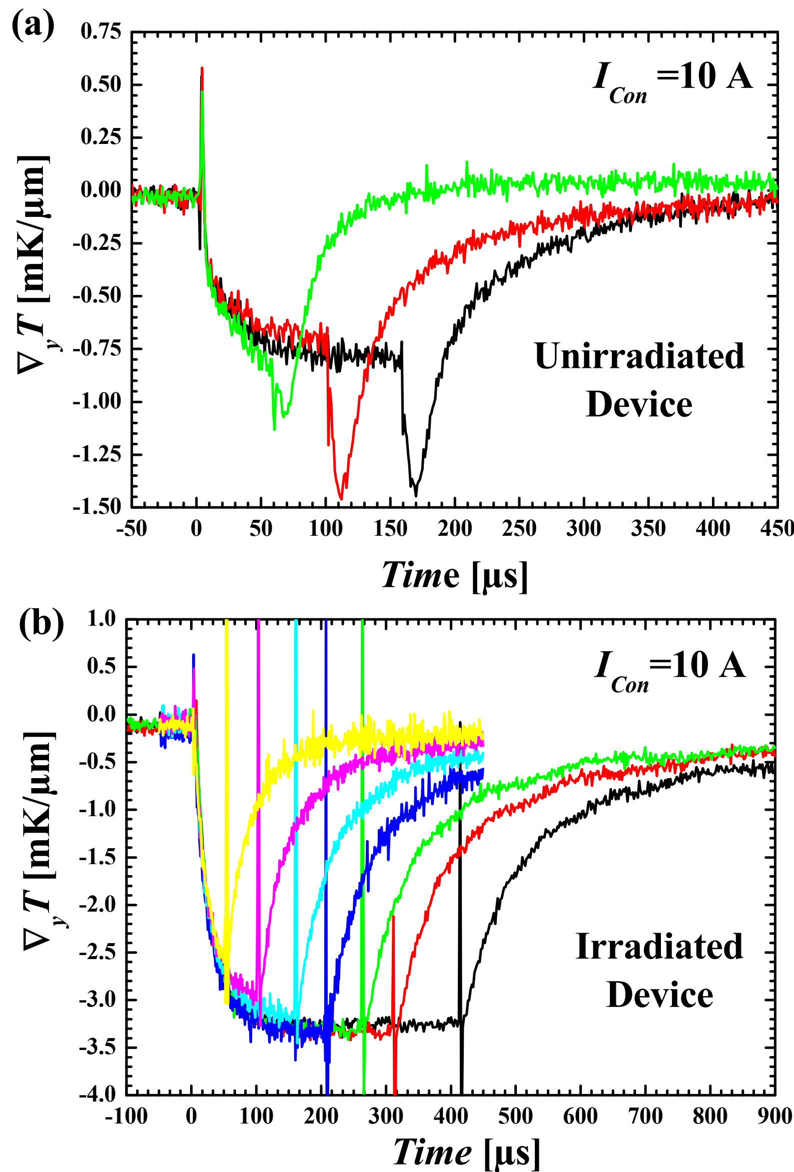

Figure 5.5.4. *Temperature gradient evolution for I_C=10 A and V_{GE}=10V at several t_{on} values, corresponding to:* (*a*) *unirradiated device,* (*b*) *irradiated device.*

The main differences between both thermal behaviours are: higher on-state power losses for the irradiated device, and for the unirradiated one, a power peak related to turn-off process. For the irradiated PT-IGBT, the temperature gradient during on-state reaches –3.3 mK/µm versus –0.8 mK/µm achieved for the unirradiated one. As in the previous subsection, the main difference is in the device behaviour during the

turn-off, where the temperature gradient peak due to turn-off process rises to –1.4 mK/µm. All these experimental values agree with the temperature gradients deduced from the simulations of Figure 5.5.1 for y_0= 35 µm. Moreover, in this figure it can be observed that in all the measurements, the temperature gradient approximately reaches the same level in steady state.

5.5.5 Thermal Parameters Extraction

From all these experimental results, the heat diffusion time and the steady state temperature gradient are determined. As shown in simulation results, the PT-IGBT can be approximated as a semi-infinite slab where all power dissipation is almost produced at the device top. Once heating effects reach the inspection depth (heat conduction), the temperature in the channel region has been uniformly distributed on the device surface, therefore depending only on the device depth. However, this assumption is valid only for t_{on} intervals shorter than the time required for the heat to diffuse from the topside to the backside of the device.

Within these hypotheses, the following expression for the temperature gradient in terms of physical magnitudes is derived [82]:

$$\nabla_y T\,(t_{on}) = -\nabla_y T\,|_0 \left[1 - erf\left(\sqrt{\tau_{heat}/t_{on}}\right)\right] \qquad (5.5.1)$$

where $\nabla_y\ T|_0$ and τ_{heat} correspond to the steady-state temperature gradient and the heat diffusion time, respectively. τ_{heat} is related with the device depth as dictates:

$$\tau_{heat} = y_0^{\,2}/4D_\alpha \qquad (5.5.2)$$

where y_0 and D_α describe the device inspection depth and the thermal diffusivity of Silicon, respectively. Thus, the heat diffusion time is determined by fitting equation (5.5.1) to experimental results. Figure 5.5.5 summarises the obtained results for both devices and the corresponding extracted parameters for I_{Con}=10 A. The fit parameters for each curve are: τ_{heat} = 4.47±0.42 µs, $\nabla_y T|_0$= –0.95±0.2 mK/µm for the unirradiated device; and τ_{heat} = 4.33±0.17 µs, $\nabla_y T|_0$ = –3.90±0.2 mK/µm for the irradiated one. As observed from Figure 5.5.5, experiment is quite well described by

theory, obtaining that both devices present the same τ_{heat}. This is a direct consequence of the fact that the proton irradiation process only changes the device electrical behaviour (introduction of recombination centres) maintaining the same thermal diffusivity. The obtained value of $\nabla_y T|_0$ for the unirradiated IGBT is in good agreement with the steady state thermal simulation of the inset in Figure 5.4.2. Moreover, from the calculated values of τ_{heat}, the thermal diffusivity of Silicon can be estimated using expression (5.5.2). We obtain thermal diffusivity values for the unirradiated and irradiated PT-IGBT of 68.51 mm^2/s and 70.72 mm^2/s, respectively, being in good agreement with the values reported in the literature (89 mm^2/s in [83]). The discrepancy between measured and reported values (less than 15%) is included in the experimental error.

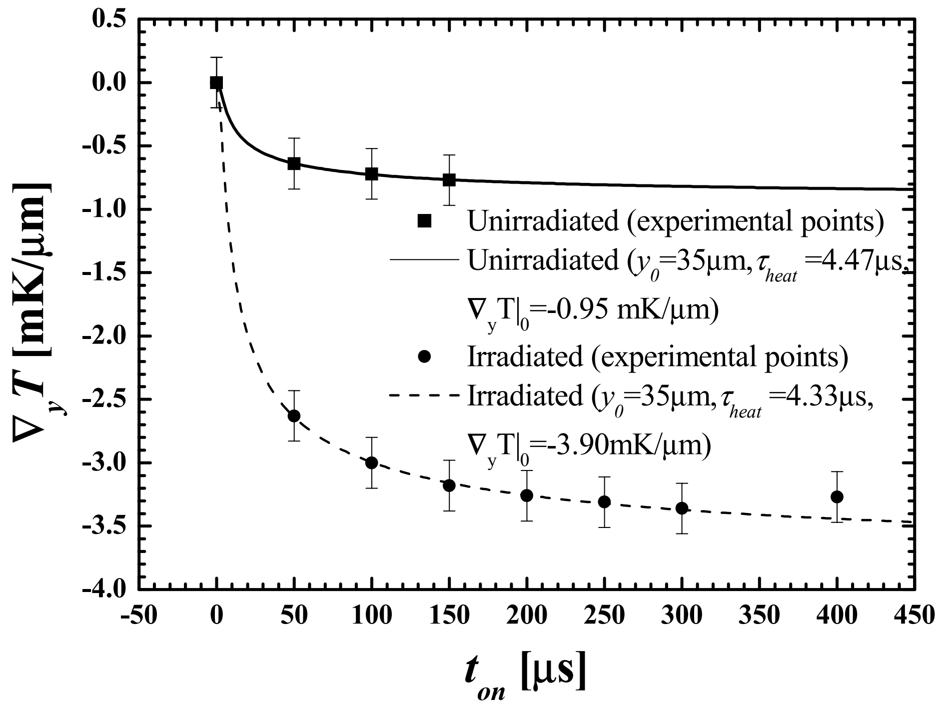

Figure 5.5.5. *Temperature gradient as a function of t_{on} for I_{Con}=10A corresponding to each device. Lines show the corresponding fitting curves, according to expression* (5.5.1).

5.6 Conclusions

In this chapter, 600V PT-IGBT devices (5.9×5.9 mm^2) have been investigated with the developed IIR-LD experimental rig. The only structural modification between the two analysed devices is the introduction of local excess carrier recombination centres in its drift region, which is externally manifested in a very different thermal behaviour between them, allowing the comparison of their temperature gradients inside the drift region. To show the temperature gradient behaviour of both devices, two types of experiment are performed: changing the bias current level and conduction time. In such conditions, the dissipated energy inside both devices is varied. As a result, it has been observed how the temperature gradient only is related to the dissipated energy in each situation. The irradiated device shows higher dissipation losses than the other inspected device, since conductivity modulation is not produced. This fact is deduced from the performed free-carrier concentration measurements, where power radiation absorption is not observed. Consequently, higher dissipation losses are produced during on-state in this device. All this information is extracted with only performing one measurement inside the drift region.

Furthermore, the possibility to extract thermal parameters from both devices is also shown. By using a simple analytical model for temperature gradient, the heat diffusion time and temperature gradient in steady state are derived. It is observed that both devices present the same heat diffusion time, whereas the temperature gradient in steady state is higher in the unirradiated case. These experimental results agree with the expected electro-thermal behaviour which is that the proton irradiation process does not change the thermal diffusivity of Silicon, and that the major dissipation observed in the unirradiated device is due to the free-carrier lifetime control.

General Conclusions

The characterisation of semiconductor devices has an important role in Microelectronics; specially in the case of power semiconductor devices, where the thermo-electrical characterisation is an essential aspect to study their behaviour. In several Power Electronics applications, electro-thermal phenomena have the same relevance as functional and electrical response of such devices. In all of them, the internal self-heating generates an internal temperature rise, changing their nominal electrical parameters. Moreover, this internal temperature increase controls various degradation mechanisms, being an important parameter in device reliability studies. Another parameter which is very important in electro-thermal characterisation of power devices is the internal distribution of free-carrier concentration. For instance, it determines the turn-off time and switching losses of bipolar devices. Although traditional characterisation techniques based on electrical measurements have been used during long time to determine temperature and free-carriers values, their main disadvantage is that they obtain an average value of the measured parameter over all the device. However, in some cases, such as the calibration of electro-thermal predictive simulations, a higher spatial resolution is required. Consequently, different spatially resolved techniques have appeared during the last 30 years. Among them the most versatile are the methods based on laser probe beam which longitudinally passes through the device. Apart from the laser radiation power, the electro-thermal sensitive properties of the probe beam are basically its radiation phase and trajectory deflection. These phenomena are due to the modulation of refractive index and absorption coefficient by free-carriers concentration (plasma-optical effect) and temperature (thermo-optical effect). Depending on the used electro-thermal sensitive parameter, these techniques are categorised in interferometric methods (radiation

phase shift) and internal IR-laser deflection (IIR-LD). In IIR-LD, the physical mechanisms which are involved in the beam deflection are the gradients of free-carrier concentration and temperature, inducing a refractive index gradient. Moreover, as the free-carrier concentration can be determined from power radiation absorption measurements, the IIR-LD equipment can be easily adapted for performing free-carrier absorption (FCA) tests. Subsequently, temperature gradients and free-carrier concentration are simultaneously determined.

In this framework, an experimental rig based on the IIR-LD technique has been designed to test biased power devices. The developed equipment allows measurements of internal temperature distributions, being a complementary tool of the IR-thermography system available at CNM. Although the IIR-LD method is not presented for the first time, this work describes how to optimally design this kind of optical equipment by means of very simple expressions and principles. As far as we know, in Europe only another equipment of these characteristics exists currently.

The IIR-LD experimental rig can be divided in three main set-ups: optical, mechanical, and electrical. The optical set-up is formed by an IR-laser source (λ=1.3 μm) and an optical system (two lenses and a beam collimator). By means of the optical system, the beam diameter across the device under test (DUT) is controlled. This fact is an important issue, because the spatial resolution depends on the beam spot dimensions. In this work, the beam shape along the interaction with the DUT has been optimised for typical DUT lengths, achieving a spatial error of 11 μm for 5 mm devices.

The mechanical set-up is constituted by six displacement modules, allowing the displacement for the collimator, each lens, DUT, and sensor. Each displacement module consists of different micro-positioning stages and adapting pieces, which assure a spatial error lower than the introduced one by the probe beam (±7 μm in the worst case). All the displacement modules are supported on an optical breadboard to isolate the experimental rig from environmental mechanical vibrations.

The electrical set-up consists of the radiation power and deflection sensing system, the DUT excitation system, and the acquiring signal equipment. The

radiation power and deflection sensing system is formed by a four-quadrant photodiode sensor (FQP), I/V converter (FQP preamplifier), and post-processing signal circuit. Concretely, the post-processing signal circuit implements real-time arithmetical operations among the signals incoming from the FQP. The power and deflection sensing system has been designed and optimised to obtain a high resolution in radiation power measurements, position sensing, and time. Electronically, these requirements can be interpreted as a constraint on the noise level (deflection and radiation power resolution) and bandwidth (time resolution). For a 2 mW radiation working power, the noise level of deflection signals is 14 mVrms, while the radiation power one is 3.5 mVrms. This fact provides a spatial and radiation power resolution of 2 µm and 12 µW, respectively. Concerning the system bandwidth, a 1.4 MHz is obtained approximately providing a 350 ns time resolution, which is required to resolve free-carriers concentration evolution. To the best of our knowledge, post processing circuits with such a wide bandwidth and a low noise figure are not commercially available (we have found a maximum bandwidth of 25 KHz). In our opinion, the proposed circuit could be of major interest in scientific applications requiring fast photo-detection performances, such as the IIR-LD technique.

As for the DUT excitation system, a modified Buck converter has been implemented to bias the DUT with short current pulses. This system can be divided in three functional sub-circuits: the Buck converter, MOS-gated drive circuit, and synchronisation and control unit (SCU). The Buck converter is the main sub-circuit where all passive components and power devices are connected. The MOS-gated drive circuit controls the state of MOS-gated power devices. The SCU manages the activation or deactivation of both drivers, as well as their synchronisation. All these actions are performed from an external control signal $V_{generator}$ provided by a waveform generator.

Concerning the acquiring equipment, an A6312 Tektronix Hall Effect current probe (with a bandwidth of 100 MHz), along with its AM 503B Tektronix amplifier, and a TDS 744A four channel digitizing oscilloscope perform the measurement of

the biasing current and all output signals of the sensing system, respectively.

In this work, the set of equations relating the measured signals to temperature gradients and free-carriers concentration are also derived (see Appendix A). In addition, it is also argued that the refractive index and absorption coefficient are linearly related to temperature and free-carriers concentration, as further discussed in Chapter 2. Therefore, the first step towards any measurement is the determination of the proportionality factors relating the refractive index and absorption coefficient to free-carrier concentration and temperature. Consequently, a research in the literature resources has been performed for the experimental conditions of this work ($\lambda = 1.3\mu m$). However, discrepancies were found among the reported values in the case of the refractive index dependence on temperature $(\partial n/\partial T)_C$. Subsequently, a thermal calibration procedure for the IIR-LD equipment has been carried out. The method is based on a thermal test chip (TTC), whose behaviour is well described by an analytical thermal model. The benefits of this procedure are that the fabrication of a TTC is much easier and straightforward than an active device, such as a power MOSFET, because of its structural simplicity. Basically, the TTC structure is a Silicon substrate with a heating resistor on its top, designed to facilitate the measurement of vertical temperature distributions. During short heating times (250 μs), the temperature distribution is estimated by using different reported values for the coefficient $(\partial n/\partial T)_C$, and compared with the TTC thermal model. As a result, for temperature rise ranging from 0 to 1.4 K, a discrepancy of the value less than 17% between theory and experiment is obtained in the worst case selecting $(\partial n/\partial T)_C = 2.0\times10^{-4}\ K^{-1}$. A high time resolution has been also evidenced, allowing the temperature evolution measurement even for very short excitation times (25 μs).

To show the functionality of the developed experimental rig for power devices characterisation, power diodes and PT-IGBTs are used for demonstrating the equipment performances in free-carriers concentration and temperature gradient measurements, respectively. This demonstration has been performed in each case by the comparison between irradiated and unirradiated devices. Ion or proton irradiation technique belongs to lifetime killing methods used to improve the bipolar device

response during turn-off process. With this process, the devices electro-thermal behaviour is changed maintaining its layout structure.

In power diodes measurements, the modification of the free-carrier concentration in steady state, jointly with the carriers decay time, by ion irradiation process have been determined. Such measurements have been performed biasing the diode at low current density levels (up to 11 A/cm^2) during short times (84 µs) to avoid the parasitic effects of the high contact resistance introduced when the sample is housed in an IMS substrate. Moreover, due to the heating effects associated to this resistance, internal temperature increments purely due to device physics can not be measured. For this reason, further efforts must be directed towards packaging improvement of this type of samples prior to proceed to the internal temperature measurement. The validation of the experimental results, obtained from the absorption signal, has been mainly justified due to their very good agreement with the electrical simulations of the diodes. From the measurements, internal effects of the ion irradiation processes such as the local modification of free-carrier concentration distribution or local lifetime dependence are directly evidenced.

For unirradiated and irradiated PT-IGBTs, two types of experiments are performed to show the temperature gradient behaviour of both devices: changing the bias current level and conduction time. In such conditions, the dissipated energy inside both devices is varied. As a result, it has been observed how the temperature gradient is only related to the dissipated energy in each situation. The irradiated device shows higher dissipation losses than the other inspected device, since modulation conductivity is not produced. This fact is deduced from the performed free-carrier concentration measurements, where power radiation absorption is not observed. Consequently, higher dissipation losses are produced during on-state in this device. All this information is extracted with performing only one measurement inside the drift region because of the similarity in dimensions of the drift region and laser beam diameter. From these measurements, the heat diffusion time and temperature gradient in steady state are derived by fitting a simple analytical model to the experimental results. It is observed that both devices present the same heat

diffusion time, whereas the temperature gradient in steady state is higher in the unirradiated case. Moreover, these results give evidence for the versatility of the proposed measurement system for obtaining direct values of semiconductor thermal parameters that could be used in simulation works. This fact also reveals that the major dissipation observed in the unirradiated device is due to the free-carrier lifetime control, as expected. On the other hand, electro-thermal simulations of the measured devices quantitatively agree with experiment. In particular, the simulated waveforms of temperature gradient and free-carriers concentration have shown the same behaviour as the experimental ones, deduced from the absorption and deflection signals.

Concerning the future lines, aside from IIR-LD and FCA measurements, this experimental rig can also be used for temperature determination by means of interferometry techniques (Fabry-Perot), directly providing temperature measurements inside the DUT. This is an important issue, since temperature measurements could be performed inside 600 V PT-IGBTs at only one depth. This fact can reveal interesting information to derive the internal temperature from experimental results. With this technique, it is possible to measure very high temperature values impossible to determine by IIR-LD due to an excessive probe beam deflection above 300 K. This technique will be very useful for studying IGBTs working in short circuit operation, where these devices experience localised high temperature increase (more than 100 K). From the experience and knowledge acquired in Silicon devices measurements, an immediate objective is extending such kind of measurements to power devices made of new emerging materials for power electronics applications, such as SiC and GaN. These materials improve several electro-thermal characteristics of power devices, e. g., the dependence of nominal electrical parameters on temperature. Towards this direction, the thermal calibration method based on a TTC can be used in such materials, also allowing the study of their optical properties for applications in other fields.

APPENDIX A

DERIVATION OF C AND $\nabla_y T$

A.1 Introduction

In this appendix, all the expressions related to the developed set-up are inferred. Figure A.1.1 shows a laser beam that passes through a diode (DUT) experiencing a deflection and power transmission modulation at the incidence depth y_0. Two lenses L_1 and L_2 are also depicted, along with the corresponding distances between L_1-lens and DUT (d_1), DUT and L_2-lens (d_2), and L_2-lens and detector (d_3). At the end of all these elements, the four quadrant detector is situated. This element must be able to measure the transmitted power across the biased DUT. The distance $H(y_0, t)$ is directly related to the total beam deflection $\Delta y(z=L, y_0, t)$.

As observed in Figure A.1.1, the laser perpendicularly strikes on the DUT lateral side ($\theta_i=\pi/2$). Because of the thermo- and plasma-optical effects, a small variation on the refractive index $\delta n(y_0, t)$ is produced when a current flows through the device, introducing a small angular variation in the beam propagation direction. In this situation, the higher the interaction distance is, the higher the beam deviation will be. For this reason, a total angular deviation of the beam θ (point 2, interface Silicon-air) is finally obtained. When the beam changes of medium, it is refracted (according to Snell law) and its angular deviation becomes θ_{air}. In this notation, the dependence on y_0 and t symbolically denotes the relation of the given variable to the incidence point and time, respectively. Thereby, the expressions which will be derived are valid

around the incident depth y_0. Therefore, in order to obtain the gradients in the vertical position, a scanning in depth must be applied, without changing the y-z plane. The collection of the measured data at various depths is denoted by changing y_0 by y. Thus, the profiles of the aforementioned gradients are finally determined.

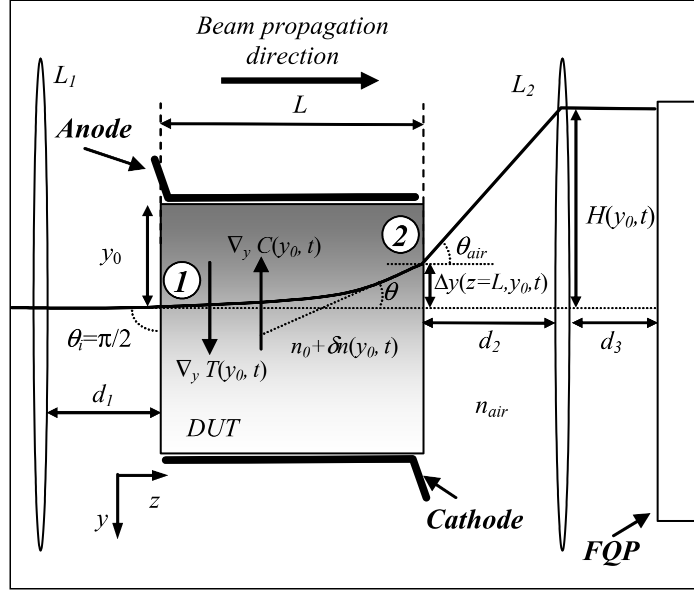

Figure A.1.1. *View of IIR-LD involved phenomena, showing the main parameters used for the final expression.*

A.2 Free-carrier Concentration Expression

The radiation power absorbed by the free-carriers along the beam trajectory inside the DUT at a given depth y_0 is given by [84]:

$$\frac{P(t)}{P_{off}} = \exp\left(-\int_0^L dz\,\alpha(C(y_0, z))\right) \tag{A.1.1}$$

assuming that radiation absorption is constant inside the DUT, the following expression is derived:

$$\alpha(C(y_0, t)) = \frac{1}{L} Ln\left(\frac{P_{off}}{P(t)}\right) \tag{A.1.2}$$

where P_{off} is the radiation power on the detector surface prior to device excitation and $P(t)$ denotes the evolution of the radiation power on the detector. Equation (A.1.2) may be expressed as:

$$\alpha(C(y_0,t)) = \frac{1}{L} Ln\left(\frac{V_{out,P_0}}{V_{out,P}}\right) \quad \text{(A.1.3)}$$

where $V_{out,P0}$ and $V_{out,P}$ correspond to the signals derived from P_{off} and $P(t)$, respectively. α has basically two components, one related to the injected free-carriers, and the other one related to the absorption performed by the doping level free-carriers ($C(y_0, t)|_{dop}$). This fact is expressed as follows:

$$\alpha = \left(\frac{\partial \alpha}{\partial C}\right)_T \left(C(y_0,t) - C(y_0,t)|_{dop}\right) \quad \text{(A.1.4)}$$

Since the inspected zone always is the drift region of bipolar devices, the following approximation is possible as long as during the conduction regime the high injection condition is accomplished:

$$\alpha \approx \left(\frac{\partial \alpha}{\partial C}\right)_T C(y_0,t) \quad \text{(A.1.5)}$$

By substituting Equation (A.2.5) into (A.2.3) and isolating $C(y_0, t)$, the desired expression for $C(y_0, t)$ is obtained:

$$\boxed{C(y_0,t) = \frac{1}{L\left(\frac{\partial \alpha}{\partial C}\right)_T} Ln\left(\frac{V_{out,P_0}}{V_{out,P}}\right)} \quad \text{(A.1.6)}$$

A.3 Refractive Index Gradient Derivation

As a first step, an expression for $\Delta y(z=L, y_0, t)$ depending on d_2, L, $H(y_0,t)$, n and n_{air} is aimed. The analysis starts at the beam output face 2 (see Figure A.1.1). In the change of medium, *Snell*'s law is applied, and $\sin\theta$ and $\sin\theta_{air}$ are expressed as a function of the total deflection experienced inside the chip $\Delta y(z=L, y_0, t)$, the chip longitude L and the beam spot displacement on the FQP $H(y_0, t)$:

$$(n_0+\delta n(y_0, t))\,\mathrm{Sin}\theta = n_{air}\,\mathrm{Sin}\theta_{air} \tag{A.2.1}$$

$$Sin\theta = \frac{\dfrac{\Delta y(z=L, y_0, t)}{L}}{\sqrt{\left(\dfrac{\Delta y(z=L, y_0, t)}{L}\right)^2 + 1}} \tag{A.2.2}$$

$$Sin\theta_{air} = \frac{\dfrac{H(y_0,t)-\Delta y(z=L, y_0, t)}{d_2}}{\sqrt{\left(\dfrac{H(y_0,t)-\Delta y(z=L, y_0, t)}{d_2}\right)^2 + 1}} \tag{A.2.3}$$

Afterwards, the paraxial approximation in the sinus, namely, $\frac{\Delta y(z=L, y_0, t)}{L} \ll 1$ and $\frac{H(y_0,t)-\Delta y(z=L, y_0, t)}{d_2} \ll 1$ is obtained:

$$Sin\theta \approx \frac{\Delta y(z=L, y_0, t)}{L} \tag{A.2.4}$$

$$Sin\theta_{aire} \approx \frac{H(y_0,t)-\Delta y(z=L, y_0, t)}{d_2} \tag{A.2.5}$$

by substituting (A.2.4) and (A.2.5) into (A.2.1) the following expression is reached:

$$\frac{n_0}{n_{air}} \approx \frac{(H(y_0,t) - \Delta y(z=L, y_0,t))L}{\Delta y(z=L, y_0,t) d_2} \tag{A.2.6}$$

where $\delta n(y_0, t) << n_0$ is assumed. Finally, deriving:

$$\Delta y(z=L, y_0,t) \approx \frac{H(y_0,t)}{1+\dfrac{n_0 d_2}{L n_{air}}} \tag{A.2.7}$$

where $H(y_0, t)$ corresponds to the spot deviation determined by the detector, L is the longitude of the chip, n_0 and n_{air} are the refractive indexes of Silicon and air, respectively.

In order to obtain the index gradient depending on the distance d_2, $H(y_0, t)$, n and n_{air}, the differential equation corresponding to the trajectory of a ray propagating inside a medium with a stratified medium is considered [85]:

$$\frac{dy}{dz} \approx \sqrt{\left(\frac{n(y)}{n_0}\right)^2 - 1} \tag{A.2.8}$$

When Equation (A.2.8) is evaluated at the output face (point 2 of Figure A.1.1) with the hypothesis that the deflections are small and the beam is not excessively deviated from y_0, the following solution is found:

$$\left.\frac{dy}{dz}\right|_{z=L} \approx \left.\frac{\Delta y}{\Delta z}\right|_{z=L} = \frac{\Delta y(z=L, y_0,t)}{L} \tag{A.2.9}$$

and, thus:

$$\frac{\Delta y(z=L, y_0, t)}{L} \approx \sqrt{\left(\frac{n(y_0, t)}{n_0}\right)^2 - 1} \qquad \text{(A.2.10)}$$

By isolating $n(y_0, t)$ from expression (A.2.10), the following relation is inferred:

$$n(y_0, t) = n_0 \sqrt{1 + \left(\frac{\Delta y(z=L, y_0, t)}{L}\right)^2} \qquad \text{(A.2.11)}$$

and taking into account the paraxial approximation $\frac{\Delta y(z=L, y_0, t)}{L} << 1$, (A.2.11) results in:

$$n(y_0, t) \approx n_0 \left[1 + \frac{1}{2}\left(\frac{\Delta y(z=L, y_0, t)}{L}\right)^2\right] \qquad \text{(A.2.12).}$$

Finally, by applying the gradient operator respect to the axis y, the following result is reached:

$$\nabla_y \, n(y_0, t) = n_0 \frac{\Delta y(z=L, y_0, t)}{L^2} \qquad \text{(A.2.13)}$$

by substituting (A.2.7) in (A.2.13) and evaluating $n_{air}=1$, the aimed expression is derived:

$$\nabla_y \, n(y_0, t) = \frac{H(y_0, t)}{L\left(\frac{L}{n_0} + d_2\right)} \qquad \text{(A.2.14)}$$

which corresponds to the refractive index gradient determined at y_0. After that, (A.2.14) is evaluated for a given distance d_2 such that f_{L_2} is in the middle of the DUT according to the Abbe invariant:

$$d_2 = f_{L_2} - \frac{L}{2n_0} \tag{A.2.15}$$

Assuming a linear response of the detection system with spot displacement, $H(y_0, t)$ is written as:

$$H(y_0, t) = \frac{\phi_{L_2}}{2} \frac{V_{out,y}(y_0, t)}{\kappa'} \tag{A.2.16}$$

where ϕ_{L_2} is the beam diameter on the L_2-lens surface. As the deflections are small, the beam spot onto the FQP ϕ_{FQP} will be the same as onto the L_2-lens. By substituting (A.2.15) and (A.2.16) in (A.2.14), the final equation where $\nabla_y n$ is related to the gradients of free-carrier concentration and temperature is obtained:

$$\boxed{\nabla_y n\,(y_0, t) = \frac{NA \;\; V_{out,y}(y_0, t)}{\kappa' L \left(\frac{L}{2 f_{L_2} n_0} + 1 \right)}} \tag{A.2.17}$$

where equation (A.2.14) is expressed in terms of design and measurements parameters: the focal distance of the L_2 lens (f_{L_2}), the beam numerical aperture (NA), the proporcionality factor between spot displacement on the detector and the obtained deflection signal (κ'), and the deflection signal ($V_{out,y}$). NA is defined as the following expression shows:

$$NA = \frac{\phi_{L_2}}{2 f_{L_2}} \tag{A.2.18}$$

This parameter is an optical invariant used to characterise the beam shape, constituting one of the design parameters as explained in Chapter 2 section 2.5.2.

A.4 Decoupling $\nabla_y C\ (y, t)$ and $\nabla_y T\ (y, t)$ from $\nabla_y n\ (y, t)$

The vertical distribution of the refractive index gradient $\nabla_y n\ (y, t)$ is determined when several depths are inspected. Thus, once the free-carrier concentration is known, the experimental data is numerically differentiated respect y obtaining $\nabla_y C\ (y, t)|_{\mathrm{num}}$. As $\nabla_y n$ has two components:

$$\nabla_y n\,(y_0, t) = \left(\frac{\partial n}{\partial C}\right)_T \nabla_y C\,(y_0, t) + \left(\frac{\partial n}{\partial T}\right)_C \nabla_y T\,(y_0, t) \qquad \text{(A.3.1)}$$

the decoupling of both effects on $\nabla_y n$ can be performed as follows:

$$\boxed{\nabla_y T(y,t) = \frac{\nabla_y n(y,t) - \left(\dfrac{\partial n_{Si}}{\partial C}\right)_T \nabla_y C(y,t)\Big|_{num}}{\left(\dfrac{\partial n_{Si}}{\partial T}\right)_C}} \qquad \text{(A.3.2)}$$

LIST OF SYMBOLS

α	Absorption coefficient.
α_X	Rotation around the *X* axis performed with a micro-positioning stages.
α_Y	Rotation around the *Y* axis performed with a micro-positioning stages.
α_Z	Rotation around the *Z* axis performed with a micro-positioning stages.
β	Incidence angle.
β'	Refractive angle.
$\delta n\ (y_0, t)$	Evolution of a small variation of refractive index at the inspected depth y_0.
$\left(\frac{\partial n}{\partial C}\right)_T$	Plasma-optical coefficient referred to the refractive index.
$\left(\frac{\partial n}{\partial T}\right)_C$	Thermo-optical coefficient referred to the refractive index.
$\left(\frac{\partial \alpha}{\partial C}\right)$	Thermo-optical coefficient referred to the absorption coefficient.
$\left(\frac{\partial \alpha}{\partial T}\right)_C$	Plasma-optical coefficient referred to the absorption coefficient.
ΔC	Free-carrier concentration variation.
ΔP	Uncertainty in power sensing.

ΔT	Temperature increase.
Δx	Uncertainty in the beam spot displacement sensing along the direction x.
Δy	Uncertainty in the beam spot displacement sensing along the direction y.
$\Delta y\ (z=L,y_0,t)$	Total deflection experienced by the probe beam inside the DUT.
$\nabla_y n\ (y_0, t)$	Time evolution of the refractive index at a given depth y_0.
$\nabla_y n\ (y, t)$	Time evolution of the distribution of refractive index gradient inside the DUT.
$\nabla_y C\ (y_0 , t)$	Measured time evolution of the free-carrier concentration gradient at a given depth y_0.
$\nabla_y C\ (y , t)$	Measured time evolution of the free-carrier concentration gradient inside the DUT.
$\nabla_y C(y,t)\big\vert_{num}$	Free-carrier concentration gradient numerically calculated from C.
$\nabla_y T\ (y_0, t)$	Time evolution of the temperature gradient inside the DUT at the inspection depth y_0.
$\nabla_y T\ (y, t)$	Time evolution of the distribution of temperature gradient inside the DUT.
ε_0	Permitivity of free space.
ϕ	Probe beam diameter.
ϕ_{L_2}	Beam diameter on the L_2-lens surface.
ϕ_{FQP}	Beam diameter on the FQP surface.
$\phi_{FQP,\max}$	Maximum beam diameter on the FQP surface.
κ	Detector response along its operation linear region.
κ'	Proportionality factor relating the deflection signal to the spot displacement ($\kappa' := \kappa \times A_{v0,2}$).

λ	Wavelength of the working laser radiation.
λ_0	Radiation wavelenght in the free space.
$\mu_{n,p}$	Mobility of electrons or holes.
θ	Total angular deviation of the laser probe beam inside the DUT.
θ_{air}	Total angular deviation of the probe outside the DUT.
θ_i	Angle of incidence defined between the beam and DUT lateral side.
$\sigma_{n,p}$	Trap capture cross section for electrons or holes.
$\sigma_{position}$	FQP theoretical resolution in spot displacement determination.
σ_{Pw}	Resolution in power sensing.
σ_x	Resolution in horizontal deflection (x direction).
σ_y	Resolution in vertical deflections (y direction).
τ_{dec}	Exponential time constant which is fitted to the free-carrier concentration decay.
τ_{heat}	Heat time diffusivity.
$\tau_{n,p}$	Minority carrier lifetime of electrons or holes.
τ_{SRH}	Carriers lifetime due to bulk SRH recombination.
$A_{v0,1}$	Signal gain introduced at the output of the first stage of the post-processing signal circuit.
$A_{v0,2}$	Signal gain introduced at the output of the second stage of the post-processing signal circuit.
$BW_{@-0.1\ dB}$	Bandwidth of the post-processing circuit when the gain response has decreased 0.1 dB.
$C\ (y_0,\ t)$	Time evolution of free-carriers concentration measured at an inspection depth y_0.

C_{CQJ}	Capacitor at the output of the trim circuit corresponding to J^{th} quadrant of the FQP.
$C_{n,p}$	Free-electrons and -holes concentration.
$C_{n,max}$	Free-electrons concentration at the PN-junction (used in Chapter 4).
C_{SS}	Measured free-carriers concentration in steady state.
d_1	Relative distance between the L_1-Lent and DUT.
d_2	Relative distance between the DUT and L_2-Lens.
d_3	Relative distance between the L_2-Lens and FQP.
D_α	Thermal diffusivity of Silicon.
$E_{dissipated}$	Electrical energy dissipated within an IGBT
E_T	Trap energy level (deep-level energy).
f_{L_1}	Focal distance of L_1-Lens.
f_{L_2}	Focal distance of L_2-Lens.
g	Distance among each photoquadrants of a FQP (FQP gap).
$H(y_0, t)$	Vertical displacement of the probe beam on the surface of L_2-Lens.
$I(r,z)$	Radiation intensity of a laser beam.
I_C	IGBT bias current.
I_{Con}	IGBT bias current in steady state during conduction mode.
I_{Q1}	Current photogenerated at the quadrant Q_1.
I_{Q2}	Current photogenerated at the quadrant Q_2.
I_{Q3}	Current photogenerated at the quadrant Q_3.
I_{Q4}	Current photogenerated at the quadrant Q_4.
L	Interaction length between the probe beam and the DUT.

L_{ef}	Effective length of the interaction between a laser beam and a material with a refractive index *n* (*L*/*n*).
L_1	Beam focussing lens in the middle of the DUT.
L_2	Lens located at the beam output of the DUT.
$m^*_{n,p}$	Effective mass of electrons or holes.
NA	Beam numerical aperture.
$NA\|_{opt}$	Beam numerical aperture optimised for increasing the spatial resolution during the measurements.
n_{air}	Refractive index of air (=1).
$n\ (C, T)$	Refractive index of Silicon as a funcion of free-carrier concentration and temperatura.
n_0	Refractive index of Silicon at room temperature and λ= 1.3 µm (=3.5).
N_T	Traps concentration of for a given energy deep-level.
$P(t)$	Time evolution of the radiation power detected with the FQP.
P_0	Dissipated power on the TTC topside surface in steady state.
$P_{dissipated}$	Electrical power dissipated within an IGBT.
P_{off}	Radiation power detected when the DUT is not biased.
P_{on}	Radiation power detected while the device is biased.
q	Electron charge.
Q_1	Quadrant located at the right superior part on the FQP surface respect to the incidence point.
Q_2	Quadrant located at the left superior part on the FQP surface respect to the incidence point.
Q_3	Quadrant located at the right inferior part on the FQP surface respect to the incidence point.

Q_4	Quadrant located at the left inferior part on the FQP surface respect to the incidence point.
R_{CQJ}	Variable resistor of the trim circuit.
Re	Responsivity of the FQP.
$R_{in,k}$	k^{th} input resistor of an analogical adder.
R_S	Resistor of the non-inverting op amp input.
R_F	Op amp feedback resistor.
S	Quadrant radius of a FQP.
S_{SRH}	Carriers surface recombination velocity due to SRH mechanism.
T	Temperature.
t	Time.
t_{on}	Conduction time of the studied device. This time is also used to denote the heating time in Chapter 3.
v_c	Velocity of light.
$v_{th,n}$	Thermal velocity of electrons.
$v_{th,p}$	Thermal velocity of holes.
V_{CQJ}	Compensation voltage obtained from the trim circuit corresponding to J^{th} quadrant of the FQP.
V_{CE}	Voltage drop between terminals collector and emitter of an IGBT.
V_{GE}	Voltage drop between terminals gate and emitter of an IGBT.
$V_{out,inv}$	Output voltage of an inverting analogical adder.
$V_{in,k}$	k^{th} input voltage of an analogical adder.
$V_{out,P}$	Output signal of the Post-processing Signal circuit corresponding to a radiation power $P(t)$ incident on the FQP.
V_{out,P_0}	Output signal of the Post-processing Signal circuit corresponding to a radiation power P_0 incident on the FQP.

$V_{out,non}$	Output voltage of a non-inverting analogical adder.
$V_{out,x}$	Output voltage of the Post-processing Signal circuit indicating the spot displacement on the FQP along the direction x.
$V_{out,y}$	Output voltage of the Post-processing Signal circuit indicating the spot displacement on the FQP along the direction y.
V_{Q1}	Output voltage of the preamplifier corresponding to the photocurrent I_{Q1}.
V_{Q2}	Output voltage of the preamplifier corresponding to the photocurrent I_{Q2}.
V_{Q3}	Output voltage of the preamplifier corresponding to the photocurrent I_{Q3}.
V_{Q4}	Output voltage of the preamplifier corresponding to the photocurrent I_{Q4}.
$V_{noise,x}$	Measured rms noise values at the post-processing signal output $V_{out,x}$.
$V_{noise,y}$	Measured rms noise values at the post-processing signal output $V_{out,y}$.
V_{REF}	Precision voltage reference.
W	Beam radius on the FQP surface.
W'	Beam radius average along the interaction between the probe beam and DUT (spatial error).
$W(z)$	Probe beam radius as a function of the propagation direction Z.
W_0	Minimum radius of a laser beam according to the beam waist theory.
X	Horizontal direction displacement of the micro-positioning stages.
x	Beam horizontal deflection.
Y	Vertical direction displacement of the micro-positioning stages.
y	Beam vertical deflection.

y_0 Inspection depth.

z Beam propagation direction.

Z Beam propagation direction displacement of the micro-positioning stages.

Z_m Transimpedance gain corresponding to each preamplifier channel.

z_0 Characteristic propagation distance for a Gaussian beam (Rayleigh distance).

LIST OF ABBREVIATIONS

ASE	Amplified Spontaneous Emission
BJT	Bipolar Junction Transistor
BLP	Backside Laser Probing
DBLP	Differential Backside Laser Probing
DFB	Distributed FeedBack
DUT	Device Under Test
EMI	ElectroMagnetic Interference
FCA	Free-carrier absorption
FC/APC	Fiber Contact Angular Physical Contact
FMT	Fluorescence MicroThermography
FQP	Four Quadrant Photodiode
FWD	Free-wheeling diode
GaN	Gallium Nitride
IFP	Fabry-Perot Interferometry
IGBT	Insulated Gate Bipolar Transistor
IIR-LD	Internal IR-Laser Deflection
IMS	Insulated Metal Substrate
IMZ	Interferometria Mach Zender
IRT	InfraRed Termography
LCT	Liquid Crystal Termography
LDMOS	Lateral Diffused Metal Oxide Semiconductor
LED	Light Emitting Diode
MOSFET	Metal Oxide Semiconductor Field Effect Transistor
NPT-IGBT	Non Punch Through Insulated Gate Bipolar Transistor
OCVD	Open Circuit Coltage Decay

Op Amp	Operational Amplifier
PT-IGBT	Punch Through Insulated Gate Bipolar Transistor
SCU	Synchronisation and Control Unit
SFM	Scanning Force Microscope
SiC	Silicon Carbide
SNR	Signal-to-Noise Ratio
SThM	Scanning Thermal Microscopy
STM	Scanning Tunneling Microscope
SRH	Shockley-Read-Hall model
SRIM	Stopping and range of Ions in Matter
TIA	TransImpedance Amplifier
TSP	Temperature Sensitive Parameter
TVS	Transient Voltage Supressor
TTC	Thermal Test Chip
VDMOS	Vertical Difused Metal Oxide Semiconductor

Bibliography

[1] B. J. Baliga. *Modern Power Devices*. John Wiley & Sons Inc., New York, USA, 1987.

[2] J. Vobecký. “Lifetime engineering in high power devices”. *Proc. of ASDAM* (Smolenice Castle, Slovakia), pp. 21-28, 2000.

[3] R. M. Scarlett, W. Schockley, and RH Haitz. “Thermal instabilities and hot spots in junction temperature”. In: F. Goldberg, J. Vaccaro (ed.). *Physics of Failure in Electronics*. Baltimore: Spartan, pp. 194-203, 1965.

[4] P. A. Aloisi. “Thermomechanical degradation and thermal fatigue”. *Proc. of ESREF* (Bordeaux, France), pp. 253-257, 1993.

[5] W. Wu, M.Held, P.Scacco and A.Birolini. “Investigation on the long term reliability of power IGBT modules”. *Proc. of ISPSD* (Yokohama), pp. 443-448, 1995.

[6] W. Wu, M. Held, P.Scacco and A.Birolini. “Thermal stress related packaging failure in power devices”. *Proc. of ISPSD* (Yokohama), pp. 330-334, 1995.

[7] J. W. Sofia, “Electrical temperature measurement using semiconductors”. *Electronics Cooling*, 3(1):22-25, 1997.

[8] A. Ammous, B. Allard and H. Morel, “Transient temperature measurements and modelling of IGBT’s under short circuit”. *IEEE T. Power Electr.* 13(1):12-25, 1998.

[9] F. Oettinger, D. L. Blackburn, and E. Rubin. “Thermal characterization of power transistors”. *IEEE T. Electron. Dev.*, 23(8):831-838, 1976.

[10] A. Hamidi and G. Coquery. “Effects of current density and chip temperature distribution on lifetime of high power IGBT modules in traction working conditions”. *Microelectron. Reliab.*, 37(10-11):1755-1758, 1997.

[11] T. Kajiwara, A. Yamaguchi, Y. Hoshi, and K. Sakurai. “New intelligent power multi-chips modules with junction temperature detecting function”. *Proc. of ISPSD* (Kyoto, Japan), pp. 281-284, 1998.

[12] Y. K. Leung, S.C. Kuehne, V. S. K. Huang, C. T. Nguyen, A. K. Paul, J. D. Plummer, and S. S. Wong. “Spatial temperature profiles due to nonuniform self-heating in LDMOS’s in thin SOI”. *IEEE Electr. Device L.*, 18(1):13-15, 1997.

[13] G. B. M. Fiege, F. J. Niedernostheide, H. J. Schulze, R. Barthelmess and L. J. Balk. “Thermal characterization of power devices by scanning thermal microscopy techniques”. *Microelectron. Reliab.*, 39(6-7):1149-1152, 1999.

[14] G. B. M. Fiege, A. Altes, R. Heiderhoff, and L. J. Balk. “Quantitative thermal conductivity measurements with nanometre resolution”. *J. Phys. D: Appl. Phys.*, 32(5):13-17, 1999.

[15] A. Mujamdar, J. P. Carrejo, and J. Lai. “Thermal imaging using the atomic force microscope”. *Appl. Phys. Lett.*, 62(20):2501-2503, 1993.

[16] J. Kölzer, E. Oersterschulze, and G. Deboy. “Thermal Imaging and measurement techniques for electronic materials and devices”. *Microeletron. Eng.*, 31(1-4):251-270, 1996.

[17] G. Gaussorgues. *Infrared Thermography*. Cambridge: Chapman & Hall, 1994.

[18] D. L. Barton and P. Tangyunyong,. “Fluorescent microthermal imaging-Theory and methodology for achieving high thermal resolution images”. *Microeletron. Eng.* 31(1-4): 271-279, 1996.

[19] A. Csendes, V. Székely, and M. Rencz. “Thermal mapping with liquid crystal method”. *Microeletron. Eng.*, 31(1-4): 281-290, 1996.

[20] W. Claeys, S. Dilhaire, V. Quintard, J. P. Dom, and Y. Danto. “Thermoreflectance optical test probe for the measurement of current-induced temperature changes in microelectronic components”. *Qual. Rel. Eng. Int.*, 9():303-308, 1993.

[21] S. Dilhaire, T. Phan, E. Schaub, and W. Claeys. “Thermomechanical and electromigration studies with a high sensitive and high resolution laser probe”. *Proc. of IPFA* (Singapore), pp. 62-67, 1997.

[22] R. Abid, F. Miserey, and F.-Z. Mezroua. “Effet de la Temperature sur la Reflectivite du Silicium Oxyde : Determination Experimentale de la Sensibilite Relative; Application a la Mesure sans Contact de la Temperature a la Surface d’un Thyristor GTO en Commutation”. *J. de Phys. III*, 6(2):279-300, 1996.

[23] G. Deboy, G. Sölkner, E. Wolfgang, and W. Claeys. “Absolute measurements of transient carrier concentration and temperature gradients in power semiconductor devices by internal IR-laser deflection”. *Microeletron. Eng.*, 31(1-4):299-307, 1996.

[24] M. Goldstein, G. Sölkner, and E. Gornik. "Heterodyn interferometer for the detection of electric and thermal signals in integrated circuits through the substrate". *Rev. Sci. Instr.*, 64(10):3009-3013, 1993.

[25] N. Seliger, P. Habaš, and E. Gornik. "A study of backside laser-probe signals in MOSFETs". *Microeletron. Eng.*, 24(1-4):431-436, 1996.

[26] C. Fürböck, R. Thalhammer, M. Litzenberger, N. Seliger, D. Pogany, E. Gornik, and G. Wachutka. "A differential backside laser-probing technique for the investigation of the lateral temperature distribution in power devices". *Proc. of ISPSD* (Kyoto, Japan), pp. 193-196, 1999.

[27] R. Thalhammer. *Internal laser probing techniques for power devices: analysis, modeling and simulation*. Doctoral dissertation, Technishen Universität München, Fakultät für Elektrotechnik und Informationstechnik, 2000.

[28] D. Pogany, N. Seliger, E. Gornik, M. Stoisiek, and T. Lalinsky. "Analysis of the temperature evolution from the time resolved thermo-optical interferometric measurements with few Fabry-Pérot peaks". *J. Appl. Phys.*, 84(8):4495-4501, 1998.

[29] N. Seliger, D. Pogany, C. Fürböck, P. Habas, E. Gornik, and M. Stoisiek. "A study of temperature distribution in SOI–smart power devices in transient conditions by optical interferometry". *Proc. of ESSDERC* (Stuttgart, Germany), pp. 512, 1997.

[30] R. F. Pierret. Volume I: Semiconductor Fundamentals. Belonging to the collection: Modular Series on Solid State Devices. Addison-Wesley, 2nd edition, 1988.

[31] R. A. Soref, and B. R. Bennett. "Electrooptical Effects in Silicon". *IEEE J. Quantum Elect.*, 23(1):123-129, 1987.

[32] D. K. Schroeder, R. N. Thomas, and J. C Swartz. "Free Carrier Absorption in Silicon". *IEEE J. Solid-St. Circ.*, 13(1):180-187, 1978.

[33] J. Isenberg, and W. Warta. "Free Carrier Absorption in Heavily Doped Silicon Layers". *Appl. Phys. Lett.*, 84(13):2265-2267, 2004.

[34] H. C. Huang, S. Yee, and M. Soma. "Quantum Calculations of the Change of Refractive Index Due to Free Carriers in Silicon with Nonparabolic Band Structure". *J. Appl. Phys.*, 67(4):2033-2039, 1990.

[35] G. Schierwater. *Untersuchung der Optischen Absorption an Freien Ladungsträgern und der Rekombinationsstrahlung am Elektron-Loch-Plasma von Pin-Dioden*. Ph. D. Thesis, Technishe Universität Berlin, 1975.

[36] C. M. Horwitz,, R. M. Swanson. “The optical (free-carrier) absorption of a hole-electron plasma in Silicon”. *Solid-State Electron.*, 23(12-A): 1191-1194, 1980.

[37] G. Deboy, et al. “Absolute Measurement of Transient Carrier Concentration and Temperature Gradients in Power Semiconductor Devices by Internal IR-laser Deflection”. *Microelectron. Eng.*, 31(1-4): 299-307, 1996.

[38] F. Hille, R. Thalhammer. *Die Eignung des Verfahrens der Internen Laserdeflexion als Charakterisierungsmethode für Leistungsbauelemente*. Technical report 1997/5, Institüt für technishe elektrophysik, Technishe Universität München, 1997.

[39] A. E. Schlögl. *Theorie und Validierung der Modelbildung Bipolarer Leistungshalbleiter im Temperaturbereich*. Ph. D. Thesis, Technishe Universität München, Fakultät der Elektrotechnik und Informationstechnik, 1999.

[40] N. W. Ashcroft, and N. D. Mermin. *Solid State Physics*. Intenational edition. Orlando: Saunders college, 1976.

[41] J. C. Sturm, and C. M. Reaves. “Silicon Temperature Measurement by Infrared Absorption: Fundamental Processes and Doping Effects”. *IEEE T. Electron. Dev.*, 39(1):81-88, 1992.

[42] A. N. Magunov. “Temperature dependence of the refractive index of Silicon single crystal in the 300-700 K range”. *Opt. Spec.*, 73(2):205-206, 1992.

[43] G. Gosh. “Temperature Dispersion of Refractive Indices in Crystalline and Amorphous Silicon”. *App. Phys. Lett.*, 66(26):3570-3572, 1995.

[44] H. H. Li. “Refractive Index of Silicon and Germanium and Its Wavelength and Temperature Derivatives”. *J. Phys. Chem. Ref. data*, 9(3):561-658, 1980.

[45] M. Bertolotti, et al. “Temperature dependence of the refractive index in semiconductors”. *J. Opt. Soc. Am. B*, 7(6): 918-922, 1990.

[46] N. Seliger, P. Habaš, E. Gornik. “Time-domain characterization of lattice heating in power VDMOSFETs by means of an interferometric laser probe technique”. *Proc. of ESSDERC* (Bologna), pp. 847-850, 1996.

[47] R. Thalhammer, F. Hille, and G. Wachutka. “Optimizing free carrier absorption measurements for power devices by physically rigorous simulation”. *Proc. of SISPAD* (Seattle, USA) pp. 249-252, 2000.

[48] B. E. A Saleh, M. C. Teich. “Chapter 3: Beam optics”. Extracted from: *Fundamentals of Photonics*, New York: John Wiley, pp. 80-107, 1992.

[49] J. E. Midwinter, Y. L. Guo. “Chapter 6: Semiconductor lasers and quantum well devices”. Extracted from: *Optoelectronics and lightwave technology*. Chichester (England): John Wiley, pp. 212-264, 1992.

[50] Melles Griot. “Introduction to Gaussian beam optics”. *Melles Griot catalogue*, 1999.

[51] X. Perpiñà, X. Jordà, N. Mestres, M. Vellvehi, P. Godignon, J. Millán, and H. von Kiedrowski. “Internal infrared laser deflection system: A tool for power devices characterization”. *Meas. Sci. Technol.*, 15(5):1011-1018.

[52] J. G.Graeme, Photodiode amplifier: OP AMP solutions, Mc Graw Hill, New York, 1996.

[53] AME-UDT Sensors Europe, *Photodetector Catalogue*, OSI Systems, 1999.

[54] W. G. Jung, *Op amp applications*, Analog Devices, 2002

[55] “Ultralow Distortion,Ultralow Noise Op Amp AD797”, Analog Devices, datasheet.

[56] “High Precision 5 V Reference AD586”, Analog Devices, datasheet.

[57] “AD734 10 MHz, 4-QuadrantMultiplier/Divider”, Analog Devices, datasheet.

[58] R. H. Hamstra, Jr., and Paul Wendland. “Noise and Frequency Response of Silicon Photodiode Operational Amplifier Combination”. *Appl. Opt.*, 11(7):1539-1547, 1972.

[59] A. Mäkynen, J. Kostamovaara, R. Myllylä. “Positioning Resolution of the Position-Sensitive Detectors in High Background Illumination”. *IEEE T. Instrum. Meas.*, 45(1):324-326, 1996.

[60] X. Jordà, X. Dalmau, P. Godignon, M. Vellvehi, X. Perpiñà, S. Hidalgo, and J. Millán. “Modular characterisation system for Power Devices”. *Proc. of ISPS* (Praga, Czech Republic), pp. 199-203, 2002.

[61] F. Madrid. *Termal Conductivity and Specific Heat Measurements for Power Electronics Packaging Materials*. PhD dissertation, Escola Tècnica Superior d’Enginyeria of Universitat Autònoma de Barcelona (UAB), Cerdanyola del Vallés (Barcelona), 2005.

[62] Flomerics Limited, *Flotherm Manual*, Issue 1.0, 2003.

[63] M. Necati Ösizik. *Heat conduction*. 2nd edition, John Wiley and Sons, New York, 1993.

[64] D.R. Lide, H.P.R. Frederikse, A.L. Smith, W.C. Lineberger, C.C. Lin, N.C. Craig, R.N. Goldberg, T.F. Koetzle, and K. Kuchitsu, *CRC Handbook of Chemistry and Physics*, 79th edition, CRC Press LLC, Boca Raton (Florida), 1998.

[65] G. Cocorullo, F. G. Della Corte, and I. Rendina. "Temperature dependence of the thermo-optic coefficient in crystalline Silicon between room temperature and 550 K at the wavelength of 1523 nm". *Appl. Phys. Lett.*, 74(22):3338-3340, 1999.

[66] H. Bleichner, P. Johnsson, N. Kestikalo, and E. Nordlander. "Temperature and injection dependence of the Shockley-Read-Hall lifetime in electron irradiated n-type Silicon". *J. Appl. Phys.*, 79(12):9142-9148, 1996.

[67] J. Vobecký and P. Hazdra. "Future trends in local lifetime control". *Proc. of ISPSD* (Maui, USA), pp. 161-164, 1996.

[68] P. Hazdra and J. Vobecký. "Accurate simulation of fast ion irradiated power devices". *Solid State Electron.*, 37(1):127-134, 1994.

[69] M. Rosling, H. Bleichner, and E. Nordlander. "A position-sensitive method for determination of high-level carrier lifetimes in power devices". *Proc. of EPE-MADEP* (Firenze, Italy), pp. 59-63, 1991.

[70] P. Hazdra, J. Vobecky, H. Dorschner, K. Brand. "Axial lifetime control in Silicon poer diodes by irradiation with protons, alphas, low- and high-energy electrons". *Microelectron. J.*, 35(3):249-257, 2004.

[71] ISE integrated systems engineering, *ISE TCAD manuals, release 9.0*, 2003.

[72] P. Jonsson, H. Bleichner, M. Isberg, and E. Nordlander. "The ambipolar Auger coefficient: Measured temperature dependence in electron irradiated and highly injected n-type Silicon". *J. Appl. Phys.*, 81(5):2256-2262, 1997.

[73] D. K. Schroder. "Carrier lifetimes in Silicon". *IEEE T. Eletron. Dev.*, 44(1):160-170, 1997.

[74] L. W. Davies. "The use of P-L-N structures in investigations of transient recombination from high injection levels in semiconductors". *Proc. of IEEE*, 51:1637-1642, 1963.

[75] Z. G. Ling, P. K. Ajmera, and G. S. Kousik. "Simultaneous extraction of bulk lifetime and surface recombination velocities from free carrier absorption transients". *J. Appl. Phys.*, 75(5):2718-2720, 1994.

[76] SRIM2000.39, J. F. Ziegler, and J.P. Biersack. "Stopping and Range of Ions in Matter", software, copyright IBM 1998, 2000.

[77] J. Vobecky and P. Hazdra. “Advanced local lifetime control for higher reliability of power devices”. *Microelectron. Reliab.*, 43(9-11):1883-1888, 2003.

[78] B. J. Baliga. *Power semiconductor devices*. Boston: PWS publishing company, pp.1-8, 1996.

[79] R. Siemieniec, R. Herzer, M. Netzel, and J. Lutz. “Application of carrier lifetime control by irradiation”. *Proc. of Miel* (Niš, Serbia and Montenegro), pp. 167-170, 2004.

[80] J. Vobecký, P. Hazdra, X. Jordà, P. Godignon, M. Vellvehi. “Parameter Optimisation of the 600V PT-IGBT using the Backside Proton Irradiation”. *Proc. of ISPS* (Prague, Czech Republic), pp. 245-248, 2002

[81] ISE Integrated Systems Engineering, ISE TCAD manuals, 2001.

[82] H. S. Carslaw, and J. C. Jaeger. *Conduction of heat in solids*. 2nd edition, Oxford University Press, Oxford, 1959.

[83] B. Abeles, D. S. Beers, J. P. Dismukes, and G. D. Cody. “Thermal conductivity of Ge-Si alloys at high temperatures”, *Phys. Rev.*, 125(1):44-46, 1962.

[84] R. Thalhammer, F. Hille, and G. Wachutka. “Optimizing free carrier absorption measurements for power devices by physically rigorous simulation”. *Proc. Of SISPAD* (Seattle, USA), pp. 249-252, 2000.

[85] P. Mejias Arias, and R. Martínez Herrero. “Capítulo 3: Principio de Fermat. Propagación en medios inhomogéneos”. In: *Óptica geométrica*. Madrid: Síntesis , pp. 45-61, 1999.